Condition monitoring of Lithium-Ion batteries using broadband multisine excitation and Electrochemical Impedance Spectroscopy

Prepared by:

Alfred Waligo

Department of Electrical Engineering

University of Cape Town

April 2018

Submitted to the Department of Electrical Engineering at the University of Cape Town in partial fulfilment of the academic requirements for a Master's of Science degree in **ELECTRICAL ENGINEERING**

Declaration

1. I know the meaning of plagiarism and declare that all the work in the document, save for that which is properly acknowledged, is my own. This thesis/dissertation has been submitted to the Turnitin module and I confirm that my supervisor has seen my report and any concerns revealed by such have been resolved with my supervisor

2. I have used the IEEE convention for citation and referencing. Each contribution to, and quotation in, this final year project report from the work(s) of other people, has been attributed and has been cited and referenced.

3. This Master's Thesis Dissertation is my own work.

4. I have not allowed, and will not allow, anyone to copy my work with the intention of passing it off as their own work or part thereof.

Name: **ALFRED WALIGO**

Signature: Signed by candidate **Date:** 22 December 2017

Acknowledgements

I thank God for this opportunity, for giving me life and for enabling me to come this far.

To my supervisor Prof P. Barendse for his mentorship and guidance throughout the entirety of the master's degree as well as the undergraduate degree and for allowing me to serve as a TA in the department.

Special thanks to Phillip Titus and Chris Wozniak who were always present to help me with the experimental setup throughout the duration of the degree.

I would like to thank my fellow members of the AMES Group who've given me valuable input when I was stuck. Special mention goes to Prof Khan, Tumi, Andrew, Jonathan, Olufemi, Chris De Beer, Jamlick, Oladapo.

To Thobile Dube, my ninja for keeping me sane throughout my Masters, and Samantha Malunga for the emotional support.

Last but not least, to my Mom, Mrs. Rita Waligo for her encouragement, prayer and parental guidance.

Abstract

Electrochemical Impedance Spectroscopy (EIS) is a well-known technique that has been employed on various electrochemical cells to obtain their impedance spectra. Lithium-ion(Li-ion) cells are some of the cells to which it has been applied. The impedance spectra obtained from EIS can be used to estimate various batteries State of Health (SOH) and State of Charge (SOC) characteristics. The lengthy acquisition time associated with standard EIS makes it unsuitable for rapid on-line impedance measurements. Alternative methods that take a shorter time have therefore been proposed. This study compares the spectra obtained by the Harmonic Compensated Synchronous Detection (HCSD) broadband signal technique with the EIS and a custom Broadband Impedance Spectroscopy (BIS) technique, at different states of charge, which mimic a real-time load. The test cells are industry standard Nickel-Cobalt and Manganese Oxide (NCM) Li-ion cells. The BIS technique is like HCSD in the selection of frequencies; however, the amplitude of the excitation broadband signal is varied to match the impedance magnitude response of the cell. Also, parameter extraction is performed on both EIS and BIS techniques for fault detection purposes.

Table of Contents

List of Figures

List of Tables

List of Abbreviations

This section describes the common abbreviations used throughout this thesis.

Li-ion	-	Lithium Ion
SOC	-	State of Charge
OCV	-	Open Circuit Voltage
SOH	-	State of Health
EIS	-	Electrochemical Impedance Spectroscopy
EV	-	Electric Vehicle
HEV	-	Hybrid Electric Vehicle
PHEV	-	Power Assist Hybrid Electric Vehicle
NI-MH	-	Nickel Metal-Hydride
Pb-Acid	-	Lead Acid
Ni-Cd	-	Nickel Cadmium
IEC	-	International Electrotechnical Commission
HPPC	-	Hybrid Pulse Power Characterisation
SEI	-	Solid Electrolyte Interface
BIS	-	Broadband Impedance Spectroscopy
HCSD	-	Harmonic Compensated Synchronous Detection
OBIS	-	Optimised Broadband Impedance Spectroscopy
DFT	-	Discrete Fourier Transform
FFT	-	Fast Fourier Transform
Redox	-	Oxidation-reduction
VRLA	-	Valve Regulated Lead-Acid

1. Introduction

1.1 Background to the Study

The increased popularity of electric vehicles, together with the rapid growth of mobile phones and portable electronics has seen the demand for energy storage devices increase. In the automotive industry, the increasing demand for Hybrid Electric Vehicles (HEVs), Plug-in Hybrid Electric Vehicles (PHEVs) and pure Electric Vehicles (EVs) has boosted the development of Lithium-ion batteries. Lithium-ion (Li-ion) batteries are being used as a replacement for existing Pb-Acid and Ni-MH batteries due to their high energy densities and high specific power [1]. Figure 1-1 below shows how Li-ion cells compare with other cell chemistries in terms of weight and energy density. In the abovementioned vehicle applications, the battery pack's cost is relatively high compared to that of the vehicle, and it is therefore important that indicators such as SOH and Remaining Useful Life (RUL) are properly measured and analysed.

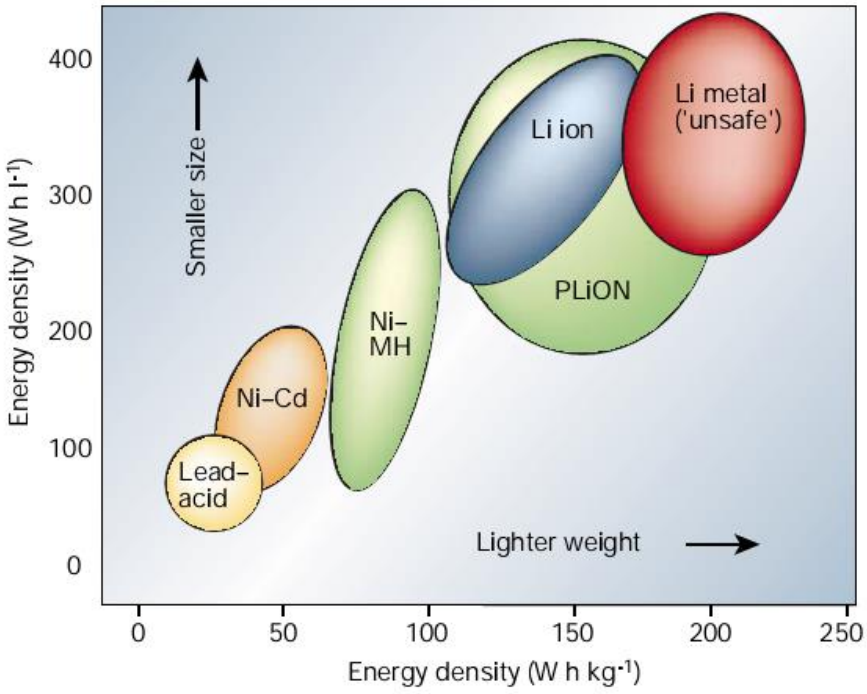

Figure 1-1: Comparison of battery technologies in terms of volumetric and gravimetric energy density [2]

Studies have shown that Li-ion cells state of health and performance is dependent on both the cell capacity as well as internal resistance. Decrease of battery capacity means an overall decrease in the driving distance, while an increase in internal impedance causes a reduction in the power capability and acceleration of the vehicle. Various common passive characteristic tests such as those that involve monitoring current and terminal voltages at different

temperature, are only able to give valuable information on state of charge and capacity as a percentage of the rated nominal capacity provided by the manufacturer. The information from these tests is however, not sufficient in the provision of a full state of health assessment of the battery, as various key information such as impedance rise, and power fade is absent from the results [3]. Other tests such as cold cranking, and hybrid pulse power characterisation can determine capacity and power capability. However, they take a long time and are not suitable in online applications, as their validation criteria cannot be met in these applications. Table 1.1 shows the common characterisation tests used in the determination of capacity and power capability for energy storage devices in automotive applications and their duration.

Table 1.1: Tests on Li-ion Cells for EV applications

Test	Parameters for Determination	Duration
Static Capacity Test	Capacity	One hour minimum (depending on discharge rate)
Pulse Power Characterisation Tests	Power Capability, Capacity	Sixty seconds per pulse for each Depth of Discharge level (DOD) /SOC with an hour rest interval between pulses[4]
DC Test	DC resistance	Eleven seconds[5]
AC Impedance Single Frequency Test	AC impedance	One to five seconds
Self-Discharge Test	Temporary Capacity loss	Seven days [5]
Cold Cranking	Power capability at low temperature	Four to eight hours

AC impedance testing has been proven and tested to be a useful measure of battery SOH and RUL. Data obtained from impedance measurements has been shown to correspond with resistance and power capability results from the hybrid pulse power characterisation tests. A full EIS however, requires expensive laboratory equipment in the form of frequency response analysers, and takes anywhere from ten minutes to an hour, depending on the number of frequency points chosen and the value of the lowest frequencies selected [6]. Studies have shown however that EIS can however be performed in an online system if the number of frequency points is reduced; however, the time taken is still reasonably longer, compared to techniques that are going to be explored in this thesis. Another technique that is currently being employed, to determine the frequency response in a short frequency range is HCSD. HCSD involves using an equal amplitude signal and a harmonic frequency spread. The harmonic spread in frequency is chosen so as to prevent crosstalk error and the resulting time wave form components are synchronously detected.

1.2 Objectives of this Study

- To perform a comprehensive literature review on Li-ion batteries, modelling and AC impedance measurement techniques such as EIS, in relation to Li-ion cell chemistry.
- To perform a full EIS on the cell at different states of charge and DC Bias currents, and compare the results with those obtained in the literature.
- To perform broadband impedance measurement techniques as well as optimizing an existing broadband impedance technique and comparing the results obtained with those from EIS.
- To extract the parameters from the EIS technique and compare them with those from one of the broadband based techniques, using a parameter extraction technique.
- To demonstrate that broadband based impedance measurement techniques, together with the parameter extraction methods, are applicable in online diagnostics of Li-ion batteries.

1.3 Scope and Limitations

This study is limited to the analysis and condition monitoring techniques that involve multisine or single sinusoidal excitation. Methods such as cold cranking, HPPT testing, and pulse power characterization are not covered.

1.4 Plan of Development

The rest of the thesis is subdivided into these chapters.

Chapter 2 presents a literature review of the different cells and batteries. The Li-ion cell chemistry is introduced, together with the modelling techniques and fault mechanisms associated with it. In this chapter, the Electrochemical Impedance Spectroscopy, and the broadband techniques of multisine excitation are also reviewed.

Chapter 3 discusses the experimental setup. It shows the overall hardware configuration, as well as the individual connections between the different hardware components.

Chapter 4 discusses the state of the charge measurement process. It shows how the initial, as well as current, cell state of charge was measured. It also shows the state of charge measurement block diagram and the theory behind how it was obtained. After discussing the

state of charge measurement process, it details the implementation of EIS. It covers cell conditioning, frequency selection, the sampling rate and excitation amplitudes, as well as the charge profile in between measurements. This chapter is concluded by the implementation of BIS, multisine excitation optimization and signal extraction. It shows how each of the different optimization criteria were optimised for the purposes of the experiments and how the multisine signals were generated

Chapter 5 presents and discusses the results obtained from the experiments performed in Chapter 4.

Chapter 6 is where the equivalent circuit model is chosen. A non-linear least squares algorithm is used to extract the parameters of the model and the simulated results from the model are compared with experimental data.

Chapters 7 and 8 are where the conclusions from the study, as well as recommendations for future work are made.

2. Literature Review

2.1 Cells and Batteries

A battery is a device that converts the chemical energy contained in its active materials directly into electrical energy, by means of a redox reaction[7]. For rechargeable systems, the battery is recharged by the reversal of this process. An exception to this is in the case of Li-ion batteries; whereby the electrochemical conversion is because of the movement of ions, and not electrons, as would be in a typical redox reaction.

The terms "cell" and "battery" are often used interchangeably; however, for clarity, a cell is the basic electrochemical unit that provides electrical energy by direct conversion of chemical energy. A battery consists of one or more of these cells connected in a parallel or a series or both. The choice as to which configuration is used depends on the required output voltage and capacity.

A cell consists of three major components. The anode, which is the negative electrode that gives up electrons to the external circuit and is then oxidised. This electrode is also called the reducing electrode or fuel electrode. The second component is the cathode or positive electrode. This is the oxidizing electrode that accepts electrons from the external circuit and is reduced during the electrochemical reaction. The third component is the electrolyte. This is the ionic conductor which provides the medium for the transfer of charge, as ions inside the cell, between the anode and cathode. This electrolyte can either be liquid or solid.

2.1.1 Classification of cells or batteries

There are four broad categories of cells and batteries[7], these are:

- Primary cells
- Secondary cells
- Reserve cells
- Fuel cells

i. Primary Cells

Primary cells are cells which when discharged cannot be returned to their original condition by passing a current through in the opposite direction. However, there are a specific category of

primary cells that form an exception to this, but this is beyond the scope of this thesis. Most primary cells utilise electrolytes that are contained within absorbent materials or a separator and are thus termed dry cells [8]. Examples of primary cells are zinc-carbon/Leclanche dry cells (most common low-cost primary battery), Zinc/air, Zinc/Alkaline-manganese dioxide (more premium), Mercuric oxide, Silver oxide and Lithium-metal anode cells, with different cathode substrates. The applications for primary cells such as the zinc-carbon and zinc/alkaline/manganese-dioxide include, flashlights, radios, toys and portable electronics. The silver/zinc and zinc air cells are used predominantly for hearing aids, cameras, space applications and missiles, because of their higher energy density and higher capacity.

ii. Secondary Cells

Secondary (or rechargeable cells) are those which when after discharge can be returned to their original condition by passing a current through in the opposite direction to that of the discharge current[7]. Secondary cells are further subdivided into two sub-categories depending on their intended applications. These are:

- Cells that are utilized as energy storage devices delivering energy on demand. These cells are normally connected to primary power sources to fully be charged on demand. Examples of these applications are in aircraft systems, emergency no-fail and standby power sources.
- Cells that are used as primary cells but are recharged after use such as in EVs and consumer electronics.

Examples of secondary cells are lead acid, nickel-cadmium, iron electrode, nickel-zinc, nickel-metal hydride and Li-ion cells. The Starting Lighting Ignition (SLI) lead acid battery is by far the most popular lead acid battery, primarily for its use in the automotive industry. The other types of lead acid batteries such as VRLAs are used in UPS applications. Nickel cadmium batteries are the most common alkaline batteries and are used mainly in industrial applications such as mining vehicles, railways and trucks. [7]. Nickel Metal Hydride and Li-ion Cells dominate the EV and consumer electronic market. NiMH batteries have been used for EVs such as General Motors EV1, the Honda EV plus, Ford Ranger EV and the Vectrix scooter as well as HEVs such as the Toyota Prius, Honda Civic and Ford Escape. Li-ion batteries have been used on EVs and PHEVs such as the Chevy Volt, Mitsubishi i-MiEV, BMW i3, Tesla Model S and the Nissan Leaf. They have also been used in space applications such as the Mars Curiosity[9]. The primary focus of this thesis will be on Li-ion cells which fall into the secondary cell category.

iii. Reserve cells

Reserve cells are a special kind of cell in which the key component of the cell is separated from the remaining components until just prior to activation. The component which is most often isolated is the electrolyte. Applications where reserve cells are used are often military type[8]. There are four categories of reserve cells and these are:

- Gas activated cells
- Heat activated cells
- Electrolyte activated cells
- Water activated cells

iv. Fuel cells

The last category of cells are the fuel cells. They are like the batteries with the exception being that the active materials are not an integral part of the device, as in the case of an ordinary battery. All active materials are fed into the cell from an external source. Fuel cells are increasingly being used in utility power applications, load levelling and site generators [7].

2.2 Li-ion Cells

2.2.1 Li-ion cell structure

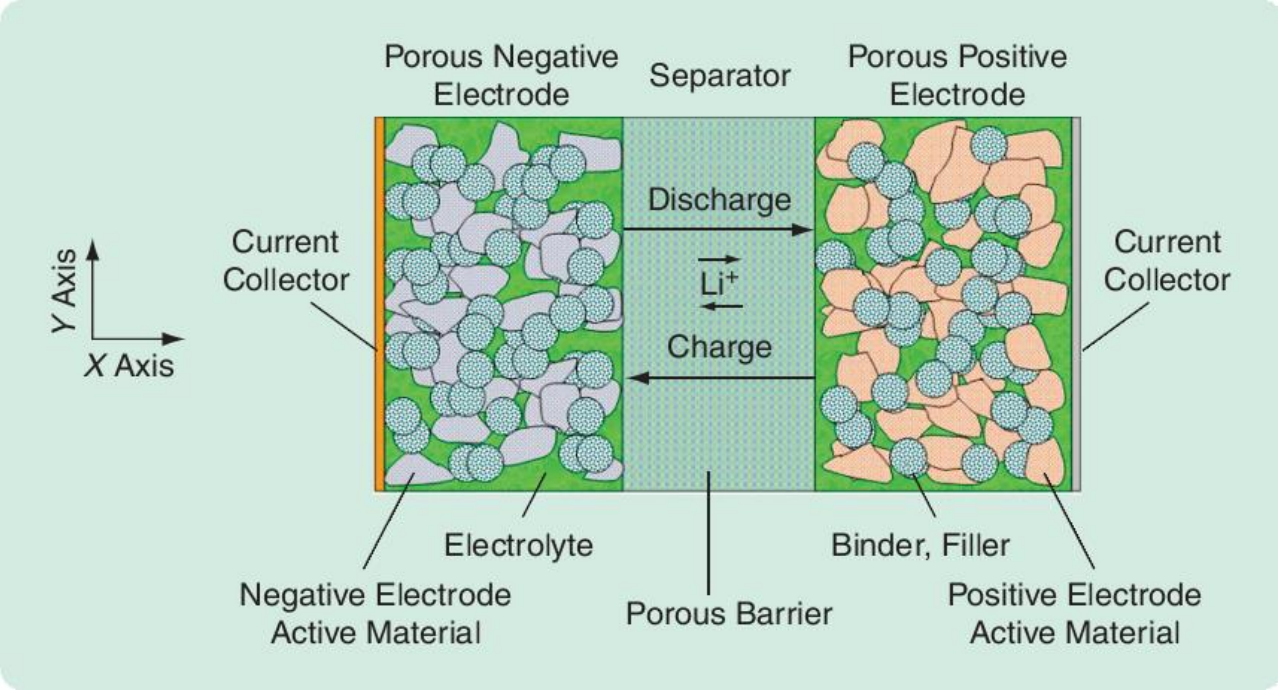

Figure 2-1: Li-ion cell structure[1]

The Li-ion cell has four main components as shown in Figure 2-1 :

- The negative electrode (anode)
- The positive electrode (cathode)
- The separator
- The electrolyte

The negative electrode is usually made of graphite and is connected to the negative terminal of the cell. The positive electrode is made up of different Lithium metal oxides. The separator is an electrical insulator that does not allow electrons to flow between the positive and negative electrodes, but because it is porous, it allows ions to pass through it by means of an electrolyte. The electrolyte is a concentrated solution that contains charged species. These species can move in response to an electrochemical potential gradient. Some Li-ions have a solid electrolyte which serves as both an ionic conducting medium and an electronically insulating separator [1].

2.2.2 Li-ion cell development

Lithium metal's use in battery technology is based on the fact that Li is the most electropositive metal as well as the lightest (equivalent weight M= 6.94g mol^{-1}) metal. It therefore facilitates the design of storage systems with high energy density. The advantage of using Lithium metal was demonstrated in the 1970s where primary cells were assembled using Lithium metal electrodes. At the same time, numerous organic compounds were shown to react with alkali metals in a reversible way. The discovery of such materials, which were later identified as intercalation compounds, was crucial in the development of high energy rechargeable Li systems. Initially there were numerous safety issues involved with using Lithium metal as a negative electrode. Lithium being highly reactive, made cells unsafe, and this prompted research into alternative solutions. In the 1980s, research showed that replacing the Lithium negative electrode with another intercalation material was possible. Using the layered material and instead inserting Li-ions, gave birth to the modern Li-ion cells of today, and made the cell much safer [2].

2.2.3 Li-ion electrode structures

Li-ion cells deviate from the traditional redox reaction mechanisms that commonly occur for other secondary cell chemistries. Li-ion cell chemistry uses an intercalation mechanism. This is

why Li-ion cells are also referred to as intercalation cells. This mechanism involves the insertion of Li-ions into the crystalline lattice of the host electrode, without changing its crystal structure. The electrodes have two key properties [10]:

- They have open crystal structures, which allow for the insertion or extraction of Li-ions. The two main structures for the electrode materials are spinel and layered structures.
- They can accept compensating electrons at the same time.

The anode (negative electrode) is usually made of graphite carbon, which is a layered structure that can allow for Li-ions to be inserted and removed. This carbon is usually lithiated, which simply means that Li-ions have been inserted into its layers. The cathode (positive electrode) is made of a Lithium Metal Oxide such as Lithium Cobalt Dioxide or Lithium Manganese Dioxide, as will be discussed in section 2.2.5. The cathode structure can also be layered just like the anode, or have a spinel structure. See Figure 2-4 and Figure 2-5 for an illustration of the different cathode structures.

2.2.4 Charge and discharge process of Li-ion cells

During discharge, Li-ions move from the anode through the electrolyte and are inserted into the crystal structure of the cathode. This process is shown in Figure 2-2 below. Often this process is referred to as the insertion of Li-ions into the intercalation layers of the electrodes. At the same time, the compensating electrons travel in the external circuit and are accepted by the host to balance the reaction. This process is reversible and during charging, the Li-ions instead move from the cathode to the anode.

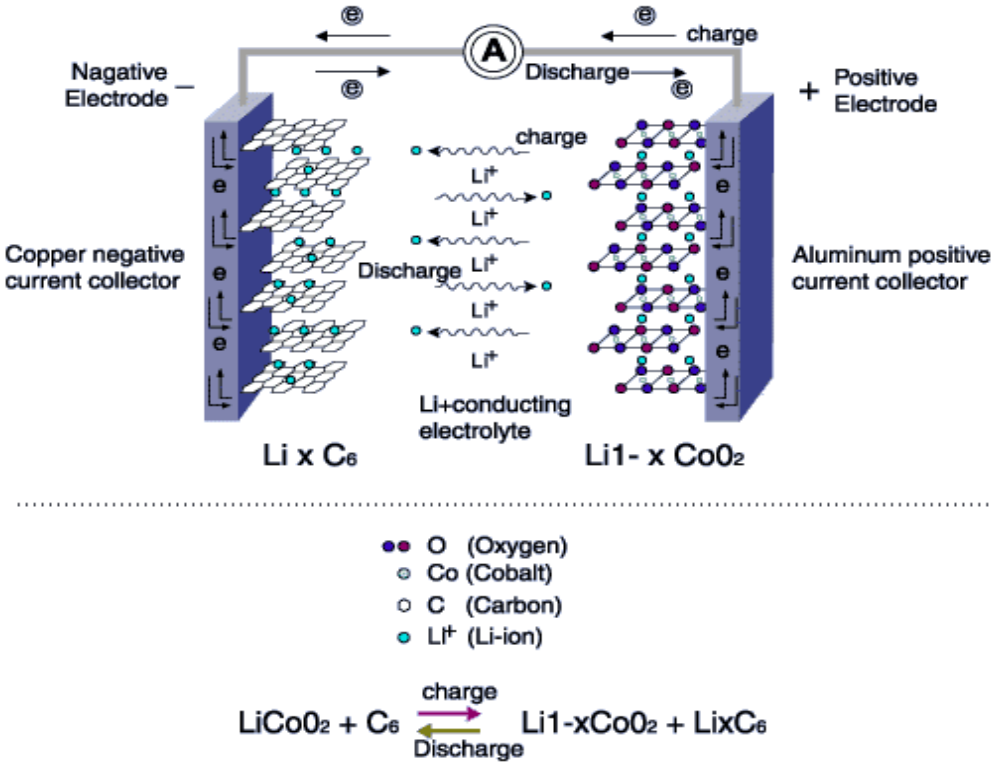

Figure 2-2: Image representing the charging and discharging mechanism in a typical Li-ion cell [11]

During charging, the constant voltage/constant current method is used to charge Li-ion batteries. The maximum voltage to which the cells should be charged is 4.2V * the number of cells connected in series. The charge current should be less than 1C and even lower i.e. around 0.1C if the voltage is 2.9V or less. See Figure 2-3 for the typical charging profile applied to Li-ion cells [11].

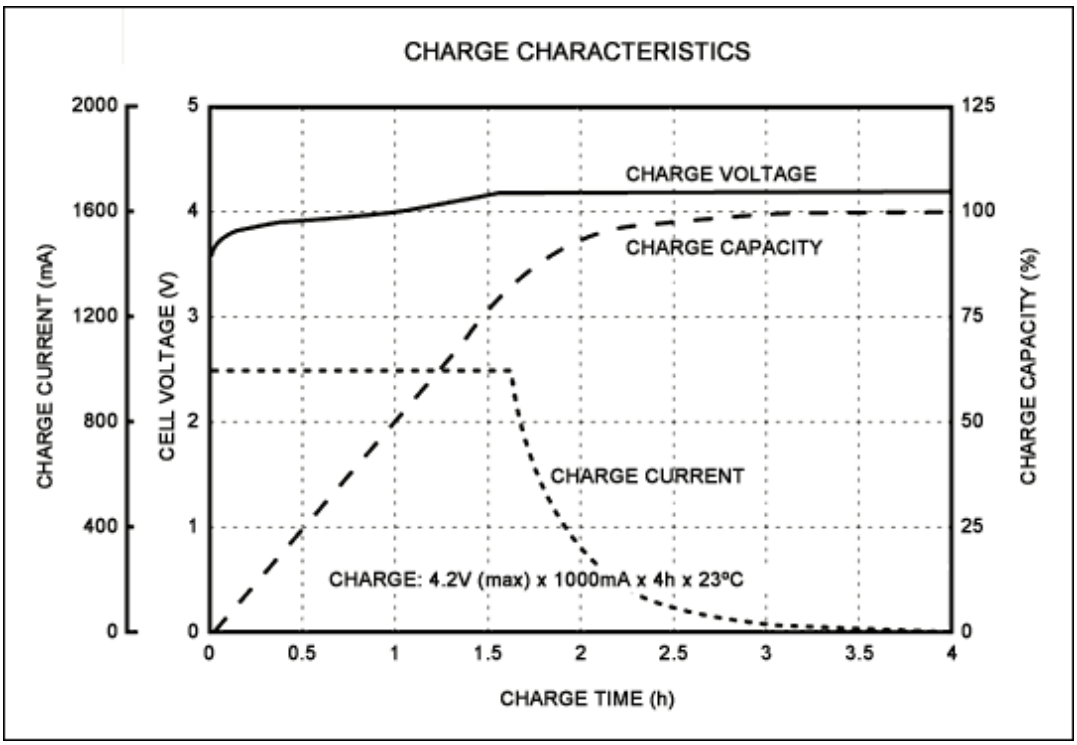

Figure 2-3: Charging profile of the Li-ion cell [11]

During discharge, the current should be maintained at 1.0C or less; however, there are some cell chemistries that allow for higher discharge currents for short periods of time, normally called burst charges [11].

2.2.5 Li-ion battery types

There are various types of Li-ion batteries, however the six most common types of Li-ion batteries are:

- Lithium Cobalt Oxide ($LiCoO_2$)
- Lithium Manganese Oxide ($LiMn_2O_4$)
- Lithium Nickel Manganese Cobalt Oxide ($LiNiMnCoO_2$ or NMC)
- Lithium Iron Phosphate ($LiFePO_4$)
- Lithium Nickel Cobalt Aluminium Oxide ($LiNiCoAlO_2$)
- Lithium Titanate ($Li_4Ti_5O_{12}$)

i. Lithium Cobalt Oxide

Lithium cobalt oxide is the battery choice for cell phones, laptops and digital cameras because of its high specific energy of about 200Wh/kg. The battery is made up of a cobalt oxide cathode

and a graphite carbon anode. The cathode has a layered structure and during discharge, Li-ions move from the anode to the cathode. The major drawback of this type of cell is its short and limited life span. Lithium cobalt oxide cannot be charged and discharged at a current higher than its C rating. This means that a cell rated 2400mAh in capacity cannot be charged at more than 2400mA without causing overheating and stress [12]. Figure 2-4 shows the structure of the Lithium cobalt oxide cathode.

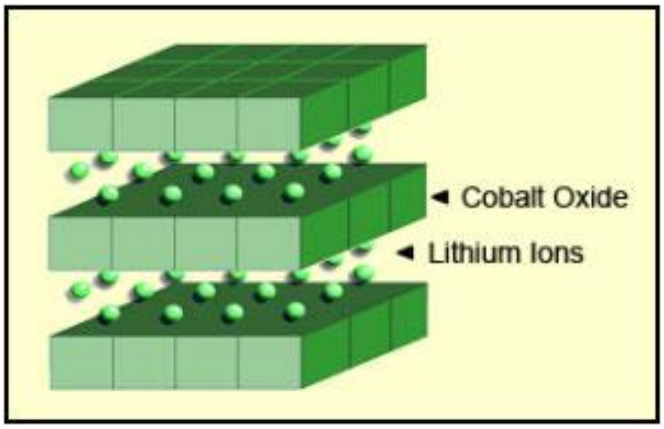

Figure 2-4: Structure of $LiCoO_2$ cell cathode [12]

ii. Lithium Manganese Oxide

There are two types of Lithium manganese oxide cells, the first being the spinel LMn_2O_4 and the other being the layered Li_2MnO_3. The former is the more dominant of the two since the latter has a poor capacity and poor cycling stability [13]. The cell is made of Lithium Manganese oxide as the cathode material and has a low internal resistance, which promotes fast charging and discharging, making it appropriate for use in EV applications. These cells however have thirty-three per cent less capacity than the $LiCoO_2$ cells described above. Lithium Manganese Oxide batteries are often coupled with Lithium Nickel Manganese Cobalt Oxide to improve their specific capacities and prolong their life spans, giving rise to the LMO(NMC) cells being used for electric vehicles such as the Nissan Leaf and BMW i3 [12]. Figure 2-5 shows the structure of a Li-Manganese cell cathode.

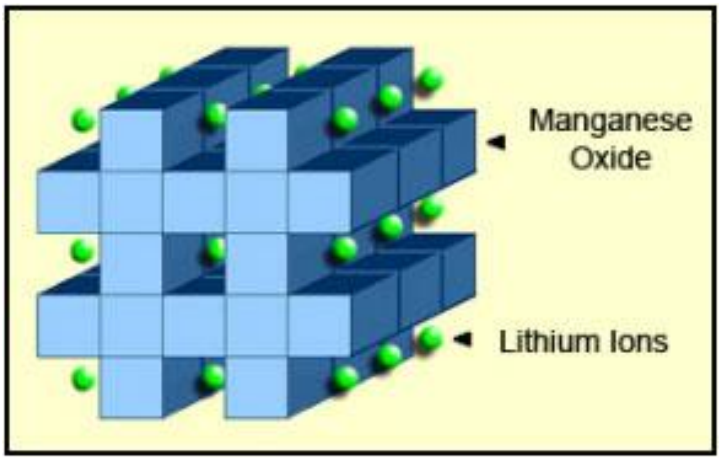

Figure 2-5: Structure of Li-Manganese cell cathode [12]

iii. Lithium Nickel Manganese Cobalt Oxide

Commonly named NMC, these are the batteries of choice in e-bikes, power tools, electric power trains and EVs. The ratios for the cathode combination are equally split between Nickel, Manganese and Cobalt at thirty-three per cent. There are several different combinations of these materials which give rise to cells such as the NCM, CMN, CNM, MNC and MCN. In these combinations, manufacturers often deviate from the thirty-three per cent ratio and keep their own ratios confidential. The best feature of these cells is that they have a high specific energy (capacity) and are the preferred candidate for EV use [12]. The cell that will be studied in this thesis falls under this group and the manufacturer combination for this cell is the NCM. Please refer to the datasheet in Figure 9-8 in the appendix for more information on this cell.

iv. Lithium Iron Phosphate

Lithium Iron phosphate cells have excellent safety features and longer lifespans compared with NMC and Li-Manganese Oxide ones. They also have high specific power capabilities, enabling them to be discharged up to twenty-five times their C rating. However, they have a much lower nominal voltage 3.2V which reduces their capacity to about half of that of the NMC cells. Such low capacities render these batteries only appropriate for lead acid battery replacement as a starter battery and for applications where rapid pulse currents are required.

v. Lithium Nickel Cobalt Aluminium Oxide

The Lithium Nickel Cobalt Aluminium Oxide cells have been used for special applications and have similar advantages to the NMC cells previously mentioned. They also have a reasonably

long lifespan and power. For this reason, these are the current choice of cells used for the Tesla EVs. The drawback for these cells is their high cost and marginally less safety when compared with NMC cells [14].

vi. ***Lithium Titanate***

Lithium Titanate cells have been in use since the 1980s. They have a Lithium Titanate cathode and a graphite anode. This cell chemistry has a low nominal cell voltage of about 2.4V and hence a very low specific energy. They however, have a longer lifespan than ordinary Li-ion batteries such as the NMC and $LiCoO_2$. They can also be fast-charged and offer a high discharge rate of up to about ten times the rated capacity. Lithium Titanate is safer than the NMC cell types. These advantages make the Lithium Titanate very costly [12]. Lithium Titanate cells also do not have an SEI layer and this is the property that allows them to be fast-charged and have a high discharge rate [12].

In 2010, the Boston Consulting Group undertook a study to compare the different chemistries of Li-ion cells. The following diagram is a comparison of the above six chemistries and compares them in six different areas which are specific energy, specific power, safety, cost, lifespan and performance.

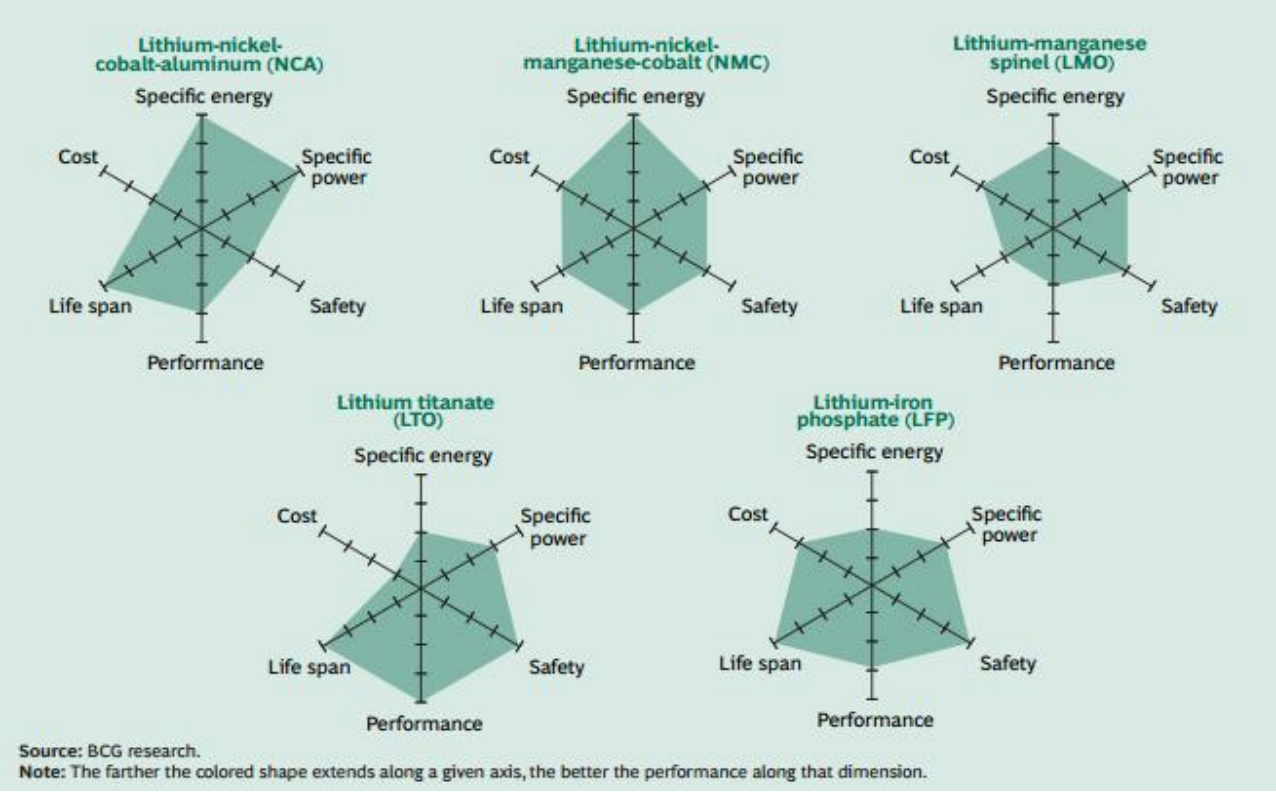

Figure 2-6: A comparison of the different Li-ion cell chemistries [14]

2.2.6 *Li-ion cell shapes and sizes*

Li-ion cells come in four major shapes and sizes. Namely: cylindrical, coin, prismatic and thin-flat cells. The chosen shape of the cell depends on the application. Cylindrical cells for example are used in cameras, laptops, toys and wall clocks. Coin cells are used in watches, hearing aids and medical devices. Prismatic cells are commonly used in mobile phones, tablets and low power laptops, whereas the thin-flat cells also referred to as pouch cells, are commonly used in automobile and military applications [12]. Figure 2-7 shows the different shapes of Li-ion cells.

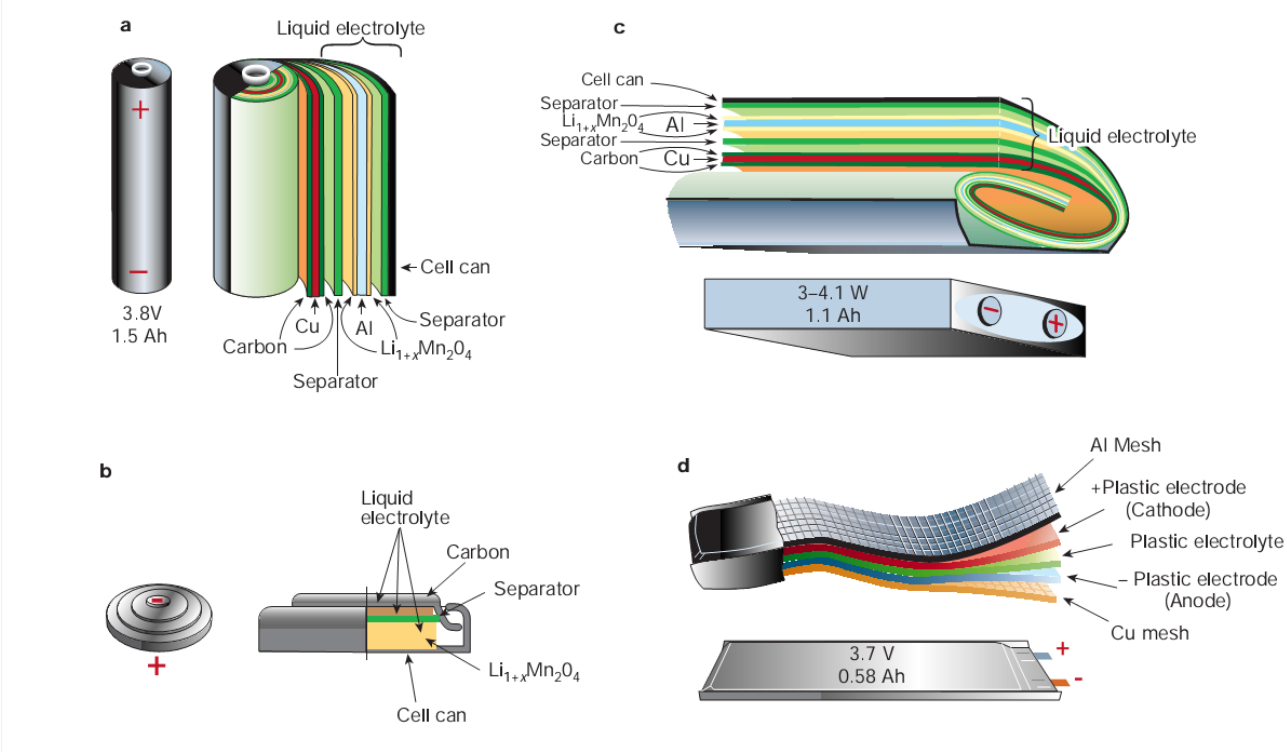

Figure 2-7: Schematic drawing showing the shape and components of various Li-ion cell configurations: a. Cylindrical; b. coin; c. prismatic; d. thin and flat [12]

2.3 Modelling of the Li-ion Battery

To diagnose Li-ion batteries, one needs to adequately choose a model for the battery. Furthermore, the model must be compared against the physical system to validate it. The validity of the model is a measure of how well it compares with the actual physical cell. The choice of model for the battery is dependent on what parameters are being tested. There is also a trade-off between complexity of the model and the speed of the model, in predicting the battery performance. There are several categories of models for the Li-ion battery. These are explained below.

2.3.1 Electrochemical models

The electrochemical model is one that breaks down the cell into different regions and uses mathematical equations to represent the various relations in these regions. The electrochemical model is often also called a mathematical model, because it involves the use of partial differential equations that relate the different relationships between the open circuit potential and the Lithium concentration with the current in the cell, the conservation of charge as well as the Butler-Volmer kinetics [1]. The cell model is usually a 1D spatial model and the cell dynamics are considered only along one axis. The advantage of the electrochemical model is that it can relate design parameters to macroscopic (for example battery voltage and current) and microscopic information (for example concentration distribution) as well as optimise physical design aspects [15], [16]. It is also highly accurate compared with the other models. The key disadvantages of the electrochemical models are: that they are complex and not as robust as equivalent circuit models [15] and that these electrochemical models also require days of simulation time, complex numerical algorithms and battery specific information, that is difficult to obtain because of the proprietary nature of the battery [16]. Figure 2-8 shows the 1D electrochemical model for a Li-ion cell.

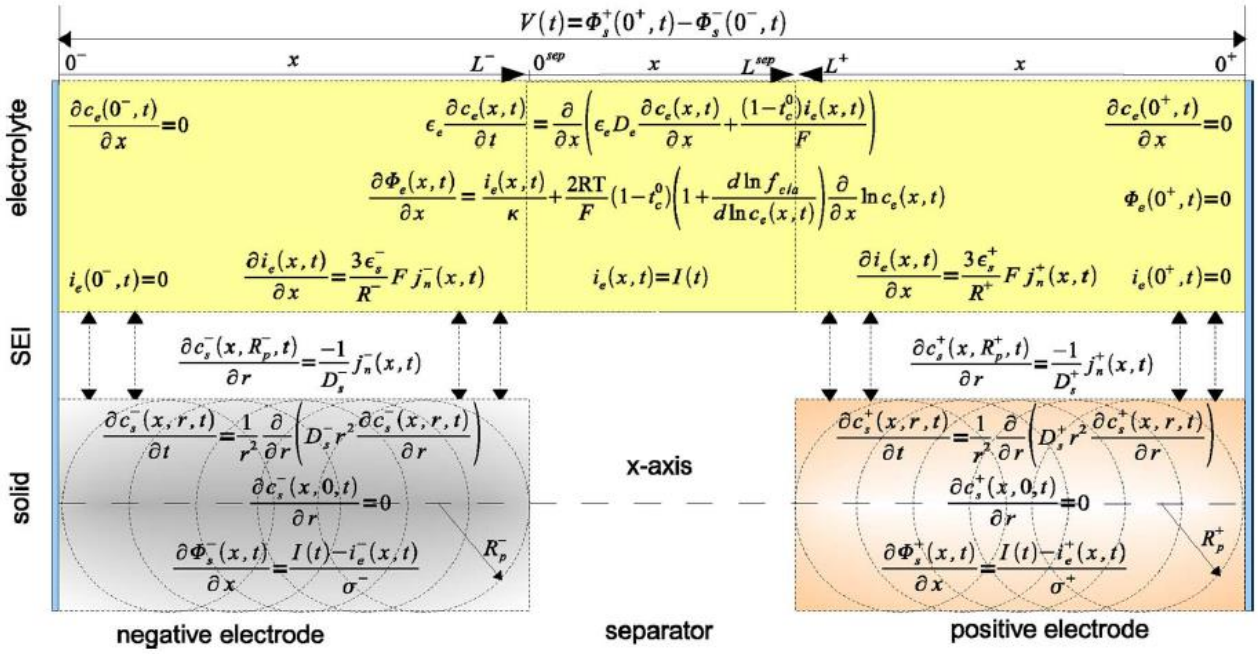

Figure 2-8: 1D electrochemical model of the Li-ion cell [1]

i. ***Mathematical modelling of electrochemical system***

Mathematical models [17], [18], are a more general case of any models that rely on mathematical equations to determine the performance and behaviour of the Li-ion cell. Mathematical models are usually made up of equations that represent a specific aspect of the cell dynamics. Some of these models are based on partial differential equations like the ones in the electrochemical model, whereas others are based on empirical formulae. For the Li-ion cell, the electrochemical model is represented by mathematical equations and thus it can also be called a mathematical model. Models like those used in [19] use mathematical equations to represent the material balance of the Li-ions in the solid/active part of the cell, the electrolyte as well as the interfaces.

The multi-scale model of the Li-ion cells is governed by the following equations.

The material balance for the Li-ions in the active solid material (electrodes) is given by

$$\frac{\partial c_{s,i}}{\partial t} = D_{s,i}\frac{1}{r^2}\frac{\partial}{\partial r}\left(r^2\frac{\partial c_{s,i}}{\partial r}\right) \tag{1}$$

Where $c_{s,i}$ is the concentration of the Li-ions in the solid layer and $D_{s,i}$ is the diffusion coefficient in the solid layer. This equation is given in spherical coordinates because the particles are modelled as being spherical in the solid material regions.

The material balance for the binary electrolyte in the liquid phase(electrolyte) is given by:

$$\varepsilon_i\frac{\partial c_i}{\partial t} = \frac{\partial}{\partial x}\left(D_{eff,i}\frac{\partial c_i}{\partial x}\right) + (1 - {t_+}^0)a_i J_i \tag{2}$$

Where $D_{eff,i}$ is the diffusion coefficient, a_i is the electrode surface area per unit volume of the electrode and J_i is the flux of Li-ions away from the surface of the spherical particles.

The charge balance for the solid phase of the cell is given by the following equation

$$\sigma_{(eff,p)}\frac{\partial^2\phi_1}{\partial x^2} = a_i F J_i \tag{3}$$

The charge balance for the liquid phase is also based on Ohm's law and is given by:

$$-\frac{\partial}{\partial x}\left(\kappa_{eff,i}\,,\frac{\partial \phi_{2,i}}{\partial x}\right)+\frac{2RT(1-{t_+}^0)}{F}\frac{\partial}{\partial x}\left(\kappa_{eff,i}\frac{\partial(\ln c_i)}{\partial x}\right)=a_i F J_i \qquad (4)$$

In the above equations, the pore wall flux, J_i , is determined by the Butler-Volmer equation:

$$J_i = k_i\left(c_{s,i,max}-\ c_{s,i,surf}\right)^{0.5}{c^{0.5}}_{s,i,surf}{c_i}^{0.5}\times\left[\exp\left(\frac{0.5F}{RT}\eta_i\right)-\exp\left(-\frac{0.5F}{RT}\eta_i\right)\right] \qquad (5)$$

Equations 1-5 can be applied to cells, to study the various effects of state variables such as temperature and the, state of charge on cells at an electrode level.

2.3.2 Electrical models

Electrical models, unlike the electrochemical models explained above, use a combination of voltage sources, resistors and capacitors for design with other electrical circuits and systems. In these models, the circuit elements are lumped together to represent the DC, AC, transient or run-time behaviour of Li-ion cells These models are simpler to analyse and are relatively faster in the determination of the cell characteristics. In comparison to electrochemical models however, they compromise on accuracy. Therefore, to develop the electrical model such as an equivalent circuit model, the chosen model needs to ensure that the physical cell characteristics that are being investigated are properly accounted for by the circuit elements. For electrical engineers, electrical models are intuitive and are much simpler to deal with compared with electrochemical models. [16]. There are three categories of equivalent circuit models used. These are the Thevenin-based models [20], [21], impedance based models [22], [23], and runtime models [24], [25].

i. Thevenin based models

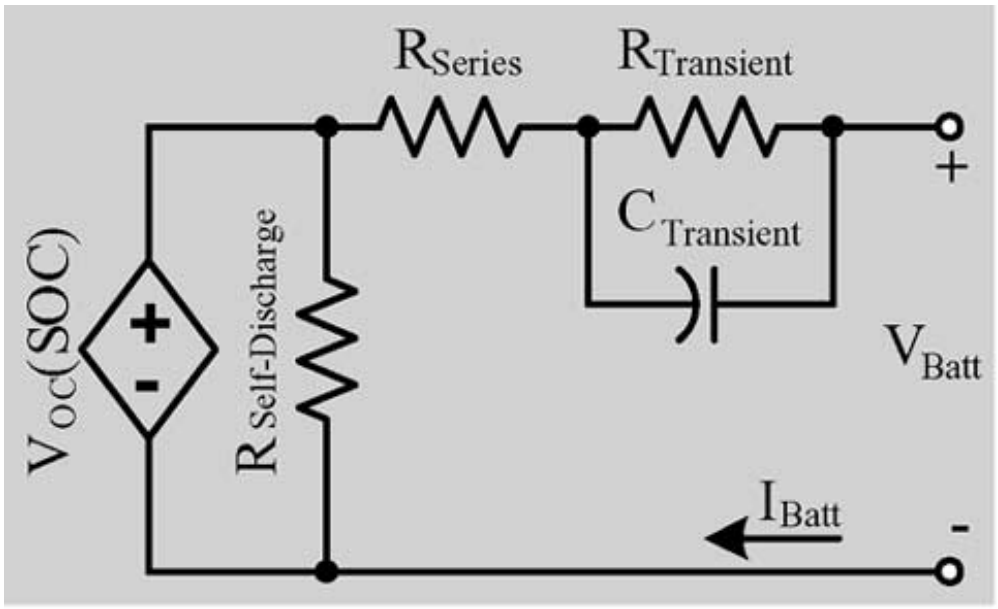

Figure 2-9: Thevenin based electrical model [16]

The Thevenin based model shown in Figure 2-9 in its simplest form uses a combination of a series resistor, and a parallel RC combination to predict the battery state response to a changing load, at a particular state of charge. It does so by assuming the open circuit voltage $V_{oc}(SOC)$ is constant [16].

ii. Runtime based models

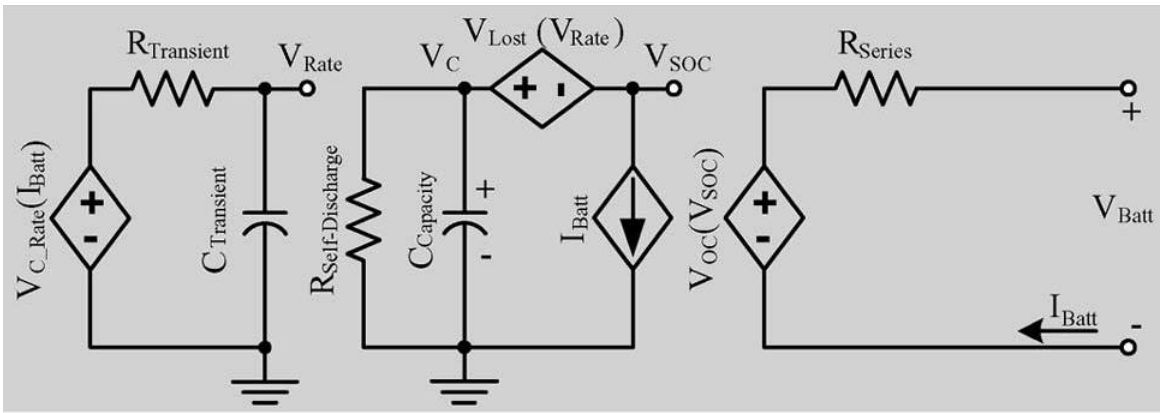

Figure 2-10: Runtime based model of an l-ion cell [16]

Runtime based models such as the ones shown in Figure 2-10 use a complex circuit network to simulate battery runtime and DC voltage response for a constant discharge current in various

simulators such as LT-SPICE and PSPICE. They are the models chosen when runtime information as well as DC performance is required [16].

iii. ***Impedance based models***

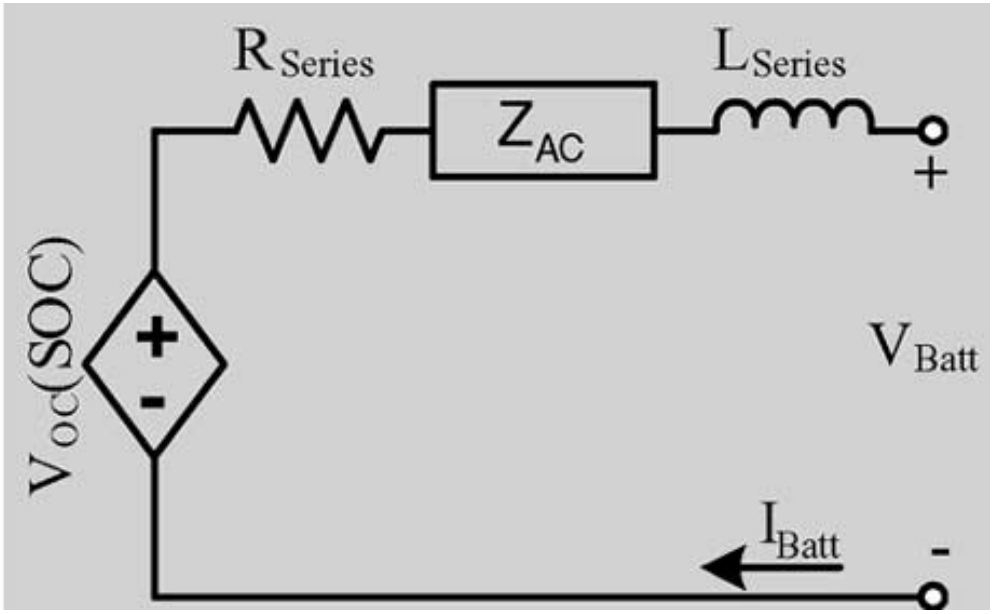

Figure 2-11: Impedance based Li-ion cell model circuit diagram [16]

Of the electrical models, the impedance based models are the most reliable in the determination of frequency response. They are usually represented by a series resistance, together with a combination of parallel RC branches and Warburg elements as shown in Figure 2-11. Impedance based models however, work at a fixed state of charge and temperature, making them less robust than the runtime models [16]. Despite this, the results obtained by applying these models to impedance spectrum data, have recently been used to predict runtime performance on commercial cells in automotive applications [26].

Table 2.1 shows the capabilities of the different models in predicting runtime, DC and AC performance.

Table 2.1: A comparison of the different electrical models

Predicting capability	Thevenin based model	Impedance based model	Runtime based Model
DC	NO	NO	Yes
AC	Limited	YES	NO
Transient	YES	Limited	Limited
Battery runtime	No	Yes [26]	Yes

2.3.3 Artificial Neural network models

Aspects, like the SOC, have been modelled using neural networks. Underlying mathematical models, for example state space models, are superimposed on the neural network [27]. Neural networks however, are designed to overcome the flaws in electrochemical models which limit their ability to predict runtime performance. Instead of state variables, neural networks rely on weighting functions on the neurons. However, they are limited in that they can only be used for the original scope of data with which they were created [28].

2.4 Battery Faults

The diagnosis of faults in Li-ion batteries has seen a growing interest among industry and academic research. The faults associated with batteries can be divided into the following categories:

- Effects due to overcharging/over voltage (>4.2V/cell)
- Effects due to under voltage/over discharge(<2V/cell)
- Effects due to low temperature
- Effects due to high temperature
- Thermal runaway
- Aging and cycling effects

2.4.1 Effects due to overvoltage

If the charging voltage is increased beyond the recommended 4.2V/cell, excessive current flows may give rise to two problems namely:

- Lithium plating
- Overheating

Lithium plating occurs because of overcharging the cell. Li-ions are not able to be accommodated fast enough between the intercalation layers of the anode. This causes the Li-ions to accumulate on the anode and be deposited as metallic Lithium. This reduces the free Li-ions in the cell causing an irreversible capacity loss. Furthermore, the Lithium plating is not homogenous in nature. It is dendritic which means that it can ultimately result in a short circuit between the electrodes.

Excessive current also increases the temperature of the cell and can lead to overheating. This is discussed in the sections below [29].

2.4.2 Effects due to undervoltage

If the charging voltage is decreased beyond 2V/cell, both electrodes can be affected adversely.

At these low voltages, the anode current collector can dissolve into the electrolyte. This then increases the self-discharge of the cell. Furthermore, if the cell voltage is increased to above 2V, the copper ions can then be precipitated and deposited as metallic copper. The metallic copper isn't necessarily deposited on the current collector and hence this gives rise to a potential for short circuits between the electrodes [29].

The cathode is also affected by low voltage. The low voltage can lead to a breakdown in the cathode material into its constituent elements. Lithium Cobalt Oxide cathodes and Lithium Manganese Oxide cathodes are known to release oxygen during this breakdown, eventually leading to permanent capacity loss.

2.4.3 Temperature effects

Li-ion cells are affected by low temperatures as much as they are affected by high temperatures. Low temperatures reduce the rate of reaction, as there is a direct correlation between the rate of reaction and temperature. This in turn reduces the current carrying capacity of the cell. Low temperature operation also means it becomes more difficult for the Li-ions to be inserted in the intercalation layers of the cell. This then causes accumulation of Li-ions onto the anode, in which they can be deposited as Lithium; causing an irreversible capacity loss and increasing the chance of short circuits due to the dendrite nature of the Lithium deposits [29].

High temperature caused in the process of overcharging can lead to thermal runaway as the rate of the chemical reaction is directly proportional to the cell temperature. When positive feedback occurs, the cell is said to be undergoing thermal runaway. It is at this stage that the SEI layer starts to breakdown, causing the electrolyte to react with the carbon anode. This reaction is exothermic and hence continues to increase the temperature of the cell. As the temperature rises, the gases reach a stage where they can be inflamed; however, they are not inflamed because there is no free oxygen in the cell. Some cells are equipped with a vent to

release the pressure build up and prevent the cell from exploding. On further increase in temperature, cathode breakdown occurs.

The effects of both overvoltage and undervoltage are summarised in Figure 2-12.

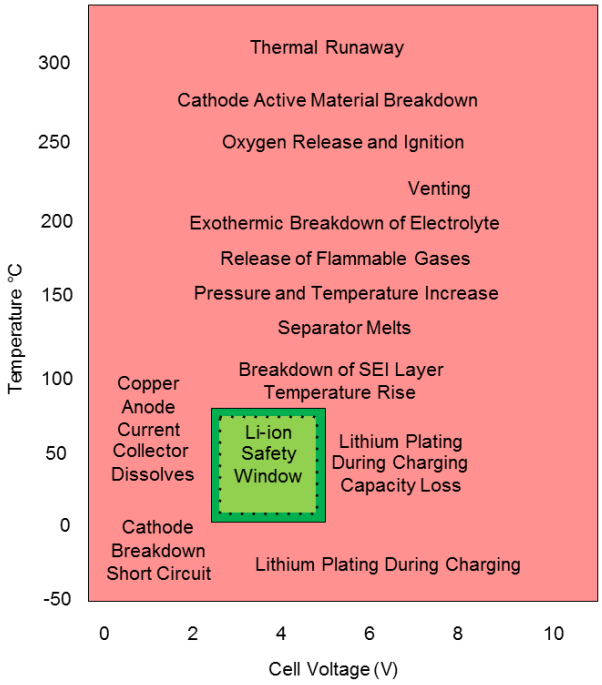

Figure 2-12: Figure showing the different battery faults dependent on voltage and temperature [29]

2.4.4 Mechanical fatigue

Mechanical fatigue results from Li-ions continually being inserted and removed from the intercalation layers of the electrodes. This process causes the expansion and contraction of the electrode, which can lead to cracking in the electrode particles. These stresses then lead to an increased cell internal impedance as the cell ages and in the worst-case scenario a breakdown of the anode SEI layer, which can cause overheating and immediate cell failure. Another scenario is the small release of gas during heat cycling which then causes the cell to swell and ultimately rupture [29].

Cycle life implications

Apart from the fact that operating the cell outside the recommended voltage and temperature windows can result in immediate failure, there are longer term effects that can also result from this such as the shortening of cycle life. Figure 2-13 illustrates the potential number of cycles vs temperature.

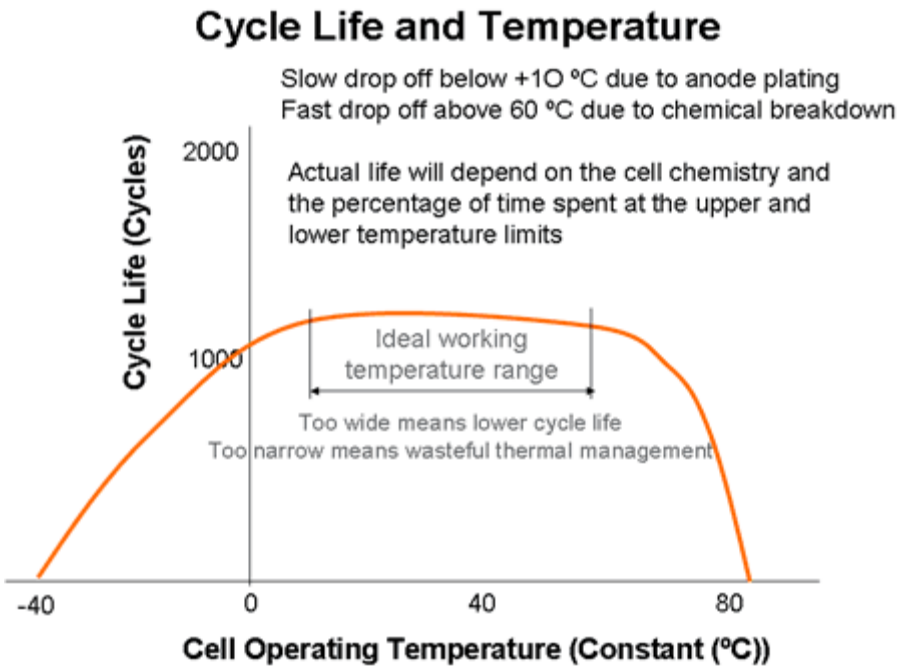

Figure 2-13: Effect of temperature on cycle life [1]

2.5 State of Charge

State of charge determination is a crucial factor in any energy storage application. In the past, batteries were maintained to work within prescribed voltage limits. However, currently several battery management systems exist in different applications. These systems require the battery state of charge to be accurately measured. For this thesis, the state of charge needs to be known for the experiments to be carried out. This section will review the different techniques used to determine the state of charge. This section will also discuss the advantages and disadvantages of the particular state of charge estimation algorithms.

2.5.1 Discharge test

The discharge test is a very reliable method of determining the state of charge of a battery. In this process, the cell is discharged under a controlled current after which it is recharged. This method is however time-consuming and renders the battery unusable during testing [30].

2.5.2 Ampere hour counting with loss calculation

The most common technique for determining SOC: If the initial state of charge is given, the final state of charge is the sum of the initial state of charge and the time integral of the current divided by the rated capacity of the cell [30]. The state of charge is therefore given by:

$$SOC = SOC_0 + \frac{1}{C_N}\int_{t_0}^{t} (I_{batt} - I_{loss})\, dt \quad (6)$$

where C_N is the rated capacity of the cell, I_{batt} the battery current, and I_{loss} the current consumed by the loss reaction [30]. There are two main complications with this method of estimation. The first is that the current measurement needs to be accurate, and incorrect current measurement could lead to significant errors in the SOC estimation. The second major problem is that not all the current measured goes into the charging of the cell. It is also interesting to note that the initial estimate for the state of charge should be accurate.

2.5.3 Measurement of electrolyte physical properties

In non-intercalation cells such as the lead acid battery, the electrolyte takes part in the cell reaction during charge and discharge. There is a linear relationship between the change of the acid density and the state of charge of the cell and therefore the change of acid density can be used to determine the SOC [30]. The measurement of the acid density is measured using a battery hygrometer [29]; however electronic sensors have now been built to determine this as well. This method of state of charge determination can only however be used with vented lead-acid batteries and therefore it is not applicable to Li-ion cells [30].

2.5.4 Open circuit voltage

The open circuit voltage for a cell can be used to determine the state of charge. In some cells, the relationship between the open circuit voltage and state of charge is highly linear. This method of state of charge determination is suitable for applications where there are long rest periods to allow for an accurate OCV measurement. This method is often used in combination with other methods to ensure an accurate state of charge measurement. The challenge with this method is often in applications; a minimal current is required to power monitoring devices,

clocks etc., and therefore the voltage measured is in fact not a true representation of the open circuit voltage [30].

2.5.5 Heuristic interpretation of measurement curves

i. Artificial neural networks

Artificial neural networks have been used to determine the state of charge such as in [31]. The artificial neural networks determine a relationship between input and output data of any kind and therefore they can be applied to all battery systems and in fact all applications, provided that the training data is available [30]. The artificial neural network can be of two types, namely the adaptable and the non-adaptable. In the case of the adaptable neural network, other methods of SOC determination are used to provide the training data at the selected states of operation. Errors depend strongly on the training data and the training method. In the non-adaptable artificial neural network, the training is done before it is used.

ii. Linear Models

In [31] linear relationships were established that show the variation of SOC, the immediate electrical measurements on the battery and the previous SOC value. The equations are as below:

$$\Delta Q(i) = \beta_o + \beta_1 U(i) + \beta_2 I(i) + \beta_3 Q(i-1) \tag{7}$$

$$Q(i) = Q(i-1) + \Delta Q(i) \tag{8}$$

where $Q(i)$ is the state-of-charge, $\Delta Q(i)$ is the SOC-difference, U the voltage and I the current measurement. The factors $\beta_o, \ldots, \beta_3$ are determined from reference data by least-mean-square calculations. The model was developed for PV applications, i.e. for low currents and slow SOC changes. The β-factors do not describe physical parameters. The linear model can be applied to various batteries, all at different stages in their life cycles. However, to achieve the best results, the reference data from the same battery type should be used to calculate the beta factors.

2.5.6 Impedance spectroscopy

Impedance spectroscopy is a common measurement technique that has been applied to various battery systems to determine their state of charge and state of health [30]. The details of this technique will be discussed in the next chapters; however, this section introduces the application of this technique in state of charge determination. In [32], impedance spectroscopy is used with a combination of fuzzy logic. The fuzzy logic is used to establish a relationship between the battery model parameters derived from impedance spectroscopy measurements and the SOC. An accuracy of +/- five per cent was achieved with the above method. It is however important to note that impedance curves are strongly influenced by temperature effects and therefore the best utilization of this method is with batteries in a temperature regulated environment [30]. In [33], it was proven that for the non-standard cells like Li-ion batteries, impedance spectroscopy is a possible SOC determination method. To observe the effect, the SOC has on impedance measurements, low frequencies are however required [30].

2.5.7 Internal resistance

The internal resistance method involves dividing the voltage drop by the change in current during a short time interval. If a time interval of less than 10ms is used, only the Ohmic resistance is measured. For larger time intervals, other effects such as transfer reactions in the case of lead-acid cells are involved and hence the resistance becomes complex [30]. In such scenarios, the impedance spectroscopy method is preferred.

2.5.8 Kalman filter

The Kalman filter is an algorithm that is used to determine the inner states of a dynamic system [30]. For state of charge determination, the battery is the dynamic system, whereas the state of charge is the inner state. A typical model for which the Kalman filter can be applied to determine the SOC is the one shown in Figure 2-14 below.

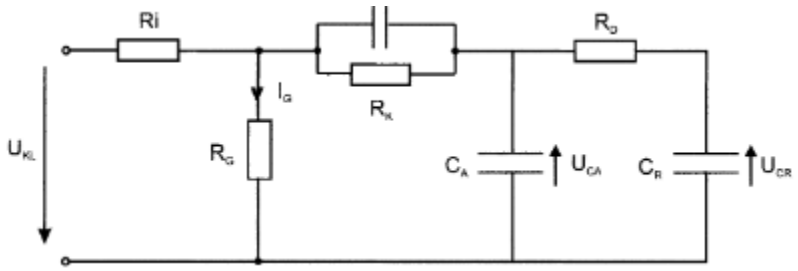

Figure 2-14: HEV model for Kalman filter SOC determination

The table below summarizes the overview of the different state of charge determination methods, highlighting the application areas, advantages and disadvantages of each method.

Table 2.2: Summary of the different SOC determination techniques [30]

Technique	Application	Advantages	Disadvantages
Discharge test	All battery systems for capacity determination in the beginning of life	Easy and accurate, independent of SOH	Offline, time intensive, modifies the battery state, loss of energy
Ah balance	All battery systems, most applications (consumer, PV, EV)	Online, easy, accurate if enough re-calibration points are available with good current measurement	Needs a model for the losses. Sensitive to parasite reactions. Cost intensive for accurate current measurement. Needs regular recalibration points.
Physical properties of electrolyte (density, concentration, colour)	Lead, Possibly Zn/Br and Va	Online Gives information about SOH	Error if acid stratification. Low dynamic. Problem of stability of sensors in electrolyte. Sensitive to temperature and impurities.
Open circuit voltage	Lead, Lithium, Zn/Br and Va	Online, cheap	Low dynamic, error if acid stratification and needs long rest time (current = 0) for lead system. Problem of parasite reaction (for example Sb poisoning by lead)
Linear model	Lead, PV, possibility for other battery systems	Online, easy	Needs reference data for fitting parameters
Artificial neural network	All battery systems	Online	Needs training data of a similar battery
Impedance spectroscopy	All systems	Gives information about SOH and quality. Possibility of online measurement	Temperature sensitive, cost intensive
DC internal resistance	Lead, Ni/Cd	Gives information about SOH. Cheap. Possibility of online measurement	Good accuracy but for only low SOC.

Kalman filter	All battery systems. PV, dynamic applications for example HEV	Online, Dynamic	Needs large computing capacity. Needs a suitable battery model. Problem of determining initial parameters.

From section 2.3, we saw that electrical models were simpler to analyse than electrochemical models, and the different cell characteristics could be accounted for using a combination of circuit elements. Table 2.2 shows that impedance spectroscopy can give information about the state of health of the cell with the possibility of online measurement, in addition to state of charge estimation. Electrochemical Impedance Spectroscopy uses the equivalent circuit electrical model to represent the different cell phenomena and therefore offers the robustness of the electrical models discussed in section 2.3.2. Furthermore, because it is an impedance spectroscopy technique, it can give information about the state-of-health and state of charge changes as discussed in this section. The next sections will therefore explore electrochemical impedance spectroscopy and other impedance spectroscopy techniques with respect to Li-ion batteries.

2.6 Electrochemical Impedance Spectroscopy

2.6.1 Electrochemical impedance

The electrochemical impedance of a battery describes its steady state and dynamic behaviour, which can be seen as its response to an excitation signal of small amplitude. This signal is usually a sinusoidal wave; however, signals like a step, noise or square wave can be used [34].

There are two types of modes that are used to determine the impedance. These are galvanostatic mode and potentiostatic mode.

In **galvanostatic mode**, the DC current I which is sometimes referred to as the polarization current charging or discharging the battery is controlled, and a sinusoidal current:

$$\Delta I = I_{\max} \sin(2\pi f t) \tag{9}$$

at frequency f, is superimposed onto I. This then yields a sinusoidal voltage response:

$$\Delta V = V_{\max} \sin(2\pi f t + \phi) \quad (10)$$

around the DC voltage V at the terminal of the battery. The amplitude $V_{\max}$ and the phase angle ϕ depend on the frequency f [34].

In **potentiostatic mode**, the DC voltage V at the terminals of the battery is controlled and a sinusoidal voltage:

$$\Delta V = V_{\max} \sin(2\pi f t) \quad (11)$$

at frequency f is superimposed to V which then yields a sinusoidal current response:

$$\Delta I = I_{\max} \sin(2\pi f t - \phi) \quad (12)$$

around the DC current I flowing through the battery. In that case, the amplitude $I_{\max}$ and the phase angle ϕ depend on the frequency f. In both cases the impedance is defined by:

$$Z(f) = \frac{V_{\max}}{I_{\max}} e^{j\phi} \quad (13)$$

This equation shows that the impedance of an electrochemical cell can be expressed either as a complex number with both real and imaginary parts or by its magnitude and phase angle ϕ.

2.6.2 Impedance measurement

There are several ways of measuring the impedance spectra obtained. Impedance measurements were earlier measured using AC bridges and lock in amplifiers. Currently impedance measurements are now measured with frequency response analysers. Excitation signals such as white noise have also been used and Fourier transform based frequency analysers were used to analyse the response [34]. The frequency range for a typical measurement is from 10 mHz to 10 kHz [35].

When measuring the impedance spectra of high capacity cells with a low impedance, the connecting leads are known to have a significant impedance, compared to the cell impedance [36]. By increasing the number of leads, the resistance reduces. There are measurement errors caused by the current-sense resistor inside the electrochemical interface (galvanostat or potentiostat) due to the inductive behaviour of resistances lower than 0.1 ohms at high frequencies [35].

Investigations on impedance measurement involve either charging or discharging the battery until the required SOC is reached, giving the cell a sufficient rest period and then measuring the impedance after equilibrium has been achieved. The other technique is to perform the impedance measurement while the cell is charging or discharging [34]. The former technique which involves, charging or discharging a battery to the required SOC and then waiting for a sufficient amount of time is a subject of debate, as authors argue that the processes at equilibrium are different from those involved during charge and discharge [37], and therefore the measurement should be carried out with a non-zero DC current.

There are however errors that are known to appear when carrying out the impedance measurement at non-zero DC current because of the voltage drift. These errors depend on the rate at which the system changes and increases with the measurement period. They therefore become significant for the lowest analysed frequencies [34]. These errors can be suppressed by applying a high pass filter to the current and voltage signals before data processing in the frequency response analyser [38]. Another error suppression technique is to carry out a four-dimensional non-stationary impedance analysis. In this technique, consecutive measurements of a series of impedance diagrams in each frequency range are taken [37].

A summary of the errors in impedance measurement and the mitigation techniques is shown below.

Table 2.3: Impedance measurement errors and mitigation techniques

Error	Cause	Mitigation
Contact Resistance on leads	Measuring impedance of high capacity cells with low impedance with few leads	- Increasing the number of leads for both the current and the voltage measurement [34]
Current sense resistor inductive behaviour	High frequency excitation signal that induces inductive behaviour in the low current sensing resistor in the measurement device	

Voltage Drift	Carrying out impedance measurements at non-zero DC current	- Applying a high pass filter before data processing in the frequency response analyser [38]. - Applying a four-dimensional non-stationary impedance analysis [37].

2.6.3 Impedance diagrams

Impedance diagrams have been plotted in the bode plane i.e. magnitude of the impedance vs. frequency as well as phase angle vs. frequency. They can also be plotted in the Nyquist plane, in which case the plot consists of imaginary part vs. the real part of the impedance. In the Nyquist plane, the electrochemists usually plot the negative of the imaginary part on the ordinate axis, for the capacitive loops to appear in the top right quadrant [34]. A typical Nyquist diagram of a Li-ion battery is shown in Figure 2-15 below.

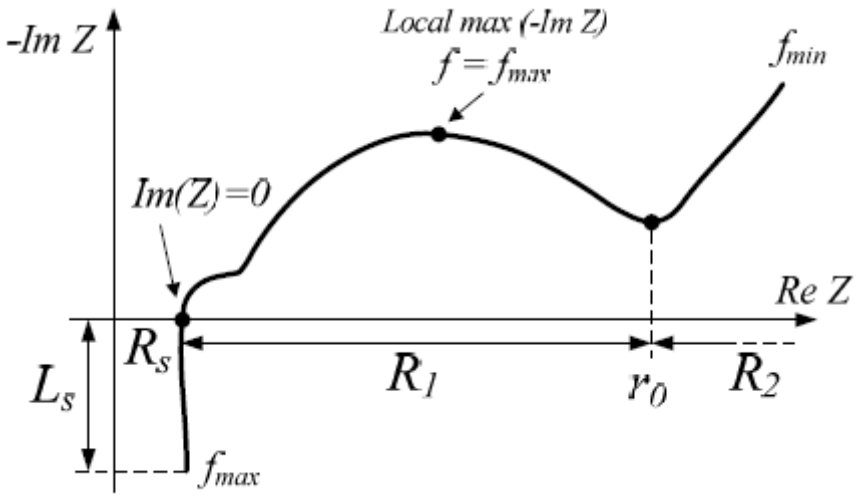

Figure 2-15: Typical Nyquist diagram of Li-ion battery [35]

The impedance spectrum is composed of five distinct regions which in literature are related to different processes. At very high frequencies, the cells inductive behaviour dominates and hence the inductance L_S. The value of the ohmic resistance R_s is found at the intersection of the impedance spectra with the real axis($Im(Z) = 0$). The first semicircle which is the third region is related to the presence of the SEI layer. The larger semi-circle is associated with the charge transfer process and the double layer capacitance. The fifth section which is at the lowest frequencies corresponds to the diffusion process and the impedance is called the Warburg impedance.

2.6.4 Physical electrochemistry and equivalent circuit elements

i. Electrolyte Resistance, R_s

The electrolyte resistance of any ionic solution depends on the ionic concentration, geometry, temperature and type of ions [39]. In a bounded area with area A, resistivity ρ and length l, carrying a uniform current, the resistance is defined by:

$$R_S = \rho \frac{l}{A} \tag{14}$$

In literature [39], [40], this resistance is defined as a function of temperature, giving rise to the equation:

$$R_S = \frac{1}{k} = \frac{1}{A_s} \exp\left(\frac{E_a}{R_u T}\right) \tag{15}$$

Where R_u is the molar gas constant and k represents the reaction rate given by $k = A_S \exp\left(-\frac{E_a}{R_u T}\right)$ modelled as an Arrhenius function [41] of the activation energy E_a and temperature T such that higher T or lower E_a results in a higher value of k.

ii. Double layer capacitance, C_{dl}

An electrical double layer exists on the interface between an electrode and its surrounding electrolyte. This is caused by ions trying to absorb onto the electrode surface. The charged electrode acts like one plate of a capacitor while the ions act as another. They are separated by an insulating space which is often in the order of angstroms [39]. The value of this capacitance depends on many variables such as electrode potential, temperature, ion concentrations etc.

iii. Polarization Resistance, R_p

Polarization is when the potential of an electrode is forced away from its value at open-circuit [39]. In these circumstances, current flows towards and from the electrode surface. The amount of current is controlled by the kinetics and the diffusion of the chemical reactants. The currents

that flow are usually termed as corrosion currents. The relationship between the corrosion currents and the current that flows in the cell is given by the equation below:

$$I = I_{corr}\left(e^{\frac{2.303(E-E_{OC})}{\beta\alpha}} - e^{-\frac{2.303(E-E_{OC})}{\beta C}}\right) \quad (16)$$

where I , is the measured cell current in Amps, I_{corr} is the corrosion current in Amps, E_{oc} is the open circuit potential in volts, β_a is the anodic beta coefficient in volts/decade and β_c is the cathodic Beta coefficient in volts per decade. Even though the corrosion current describes currents in cells whose electrodes corrode, the same equation is applicable even to non-corroding electrodes [39].

Small signal approximation to the above equation introduces the term known as the polarisation resistance as follows:

$$I_{corr} = \frac{\beta_a\beta_c}{2.303(\beta_a + \beta_c)}\left(\frac{1}{R_p}\right) \quad (17)$$

iv. ***Charge Transfer Resistance, R_{ct}***

This is a resistance formed by a single kinetically-controlled electrochemical reaction. When a metal substrate is in contact with an electrolyte, the metal can dissolve into the electrolyte releasing metal ions. During this process, charge is being transferred [39]. This charge transfer reaction has a certain speed. The general relation between the potential and the current is described by equation (5) given in section 2.3.1i. When the overpotential η is very small, and the electrochemical system is in equilibrium, the charge-transfer resistance changes to:

$$R_{ct} = \frac{RT}{iF\alpha}\sinh^{-1}\left(\frac{i}{2i_0}\right) \quad (18)$$

Where R is the gas constant, T is the temperature, α is the transfer coefficient for reduction and oxidation (assumed to be the same for discharge and charge), I the current magnitude, F is Faraday's constant and i_o is the equilibrium current magnitude. From this equation, the exchange current density can be calculated when R_{ct} is known. Since i_0 represents the

magnitude of the exchange current where oxidation and reduction are occurring in equilibrium, it is possible to model it as an Arrhenius relationship as shown below [42].

$$i_0 = \beta e^{\left(-\frac{G}{RT}\right)} \tag{19}$$

Where G is the reaction rate and β is the current coefficient in A.

v. ***Diffusion, Z_w***

The impedance known as the Warburg impedance is known to account for diffusion. It is highly frequency-dependent such that at high frequencies, it is small because the reactants do not have to move very far. At low frequencies, it increases as the reactants must move further. On the Nyquist plot, the infinite Warburg impedance appears as a diagonal line with a slope of 45° [39], [43] .

There are two equations which describe the Warburg impedance. The equation for the infinite Warburg impedance is:

$$Z_w = \frac{\sigma}{\sqrt{\omega}}(1 - j) \tag{20}$$

where ω is the radial frequency, and σ is the Warburg coefficient. The Warburg coefficient is determined by the following equation:

$$\sigma = \frac{RT}{n^2F^2A\sqrt{2}}\left(\frac{1}{C^o\sqrt{D_o}} + \frac{1}{C^R\sqrt{D_R}}\right) \tag{21}$$

where D_o is the diffusion coefficient of the oxidant, D_R is the diffusion coefficient of the reductant, C^o is the concentration of the oxidant in the bulk solution and C^R is the concentration of the reductant in bulk solution.

In practice, the Warburg impedance isn't infinite because of the finite thickness of the diffusion layer.

Cells such as PEM fuel cells rely on the Warburg impedance, which is described as the open boundary finite-length Warburg impedance to model their behaviour.

$$Z_w = R\frac{\coth\left(\sqrt{j\omega\theta}\right)}{\sqrt{j\omega\theta}} \tag{22}$$

Li-ion cells impedance spectra are instead modelled using the blocked boundary finite-length Warburg impedance on the low frequency side.

$$Z_w = R\frac{\tanh(\sqrt{j\omega\theta})}{\sqrt{j\omega\theta}} \tag{23}$$

vi. ***Coating Capacitance***

A capacitor is formed when two conducting plates are separated by a non-conduction media known as the dielectric. The value of the capacitance depends on the size of the plates, the distance between the plates and the properties of the dielectric.

vii. ***Constant Phase Element, Z_{CPE}***

The capacitances in EIS experiments are known to differ from the theoretical ideal capacitors. Instead they behave like a constant phase element as shown below.

The impedance of a constant phase element is expressed as:

$$Z_{CPE} = \frac{1}{(j\omega)^{\psi}\theta} \tag{24}$$

where θ is the capacitance and ψ is an exponent equalling 1 for an ideal capacitor. ψ = 0 represents an ideal resistor.

The ψ parameter is sometimes referred to as a depression constant when the constant phase element is combined in parallel with a resistor, and enables the depression of the associated semicircle on the Nyquist plane associated with the element. The effect of varying the φ parameter is shown in Figure 2-16 below.

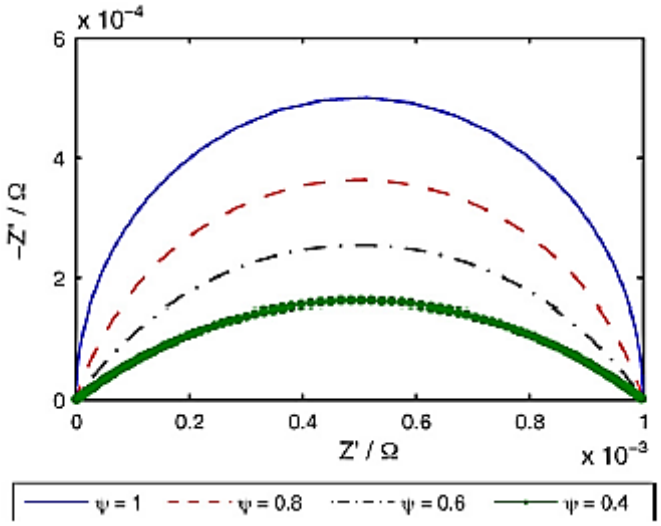

Figure 2-16: Effect of varying the depression ψ on Nyquist plot formed by a parallel combination of a Z_{CPE} and a resistor C = 1kF, R = 1 mΩ [26]

viii. ***Virtual inductor, L_s***

The impedance of an electrochemical cell is known to show inductive behaviour especially at high frequencies. This is usually represented as a virtual inductor.

The above elements all have specific representations in the Nyquist plane and the table below summarizes these representations.

Table 2.4: Table showing the different elements and their Nyquist plot representation [43]

Element list	Impedance formula	Nyquist plot representation
Resistor	$Z = R$	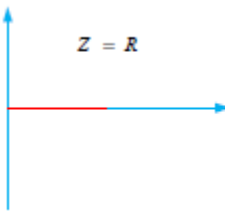
Capacitance	$Z = \frac{1}{j\omega C}$	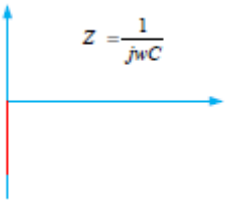
Inductance	$Z = j\omega L$	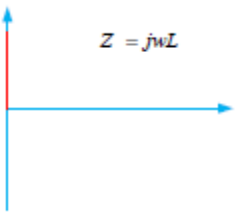

Constant phase element	$Z = \frac{1}{(j\omega)^{\varphi}\theta}$	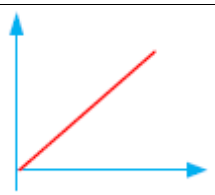
Warburg element for fuel cells (open boundary finite-length Warburg impedance)	$Z_w = R\frac{\coth\left(\sqrt{j\omega\theta}\right)}{\sqrt{j\omega\theta}}$	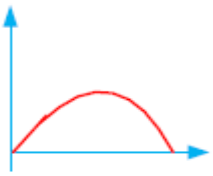
Warburg element for Li-ion cells (blocked boundary finite-length Warburg impedance)	$Z_w = R\frac{\tanh(\sqrt{j\omega\theta})}{\sqrt{j\omega\theta}}$	

2.6.5 *Modelling*

i. Equivalent Circuit Modelling with RC Elements

In this modelling scheme, the equivalent circuit consists of one element per section of the ideal impedance spectrum of Li-ion cells and is displayed in Figure 2-17 below.

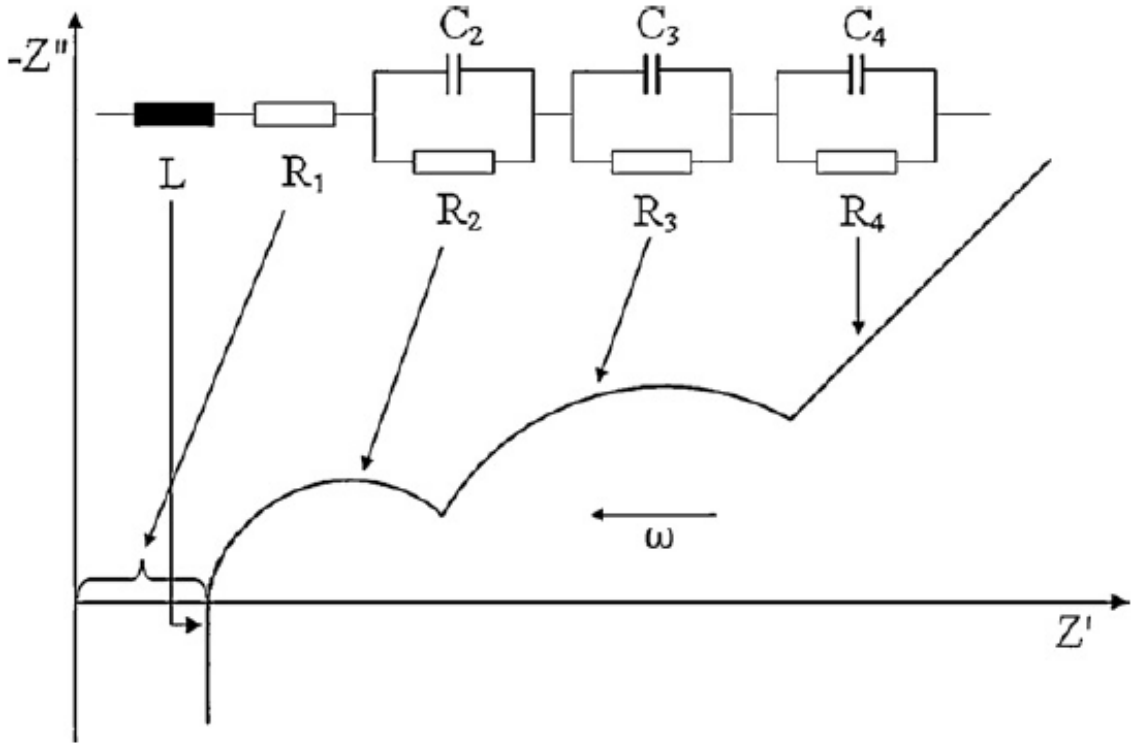

Figure 2-17: Equivalent circuit model of Li-ion cells based on RC components [26]

In this case the equation is given by:

$$Z_{RC} = j\omega L + R_1 + \frac{1}{\frac{1}{R_2} + \frac{1}{j\omega C_2}} + \frac{1}{\frac{1}{R_3} + \frac{1}{j\omega C_3}} + \frac{1}{\frac{1}{R_4} + \frac{1}{j\omega C_4}} \quad (25)$$

The parameters in this equation are estimated and fitted by an optimization algorithm.

ii. ***Equivalent circuit with Zarc and Warburg elements***

Zarc elements as shown in Table 2.4 are a parallel combination of a resistor and a constant phase element. They consist of a generalized capacitance θ and a depression factor. When combined with a resistor in parallel, the impedance of the combination becomes:

$$Z_{Zarc} = \frac{1}{\frac{1}{R} + (j\omega)^{\psi}\theta} \quad (26)$$

where ψ is the depression factor valid between 0 and 1. For ψ = 0, the Zarc element represents an Ohmic resistance whereas for ψ = 1, it represents the ideal semicircle of an RC element. The equivalent circuit representation and its corresponding impedance spectrum is shown in Figure 2-18.

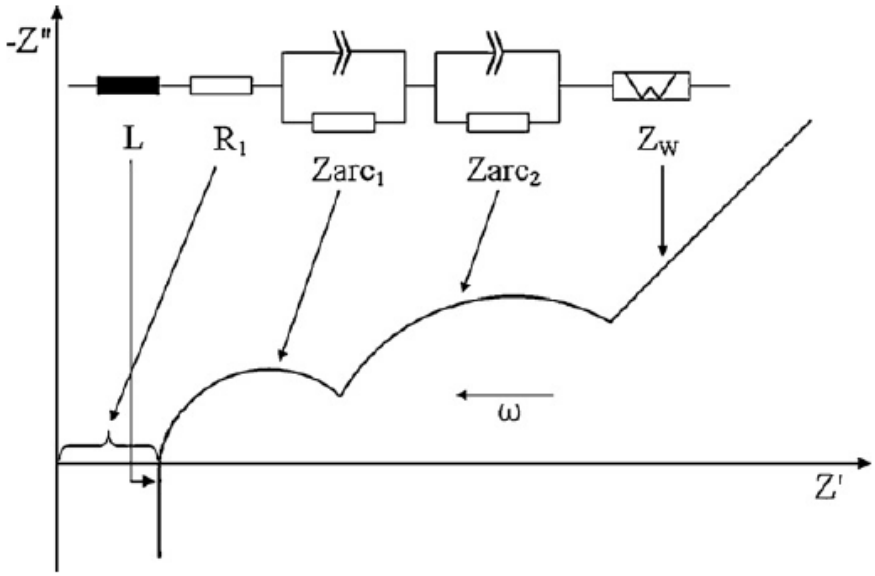

Figure 2-18: Equivalent circuit representation of Li-ion cells based on constant phase elements and Warburg impedances [26]

2.7 Multiple Frequency Excitation

This describes impedance measurement techniques in which multiple frequencies are injected into the test cell. Different signals such as chirps and binary length sequences fall into this category but they are seldom used because they involve the excitation of unwanted frequencies and contain substantial amounts of spectral leakage [6]. The more common techniques therefore involve careful frequency selection and magnitude optimization of the constituent sinusoids. Examples of these are the Compensated Synchronous Detection technique (CSD), the Harmonic Compensated Synchronous Detection technique (HCSD) and the broadband technique that is used in this thesis. A real valued multisine signal can be represented as a Fourier series time domain expression of order N [6].

$$u(t) = \sum_{n=0}^{N-1} a_n \cos(2\pi f_n t + \varphi_n) \tag{27}$$

where N is the number of frequencies in the signal, a_n is the amplitude matrix, f_n are the frequencies to be excited and φ_n is the phase matrix. In the same manner as EIS, the multisine signal which can be a voltage or current signal, is applied to the cell, and the voltage or current response is then measured for each of the individual excitation frequencies. The impedance spectrum is then plotted.

2.7.1 Compensated synchronous detection

The CSD technique [3], [44] involves the injection of sinusoids that are separated logarithmically. The sum-of-sines signal therefore contains multiple frequencies spread over the specified range of interest. For accurate detection with minimal error, it is advantageous to include several periods of each discrete frequency. Multiple studies indicate that a minimum of three periods of the lowest frequency is generally sufficient for this technique when about twelve frequencies are included in the input signal [3], [44], [45]. If more frequencies are used, then more periods would have to be selected to minimize the crosstalk error. The impedance magnitude and phase is synchronously detected by using the input sum of sines current signal which can either be voltage or current, and the output sum of sines signal response. Because the length of the recording is not infinite, the output response sinusoids appear as sinc functions in the frequency domain. These functions can overlap and cause crosstalk error in the frequency domain [3]. Techniques such as the ones mentioned in [46] involve reassembling the

response back into the sum of sines signal in the time domain with all the components except the frequency of interest. The reassembled signal time record is subtracted from the original response signal in the time domain and then synchronously detected again to obtain an accurate impedance spectrum directly comparable to EIS.

2.7.2 Harmonic compensated synchronous detection

The HCSD technique can be analysed as a variant of the CSD technique discussed in 2.7.1. In this technique, the frequencies are selected to be a power of two harmonic of the fundamental frequency. This allows for the impedance measurement to be done within one period of the lowest frequency [3]. Because the frequencies have a harmonic spread, the crosstalk error observed with the CSD approach is eliminated as the sinc function magnitude converges to zero at the frequencies of interest for all sinusoids present in the signal. Figure 2-19 shows a sum of sines signal with two frequency components of 1hz and 4hz and amplitudes of three and two respectively.

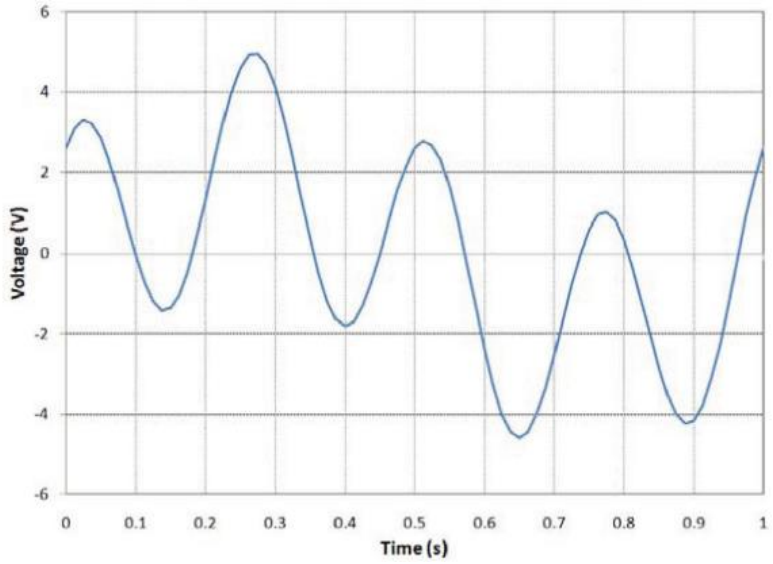

Figure 2-19: Sum of sines output response signal containing two sinusoids with harmonic frequency separation $f_1 = 1Hz, f_2 = 4Hz$[3]

The sinc function sideband magnitude is shown to converge to zero at the frequency points 1Hz and 4Hz which is where the expected output frequency is expected to be measured. Thus, eliminating the need for compensation.

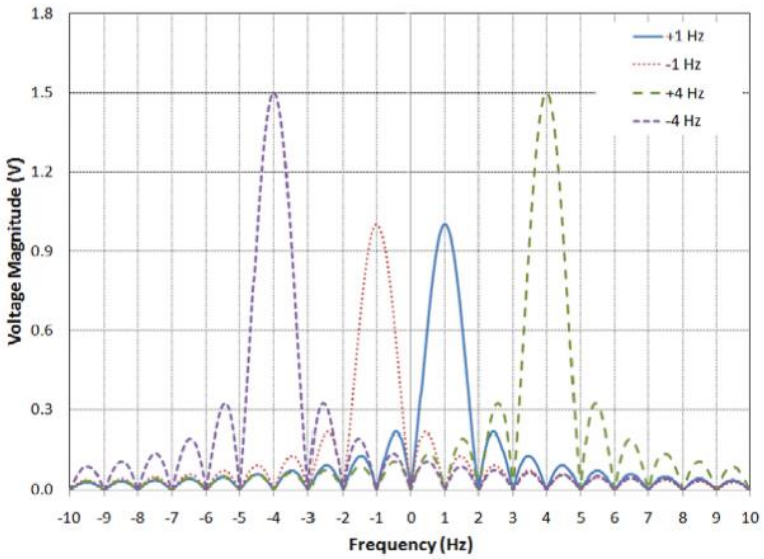

Figure 2-20: Magnitude response for the signals depicted as sinc functions [3].

Although Figure 2-19 and Figure 2-20 show this graphically, the mathematical formulation is expressed in detail in [3].

2.7.3 Other techniques of multisine excitation

Other techniques such as OBIS [6] as well as the custom broadband impedance technique that is discussed in this paper involve careful frequency selection, magnitude optimization and phase optimization techniques that will be covered in detail in the next section.

2.8 Multisine Excitation Optimization

An area in which broadband impedance measurement techniques have been extensively applied is the biomedical industry. In these applications, factors such as a high signal to noise ratio are required to make meaningful tissue measurements. This would involve high magnitude excitation signals with a large crest factor [3]. However, in all these applications, linearity and time invariance should be observed. This then limits the excitation to within certain values. Similarly, the goal in an electrochemical cell is to adjust the conditions including the excitation such that as much information is obtained from the experiment as possible. To achieve this, the excitation signal must be carefully optimised. In this thesis, two broadband techniques are explored, the first being the standard HCSD technique and the second being a modified HCSD technique referred to as BIS. There are three important sections in which the broadband signal can be optimised. These are discussed below.

2.8.1 Amplitude optimization

The first is the amplitude spectrum of the excitation signal. If it is assumed that the input and output noise disturbance is additive and mutually independent with zero mean, then optimizing the amplitude spectrum reduces the uncertainty in the impedance frequency response with independence of the noise level especially at high frequencies (or frequencies with a low SNR). Ultimately, literature suggests the optimal amplitude spectrum of the excitation signal is one which is higher at around the central frequency (where the impedance change is at its maximum) as opposed to a flat spectrum [3]. Care must be taken however to ensure that the higher frequencies further away from the central frequency are also excited sufficiently. The BIS technique proposed in this thesis makes use of amplitude optimization in the excitation signal.

2.8.2 Frequency distribution optimization

A logarithmic spread of frequencies yields the same information as would an equally spaced frequency distribution with a smaller number of excitation frequencies. The disadvantages of an equally spaced frequency spread are that a high number of exciting frequencies are required to determine the entire EIS frequency range without losing impedance spectrum resolution [3]. Equally spaced frequency distributions also yield harmonics that appear at fundamental frequencies. This means that potentially, each excitation signal frequency is interfered by noise from another excitation frequency [3]. Literature suggests that the optimal frequency distribution is one which places more exciting frequencies close to the characteristic frequency. The frequency distribution for HCSD (a power of two harmonic of the fundamental frequency) inherently observes the optimal criteria if the minimum frequency chosen for the excitation is as close to the characteristic frequency of the cell.

2.8.3 Time or phase optimization

Time optimization improves the crest factor of the multi-sine excitation signal. This then allows for more energy to be injected into the cell for a given range of frequencies. To minimize the crest factor, the $l_{\infty}norm$ in the crest factor equation function must be minimized [47]. This norm is however not a differentiable function making its minimization a complex procedure

[48]. Different phase distributions that yield a low crest factor have been applied in literature. These include the Saphiro-Rudin multitones, and the Newman phase multitones.

The phases for the Newman multitones are given by the functions:

$$\delta_k(Newman) = \frac{\pi(k-1)^2}{N} \tag{28}$$

The phases for the Saphiro-Rudin multitones are given by the functions:

$$\delta_k(S-R) = \begin{cases} 0, & r_k = 1 \\ \pi, & r_k = -1 \end{cases} \tag{29}$$

where r_k is the kth element in a rudin sequence explained in [49].

Figures 2-21 and 2.22 show the differences between an un-optimised mutlisine and an optimised multisine sinusoidal signal.

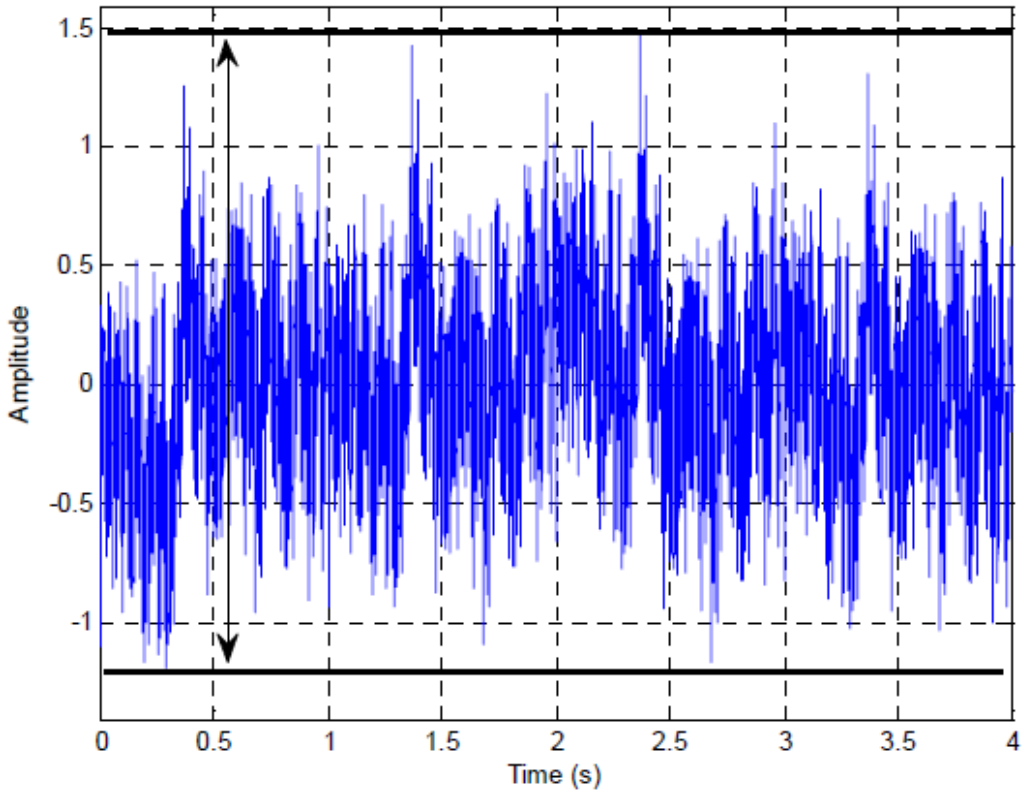

Figure 2-21: Un-optimised multisine signal [6]

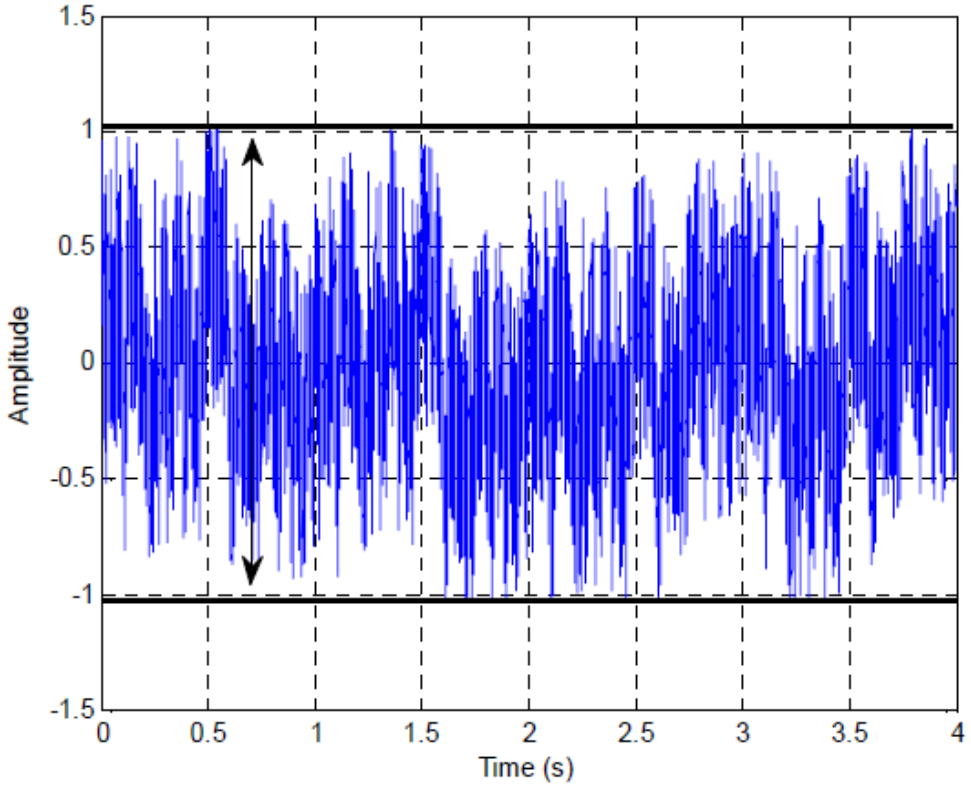

Figure 2-22: Optimised multisine signal [6]

2.9 Impedance Spectra Under Varying Conditions

2.9.1 Varying SOC at a fixed DC bias current and temperature

Some studies for Li-ion cells show a variation in size of the lower frequency loop as the state of charge is increased. This can be seen in Figure 2-23. Hence one can use the size of this loop to predict the state of charge of the cell.

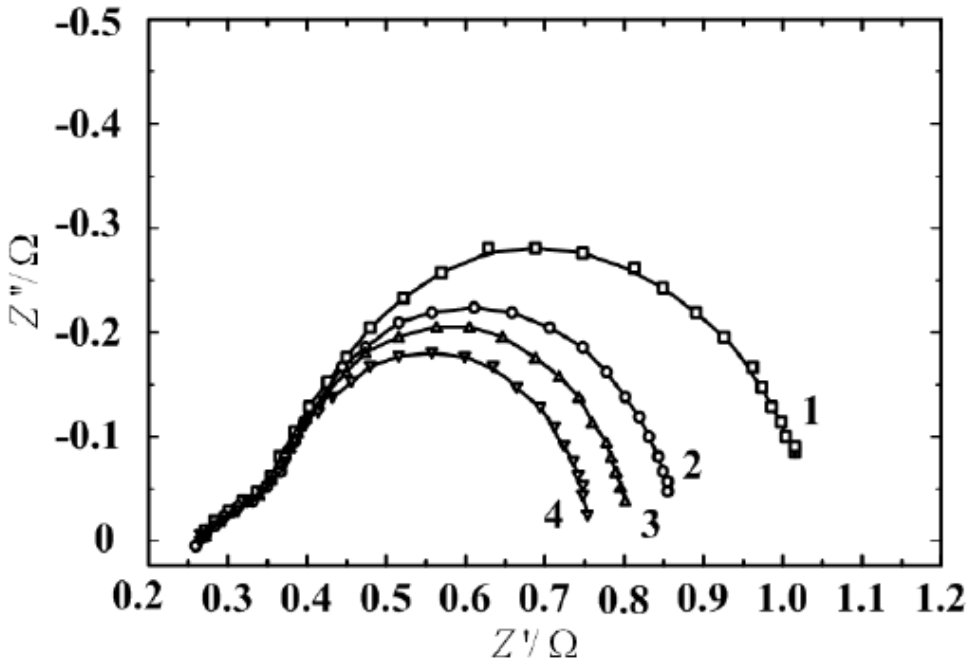

Figure 2-23: SOC variation at fixed DC Bias currents for Li-ion cell where SOC 1< SOC 2 <SOC 3 < SOC 4 [50]

Other studies on other Li-ion cell chemistries show a variation in the higher frequency loop as the state of charge is increased. This is shown in Figure 2-24

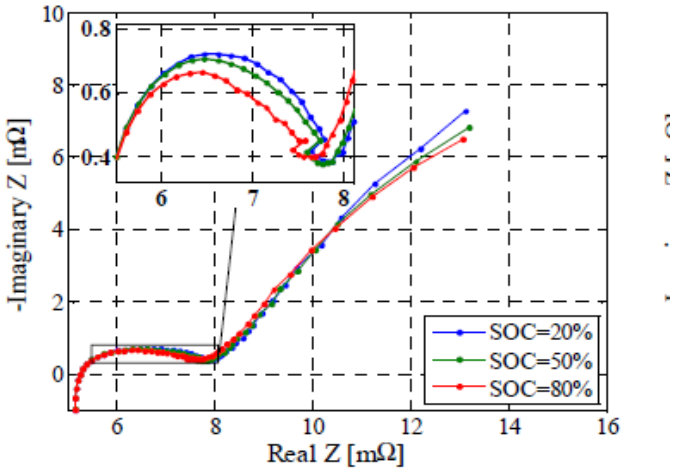

Figure 2-24: Impedance plot variation with state of charge [35]

It is for this reason that one generalized solution is not in fact feasible, and therefore solutions will vary according to the cell chemistry and other factors such as temperature, age, DC bias etc. The general increase in the size of the loops indicates an increase in the impedance of the cell as the state of charge drops.

2.9.2 Varying temperature with EIS at a fixed SOC

EIS at varying temperatures for $LiFePO_4$ cells shows an overall increase in size of the lower frequency loop as the temperature increase. This indicates an increase in the cell impedance as the temperature drops. This is illustrated in Figure 2-25.

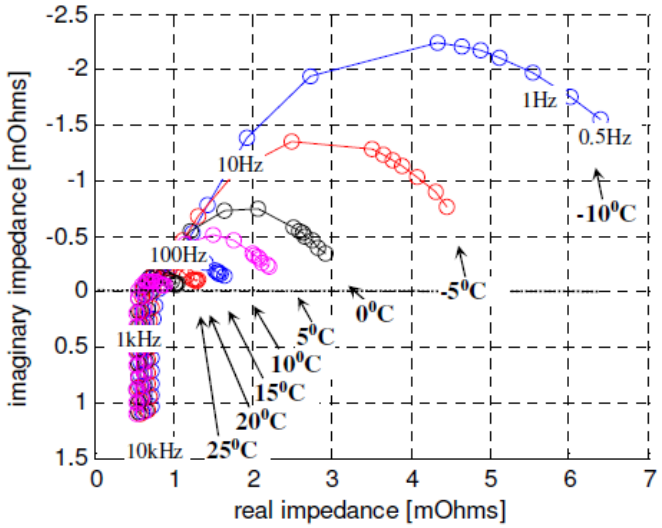

Figure 2-25: Measured results for EIS on a LiFePO4 cell at different temperatures and fixed SOC [42]

Other Li-ion cell impedance spectra are less predictable under varying temperature conditions despite showing an increase in the loop size and hence cell impedance as temperature is reduced. This is shown in **Figure 2-26** below.

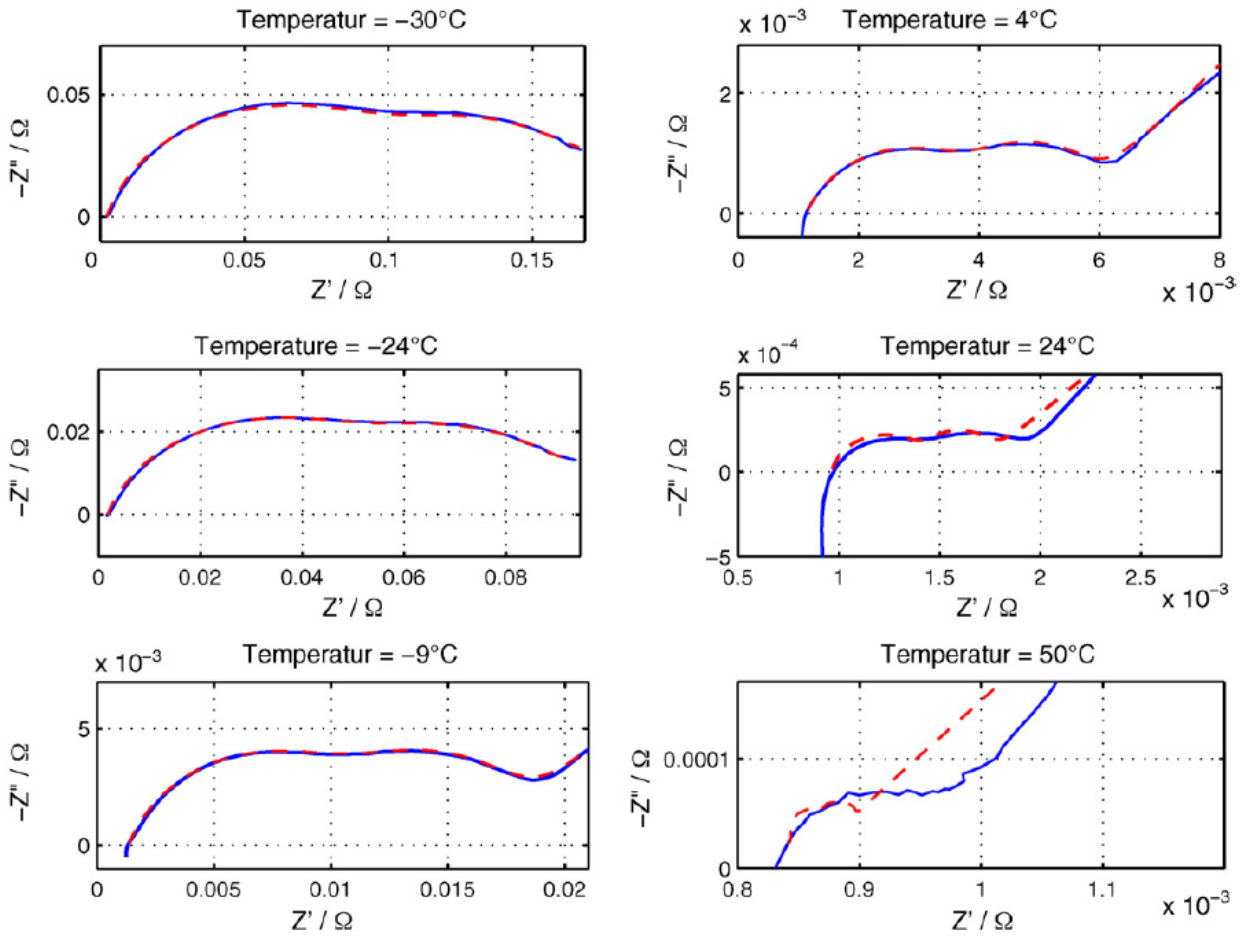

Figure 2-26: EIS spectra under different temperatures and 60%SOC for commercialised high power Li-ion cells (blue) [26]

2.9.3 Impedance spectra with ageing at a fixed SOC and temperature

As the cell ages, the impedance spectra of Li-ion cells tend to shift to the right. This shift corresponds mainly to the increase of the ohmic resistance Rs while the Li-ion battery cell is ageing. These are the most visible trends associated in spectra associated with ageing. In some studies, ageing is directly related to the state of health of the cell. These results are shown in Figure 2-27

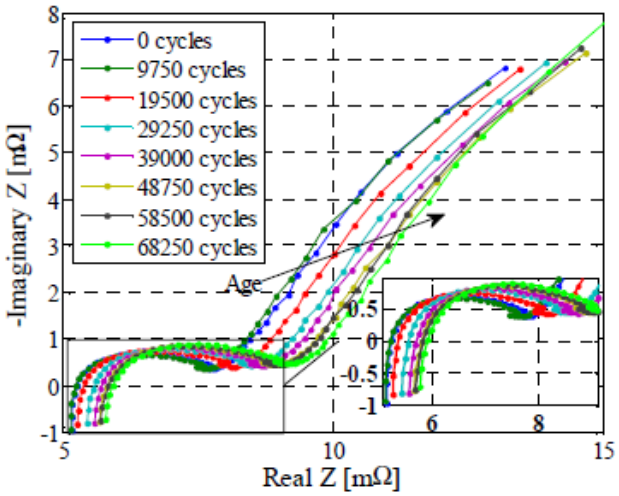

Figure 2-27: Impedance spectra of Li-ion cells after different cycles [3]

2.9.4 DC variation at fixed SOC and temperature

For LiFePO4 cell chemistry, Figure 2-28 shows the EIS results for different DC bias current magnitudes, indicated as a C rate, at 25°C. At this temperature, it is observed that the impedance spectra remain the same for the different dc bias currents. On the other hand, at 0°C, there is a notable change in impedance spectra as the dc bias current is changed This is indicated in Figure 2-29. As the DC Bias current increases, the diameter of the semi-circle reduces. This is significant, since it can be shown that the diameter of the semi-circle ideally equals the charge transfer resistance R_{ct}. From observing these trends, this change in size can be associated with the Butler-Volmer and Arrhenius equations that give rise to the equations in (18) and (19). It can be noted that the lower temperature decreases the value of i_0 calculated using (19) and causes the dependence of R_{ct} in (18) on DC bias current to be more prominent. Because the right side of the EIS trajectories in Figure 2-28 and Figure 2-29 (corresponding to 1 Hz) approaches the x-axis (i.e. zero reactive impedance) for the majority of the test results appearing in these two figures, the value of R_{ct} can be approximately estimated by subtracting R_s (the x-axis intercept of each EIS trajectory) from the value of real impedance measured at 1 Hz.

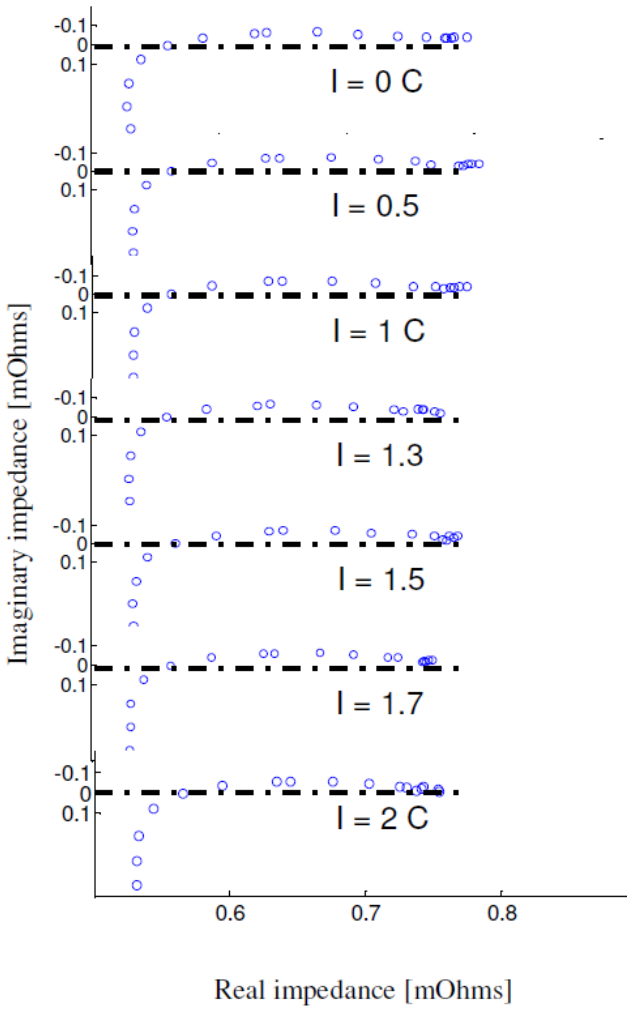

Figure 2-28: Measured EIS spectra for LiFePO4 cells for 7 DC bias currents at 25° C [42]

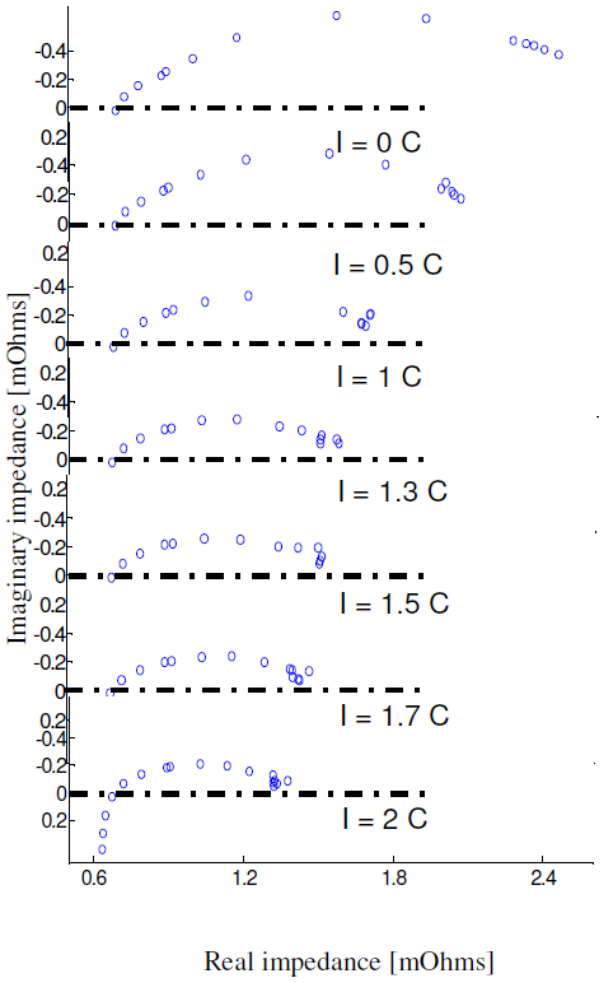

Figure 2-29: Measured EIS spectra for LiFePO4 cells for 7 DC bias currents at 0 °C [42]

3. Hardware Setup

3.1 Overall Setup

The experimental setup for the tests is shown in Figure 3-1. All experiments were carried out at room temperature. The multi-sine signal injection was done using the dSPACE CLP1104 Kit, while the data acquisition device chosen was the NI-USB 6366 device. The electronic load used was the TTI-LD300 voltage controlled load. The cells used were EIG 20Ah CO20 NCM cells. EIS was also performed on the cells and the signal generator was used to produce the single frequencies used to control the TTI-LD300 load.

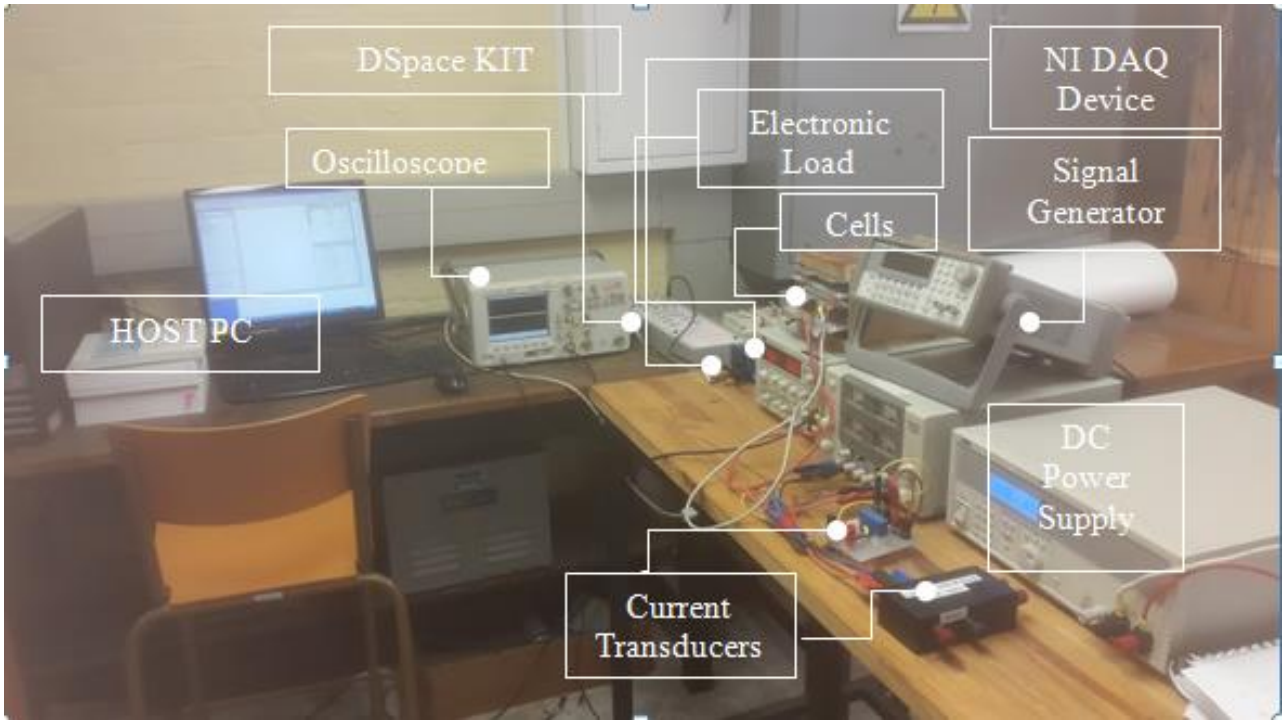

Figure 3-1: Experimental set-up

The block diagram in Figure 3-2 shows the connections between the components used. The multisine excitations as well as EIS were performed in galvanostatic mode i.e. current was the input signal and voltage the response signal. All measurements on the cell were carried out at room temperature. The NI USB 6366 device was used as the data acquisition device. The TTI-LD300 was used as the electronic load as it is supplied with an analog input which can be used to control the current the load draws. MATLAB software was used to create the multisine signals which then used the dSPACE CLP1104 kit DAC converters to supply the TTI LD300 load analog control voltage. The signal generator was used to generate the single frequency sinusoid

for EIS measurements. It was also connected to the analog input of the TTI LD300 load. Both FFT spectral analysis and synchronous detection techniques were used to obtain the voltage response. The connections between the cells, the electronic load and the data acquisition device were kept as short and as close as possible to minimize stray inductances in the impedance measurement. Although HCSD makes it possible to carry out measurements during one period of the lowest frequency [3], [51] , at least two periods of the lowest frequency sinusoid were used in both the BIS as well as the HCSD technique. This was done to improve the performance at the low frequency end of the spectra [3].

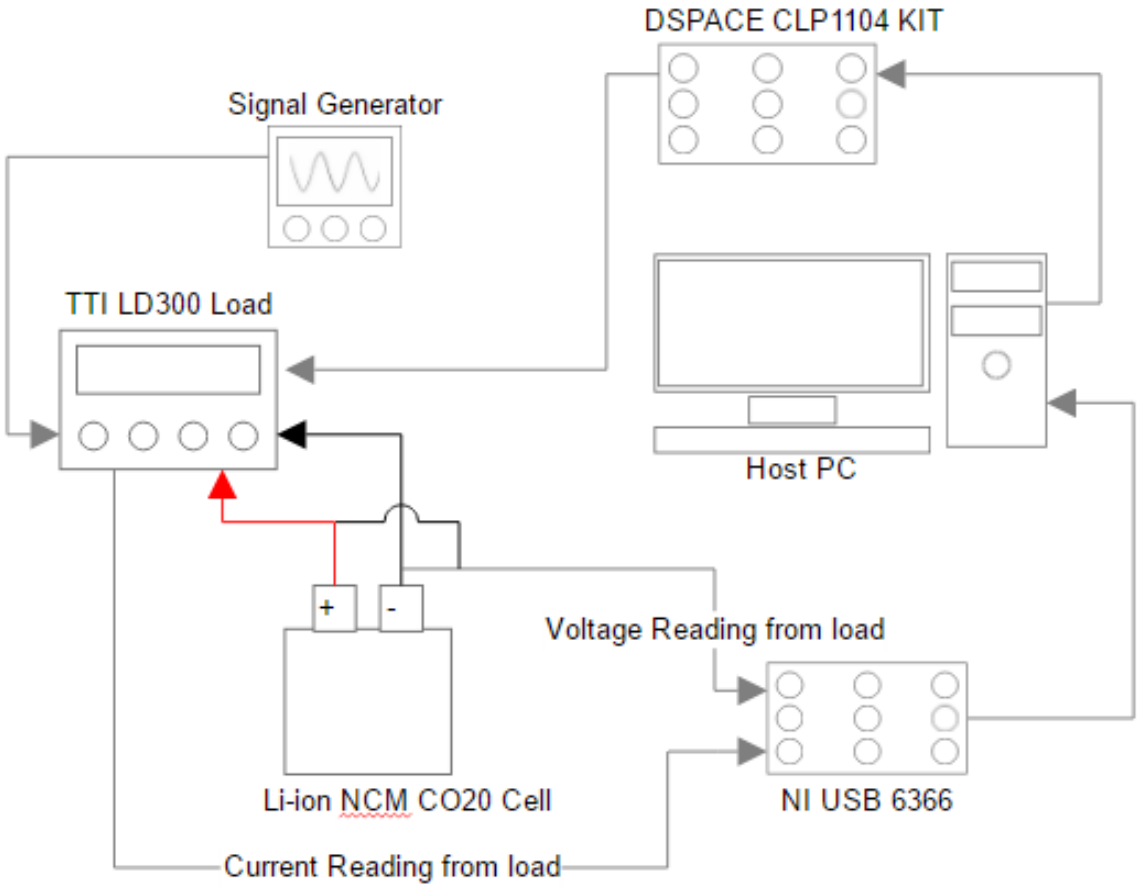

Figure 3-2: Block diagram showing connections between components

3.2 DC Power Supply

The power supply chosen for charging the Li-ion cells was a TTI QPX1200SP power supply. This power supply was found to have flexible voltage/current characteristics, high precision and low noise. Figure 3-3 below shows the QPX1200SP power supply used.

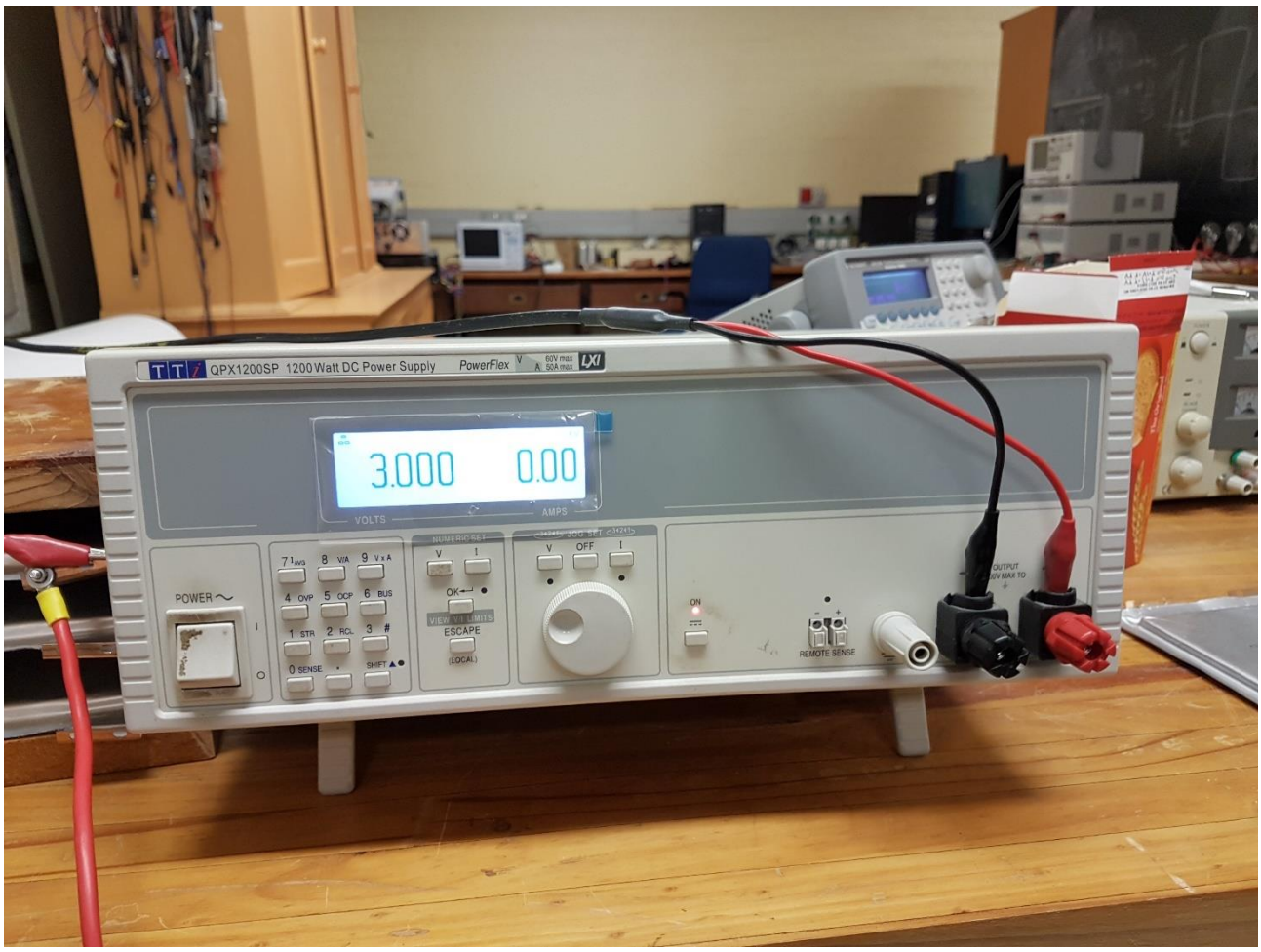

Figure 3-3: QPX1200SP DC power supply

3.2.1 Power envelope

The power characteristics of the QPX 1200SP can be summarised in the power envelope shown in Figure 3-4 below. The power envelope shows the maximum current that can be drawn from the load at a particular voltage. The QPX 1200SP is capable of an output of 60V at 20A all the way to a 20V/50A power combination as described by the power envelope shown.

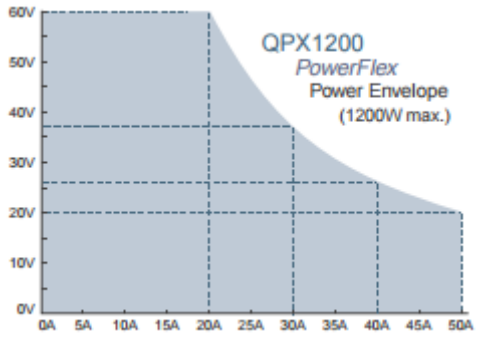

Figure 3-4: Power envelope for the QPX 1200SP power supply [52]

3.2.2 Output specifications and settings

The voltage for the QPX1200SP ranges from 0-60V with a current range of 0-50A. The operating mode switches from a constant current to constant voltage mode with an automatic crossover and indication of crossover. This makes it suitable for Li-ion battery charging.

The voltage setting resolution using the rotary wheel for numeric entry is 1mV whereas the resolution for the current setting is 10mA. The setting accuracy for the voltage is $-0.1\% + /-2mV$, whereas the setting accuracy for the current is 0.3% +/- 20mA. The load regulation is <0.01% +5mV for a ninety per cent load change whereas the line regulation is <0.01%+5mv for a 10%-line voltage change.

For the cells in the experiments, a charge current of 0.2C-0.5C in the constant current phase was employed and since the cells were 20Ah, this corresponded to a charging current of 4A – 10A. The resultant error for the 10A setting according to the formula specified, would be +/- 0.05A or 50mA whereas the resultant error for the 4A constant current setting would be 0.032A or 32mA.

3.2.3 Overvoltage and overcurrent protection

The power supply is fitted with a reverse protection diode. The power supply comes with two configurable overvoltage (OVP) and overcurrent (OCP) setting values. The overvoltage protection is settable from 2V to 65V in values of 100mV whereas the overcurrent protection is configurable from 2A to 55A in 0.1A steps. During charging, the overvoltage was set to 5V to allow for the minimal voltage drop of approximately 0.5V at the terminal of the LD300 load and another 4.2V across the terminals of the battery. Beyond 5V, the power supply would immediately shut down the output.

Overcurrent protection was set to 1C (20A). The current during charging was not allowed to go beyond 1C, however the actual current setting was set on the load side.

3.2.4 Charging setup

The setup for charging the cell is shown in the Figure 3-5 below. The QPX 1200SP power supply was set to a 5V over protection voltage and a 20A over current protection setting. The TTI LD300 load was then set to a constant current mode and then adjusted to constant voltage

mode when the terminal voltage of the cell reached 4.0V, until the terminal voltage reached 4.2V at which point the charging would be stopped.

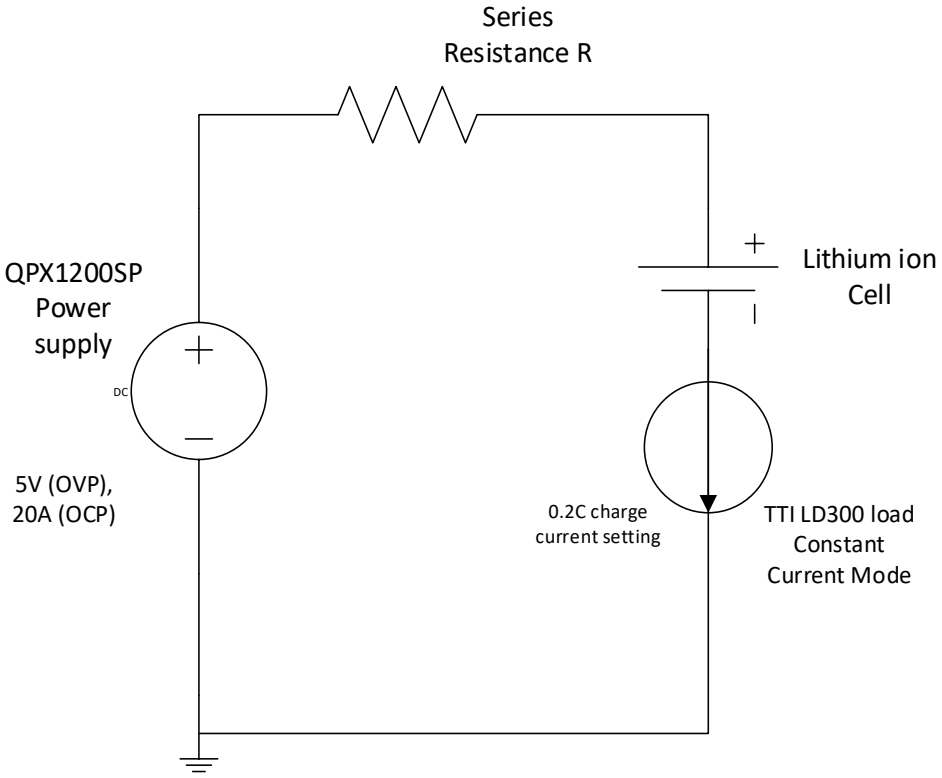

Figure 3-5: Circuit diagram for charging the cells

3.3 Cells

The cells used were ePLB 20Ah Li-ion polymer cells with a $Li(NiCoMn)O_2$ based cathode. These NMC cells are typically used for PHEV and EV applications. They were housed in a wooden container constructed with a dimension of $250mm \times 150mm \times 150mm$ with six cell slots. This is shown in Figure 3-6 below.

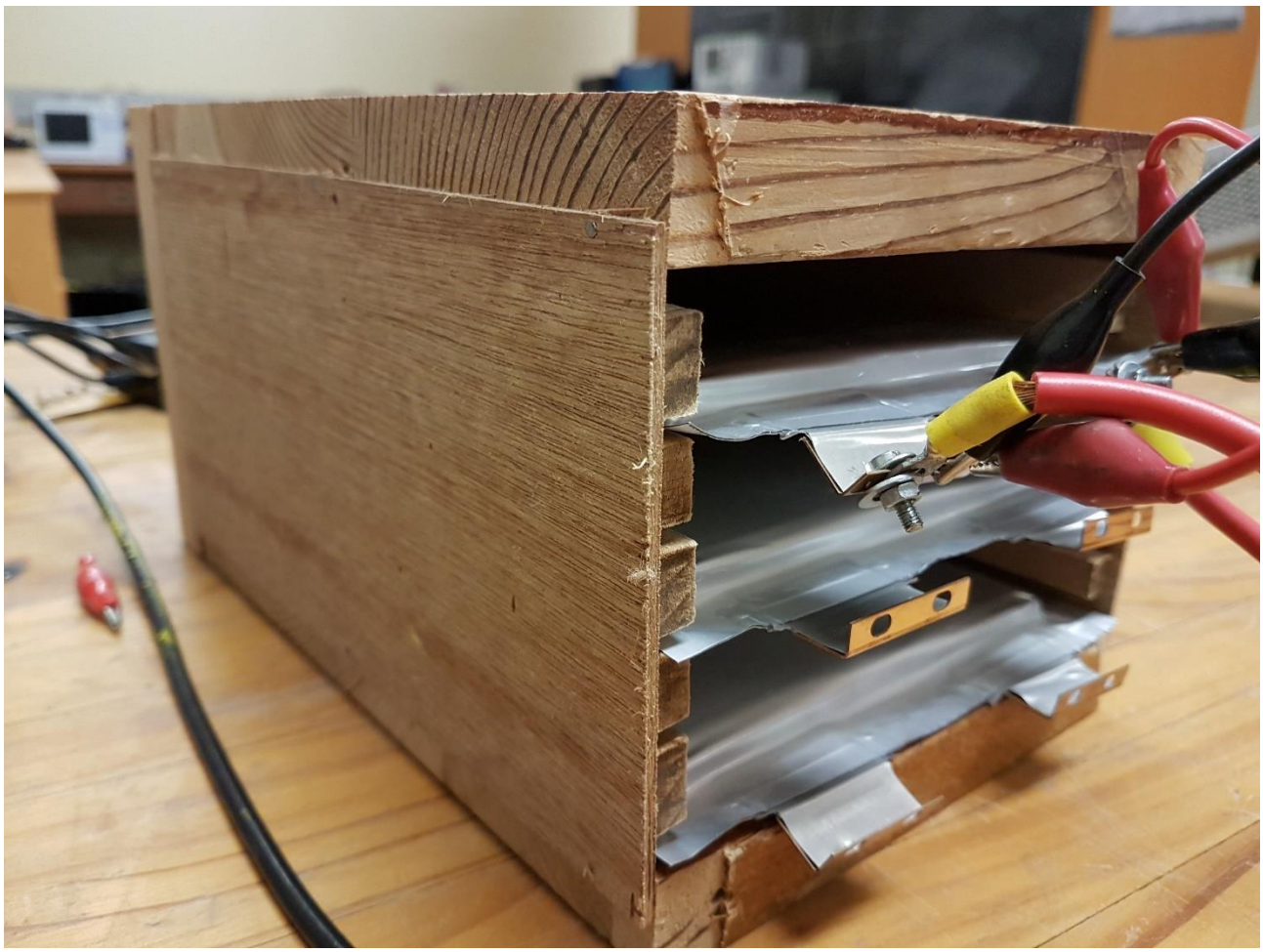

Figure 3-6: Cells with housing

3.3.1 Electrical characteristics

The cells have a nominal voltage of 3.65V and a nominal capacity of 20Ah. The stated 1kHz impedance at room temperature is less than $3m\Omega$. The cells have a specific energy of 174Wh/Kg and an energy density of 370Wh/L. The ten second Specific Power is 2300W/Kg at a fifty per cent depth of discharge, whereas the power density at the same depth of discharge is 4600W/L.

3.3.2 Mechanical characteristics

The cells measure $217 \times 130 \times 7mm^3$ and weigh approximately 428g. This volume excludes the two terminals on the end of each cell.

3.3.3 Operating conditions

i. Charging

The manufacturer recommends a constant current / constant voltage charge method with a maximum charge voltage of 4.15V. The recommended charge current is 0.5C which comes to 10A in this case.

ii. Discharge

The recommended voltage limit for discharge is 3V however the lower voltage limit for discharge is 2.5V. The cell can supply up to a 5C continuous current and up to 10C peak pulse discharge current with the pulse being less than ten seconds duration.

iii. Operating temperature

The cells are to be operated within a $-30°C$ to a $+55°C$ with a recommended charge temperature of $0°C$ to 40°C. The recommended storage temperature of the cells is $-30°C$ to $+55°C$.

3.3.4 Step response and implications of step response on EIS

The objective of these step response tests is to determine how long after charging or discharging the battery will need, to settle to a steady state voltage, before the next EIS experiment is carried out.

The cell was subjected to a step-in voltage during discharge as shown in Figure 3-7. The cell could charge to its full capacity of 4.2V OCV. A constant current of 0.25C (5A) was then drawn from the cell for a period of one thousand seconds, and thereafter stepped down to zero. The resultant effect on the state of charge as well as the terminal voltage is shown in the graphs below. The state of charge was determined using the coulomb counting method. The settling time for a 0.25C step down to zero in current during discharging at a one hundred per cent SOC, was measured to be two hundred seconds for the cell. The purpose of the step response was to help determine the minimum time required between two successive EIS experiments at different states of charge. A two hundred second interval which corresponds to about four

minutes for a 0.25C DC bias current is therefore sufficient, as it ensures the cell's open circuit voltage has reached steady state.

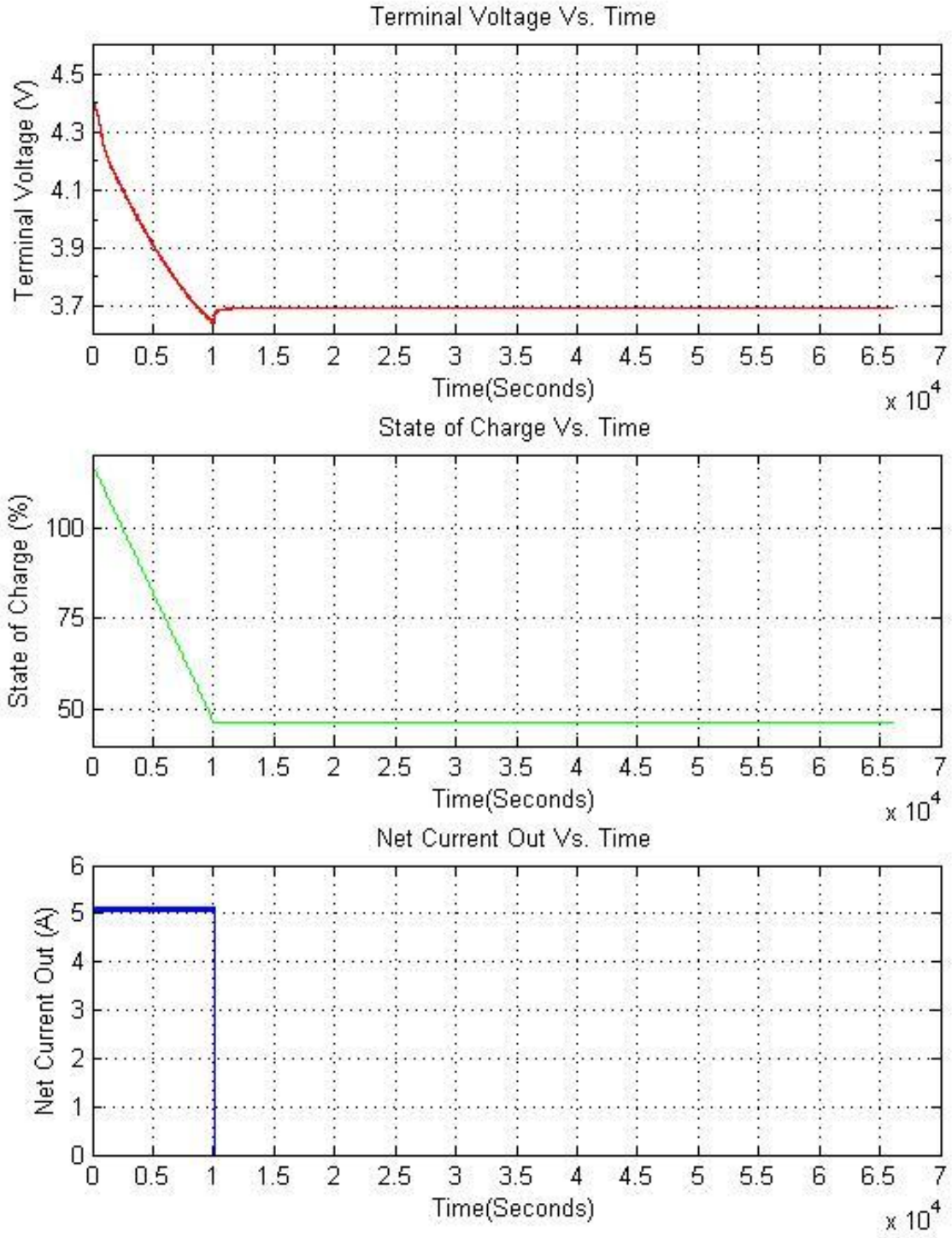

Figure 3-7: Discharge step response of NCM C020 cells

The cell was also subjected to a step during charging as shown in Figure 3-8 below. The cell was allowed to charge at the recommended 0.5C charge current for about three thousand two hundred seconds. The charge current was then stepped down to zero. The settling time for the voltage of the cell was found to be approximately one thousand three hundred seconds.

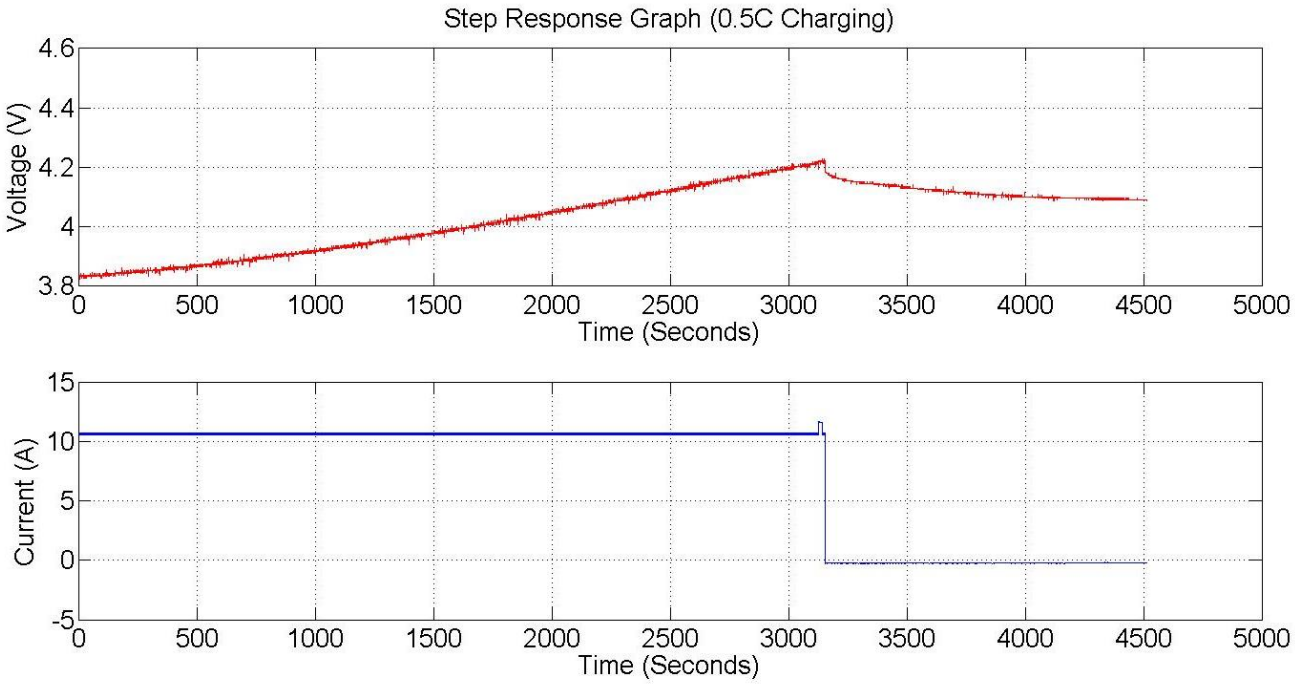

Figure 3-8: Step response after charging at a 0.5C current for the C020 cells

Generally, it was found that the greater the magnitude of the step, the longer the cell would take to reach its steady state open circuit voltage. This settling time was also greatly affected by whether the cell was charging or discharging. The charge settling time is useful in determining the amount of time after charging the cell should be left for the open circuit voltage to reach a steady state, for an EIS experiment to be carried out. It shows that for a 0.5C charge, the cell should be left for at least one thousand three hundred seconds or approximately twenty minutes after charging.

3.3.5 Rate capability

The Voltage Vs Capacity at different discharge rates is shown in Figure 3-9 below. The discharge scheme employed is a constant current discharge to 3.0V which is the recommended minimum discharge voltage. The cell's initial voltage is the recommended 4.15V, and the end of discharge voltage is the recommended minimum end of discharge voltage of 3V.

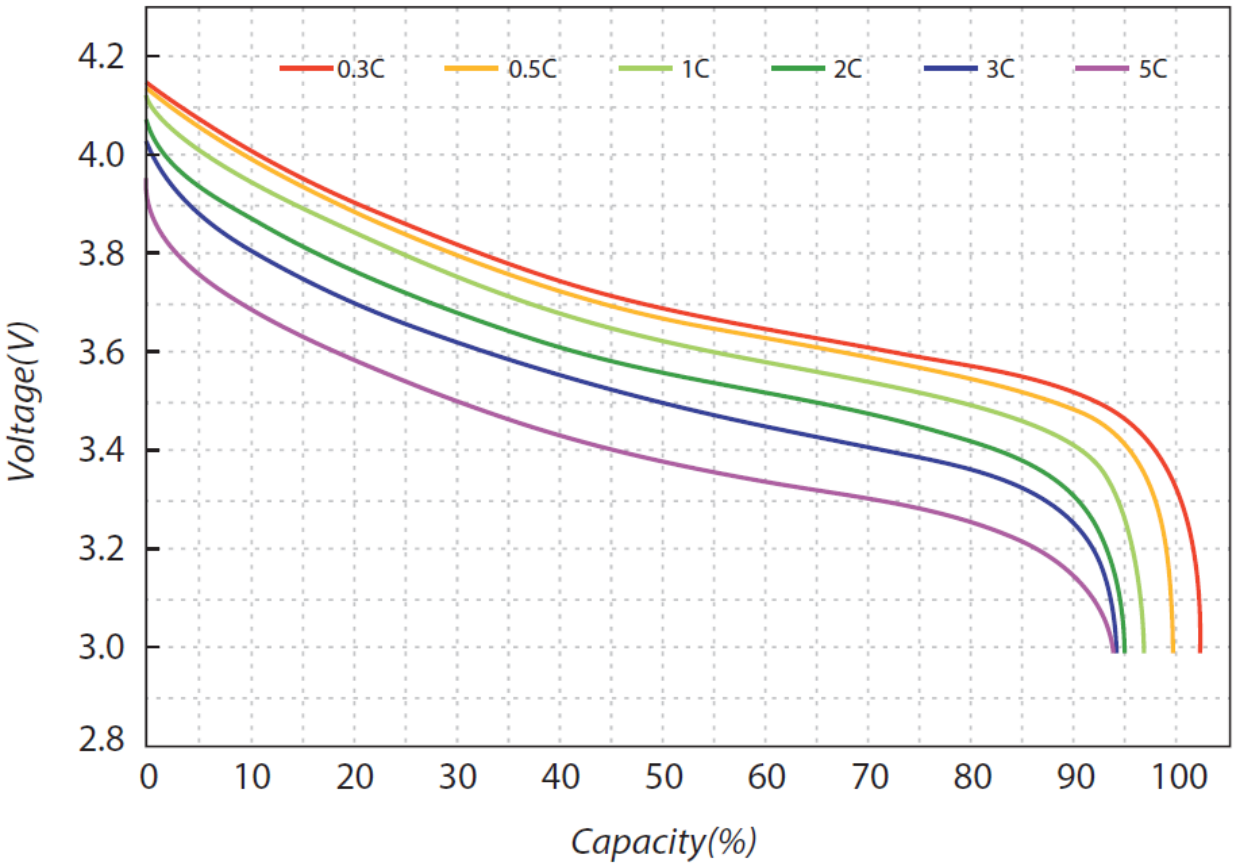

Figure 3-9: Voltage vs Capacity for different discharge currents for the CO20 cells used in the experiments [53]

This graph shows that the cells can only give about ninety-four to ninety-five per cent of their full capacity before reaching their recommended minimum discharge voltage at higher rates of discharge (>=1C). This graph shows that at lower rates of discharge(<0.5C), the cell can give over 100% (~102%) of its rated capacity.

This graph also shows that the magnitude of the initial drop from the open circuit voltage when a constant discharge current is applied, is directly proportional to the discharge current. i.e. the higher the discharge current, the higher the drop and vice versa.

3.3.6 Pulse power capability

The pulse power capability (HPPC) is shown in Figure 3-10 below with the discharge and charge graphs. This is calculated from the FreedomCAR Battery Test Manual. The cell's pulse power performance varies considerably, depending on whether the cell is charging or not, as well as on the depth of discharge. The maximum power density during discharge is achieved at approximately ten per cent depth of discharge, whereas the maximum power density during charging is obtained at a ninety per cent depth of discharge. This is shown in the figure below.

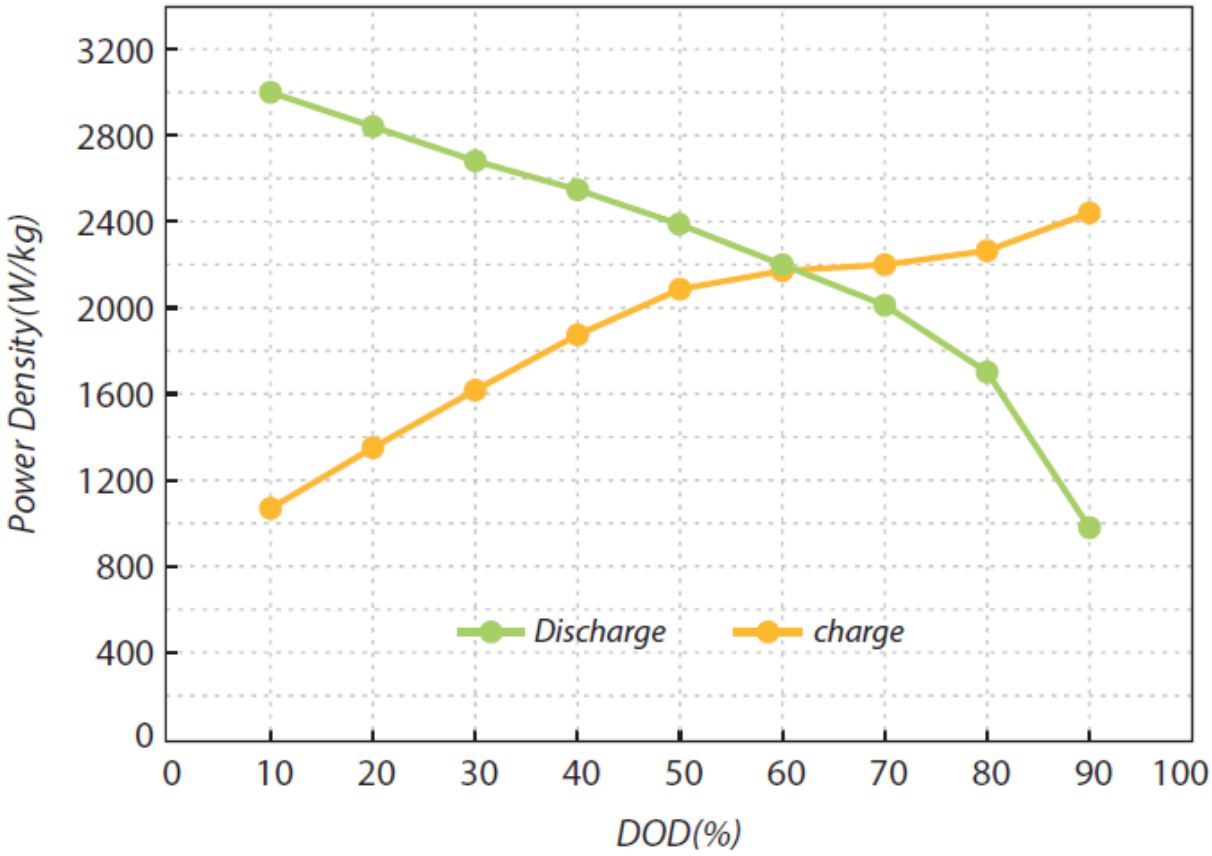

Figure 3-10: Pulse power characteristic of C020 NCM cell used [53]

3.3.7 Cycle life

The cells are designed to undergo about one thousand cycles before their threshold. The capacity retention is heavily reliant on the depth of discharge together with the discharge and charge current. Figure 3-11 shows the cycle life and capacity retention after one thousand cycles when the constant current/constant voltage method is employed for a charge current of 1.0C and an end of charge voltage of 4.15V, as well as when a discharge constant current of 1.0C to 3.0V at room temperature is used. The depth of discharge is one hundred per cent.

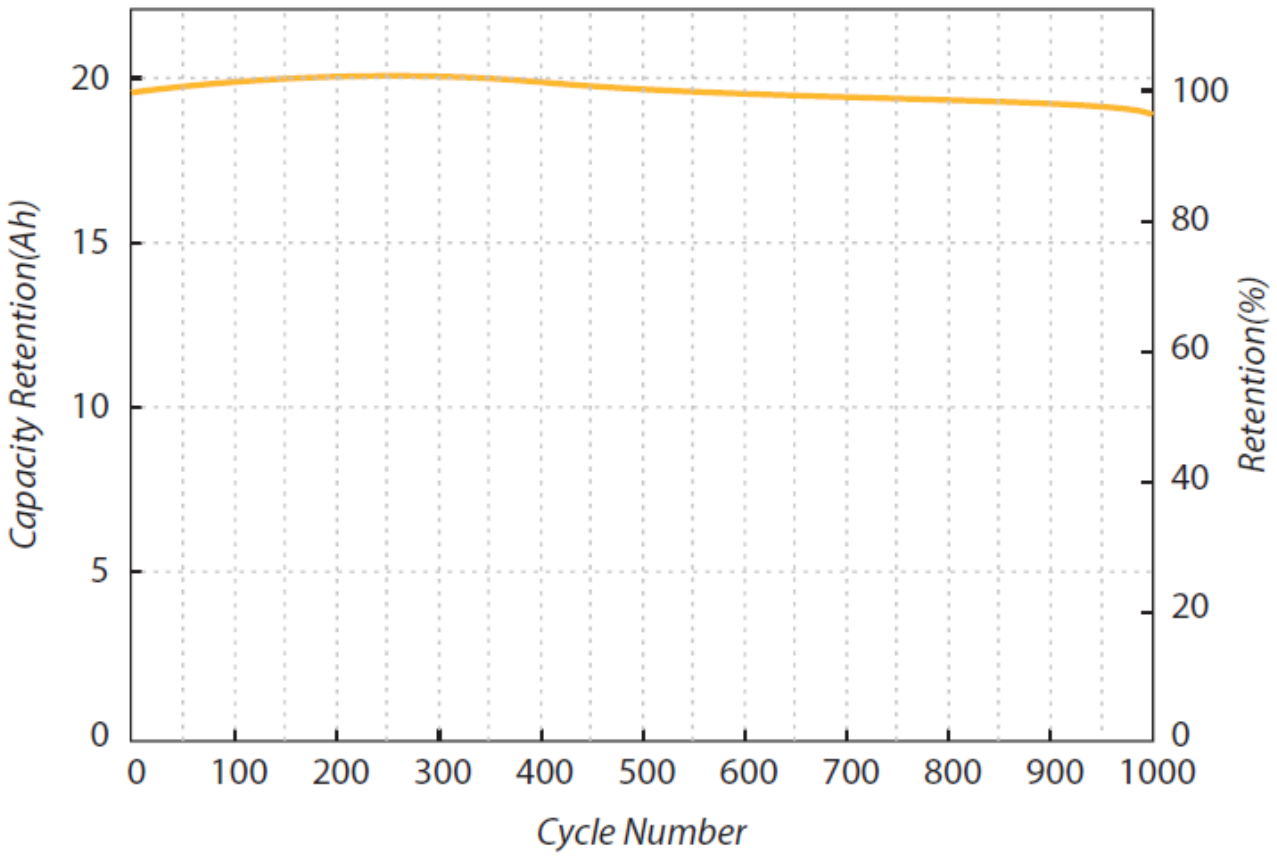

Figure 3-11: Cycle life characteristic of CO20 NCM cell used [53]

3.3.8 Charging and discharge graphs

The charge and discharge graphs for the cells are in Figure 3-12 below. The cell was charged with a constant current (0.5C) and the corresponding graph was obtained.

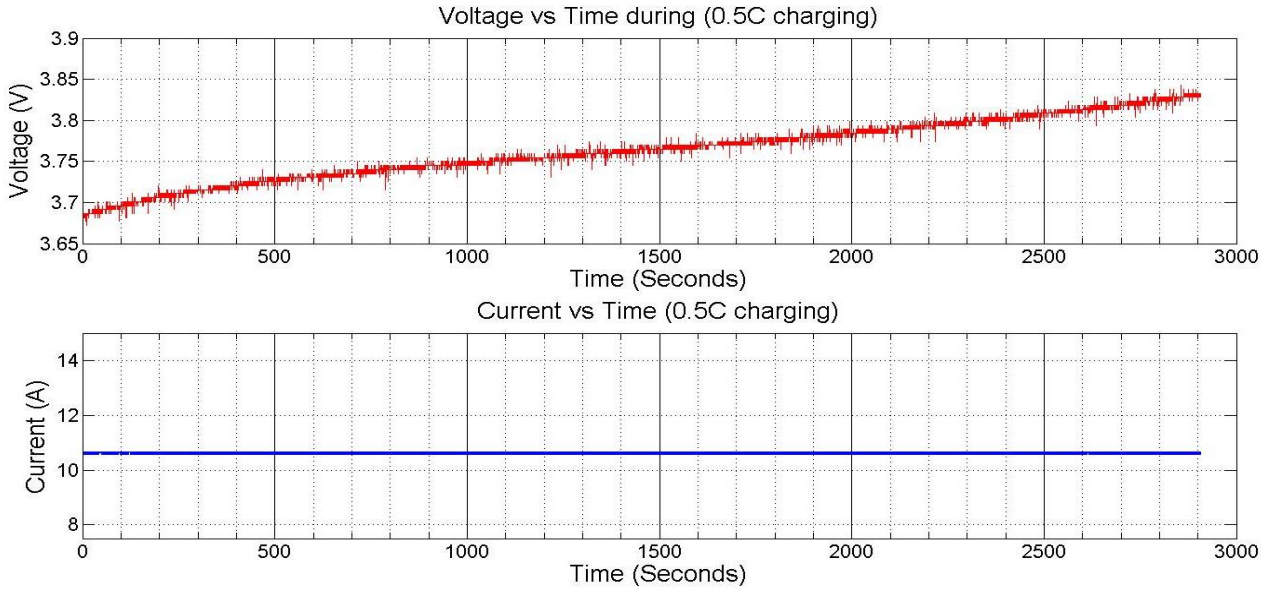

Figure 3-12: Typical charge characteristic graph at 0.5C for the cells

The cell was discharged at 0.25C for a period of about two thousand three hundred seconds which is about forty minutes. The corresponding graph as shown in Figure 3-13 was plotted.

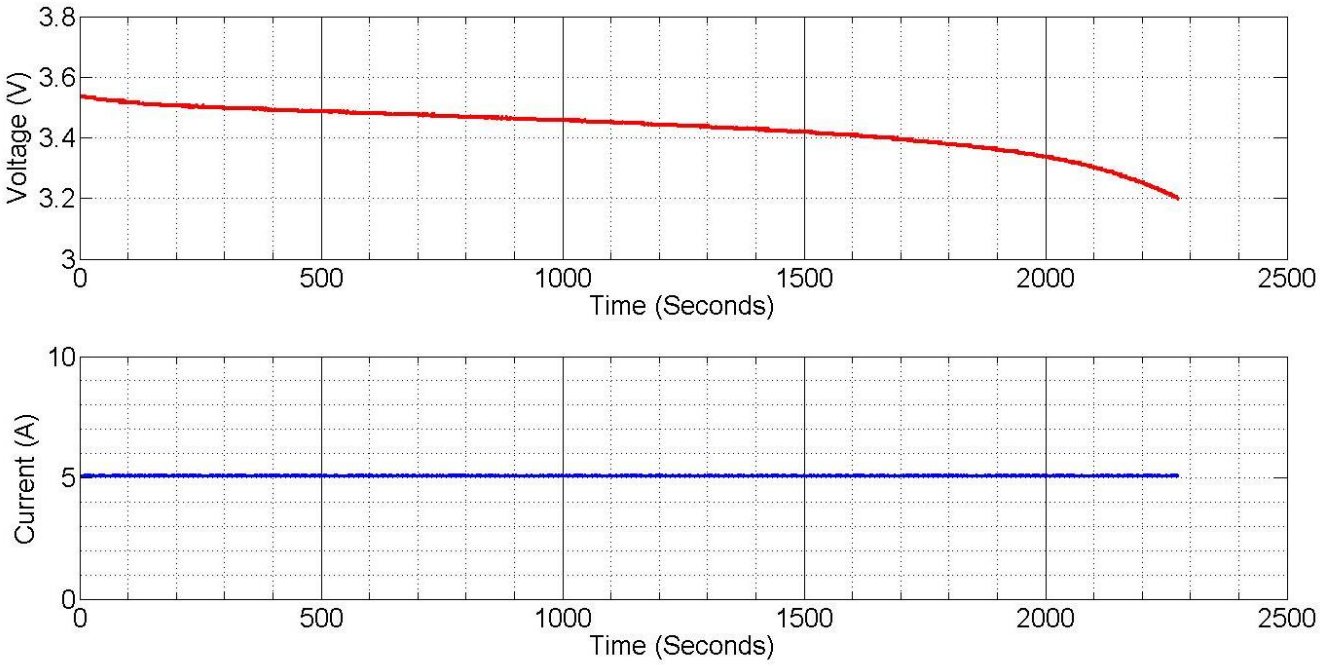

Figure 3-13: Typical discharge characteristic graph at 0.25C constant current for the cells

A typical EIS experiment takes about ten minutes and therefore if the EIS experiment is to be carried out with a DC Bias like the one shown in the above graph, it is critical that the experiment is performed in the linear region of operation.

A ten-minute time interval corresponds to about six hundred seconds. From the above graph, at 0.25C, it can be seen that in a six hundred second interval, the change in voltage corresponds to about 0.05V. Which is approximately 1.4% of the open circuit voltage and thus is small enough to be regarded in a linear region. For even faster methods such as BIS, which is introduced in this thesis, the time exposure is far less than six hundred seconds and therefore the effect of the voltage drift is minimized to a greater degree.

3.4 Signal Injection

The signal injection device chosen was the dSPACE CLP1104 Kit. This device has eight Digital to Analog outputs. The DAC analog output channel was then connected to the input remote control pin of the TTI LD300 load. Figure 3-14 shows the dSPACE kit analog and digital signal connections.

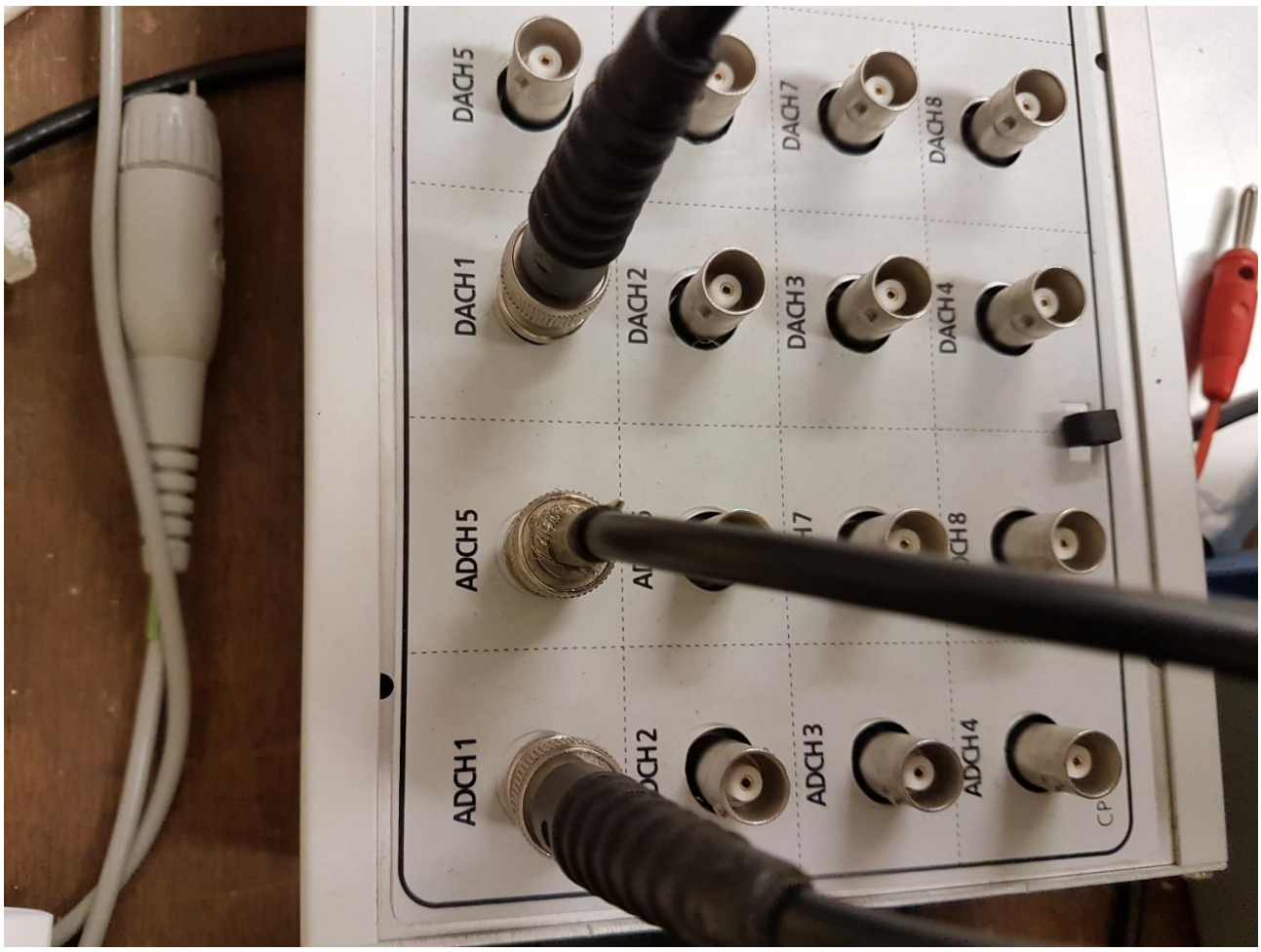

Figure 3-14: Figure of the dSPACE CLP1104 kit used for signal injection

3.4.1 Output electrical circuit

Figure 3-15 shows the simplified diagram of the output electrical circuit.

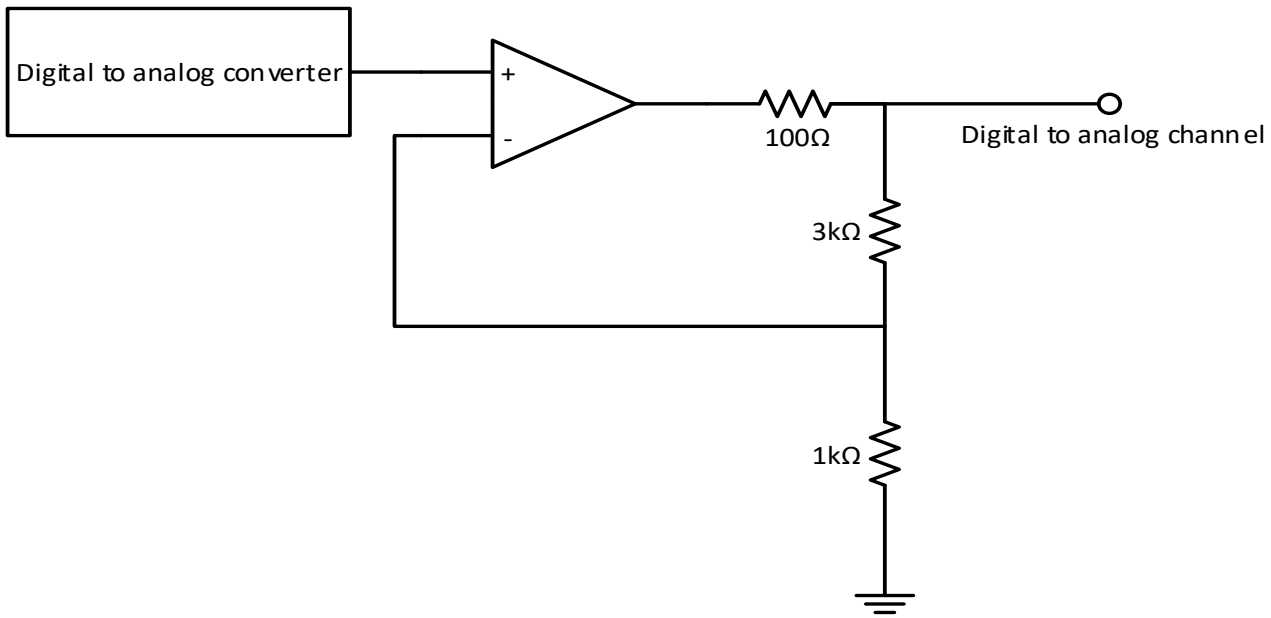

Figure 3-15: Simplified output circuit from digital to analog converter on dSPACE kit

i. Circuit analysis

This circuit was analysed in a similar manner to an ideal non-inverting op-amp configuration. In this analysis, since there is negative feedback, we can safely assume that the inputs are always going to be at the same voltage. Therefore, the output voltage immediately after the op-amp itself is given by:

$$V_{out} = V_{DAC}\left(1 + \frac{3100}{1000}\right) \tag{30}$$

Assuming the input bias current to the op-amp is negligible, then the voltage at the terminals of the voltage at the channel can be calculated as a simple voltage divider ratio. The overall equation for the voltage at the DAC channel of the dSPACE kit is therefore:

$$V_{DAChannel\,x} = \frac{4000}{4100} \times V_{out} = V_{DAC} \times \left(1 + \frac{3100}{1000}\right) \times \frac{4000}{4100} = 4V_{DAC} \tag{31}$$

3.4.2 Output voltage range and requirements

The output voltage range for each DAC channel is -10V to 10V, which corresponds to an input setting of -1A to +1A respectively. The TTI LD300 load input requires a 0-4V input voltage for a full-scale deflection (0-80A or 0-8A depending on the range selected). This means that the output signal from the DAC should lie between 0-4V, hence the need for scaling. From the above information, we can easily determine the gain that needs to be applied to the current setting to obtain the correct value of current at the load. The overall gain of the system is given by:

$$G_{overall} = G_{DAC} \times G_{LOAD} \tag{32}$$

The load's gain G_{LOAD} in volts per amp is:

$$G_{Load} = \frac{4V}{8A}(for\ 8\ A\ range) = 0.5V/A \tag{33}$$

The DAC software registers a value of 1A as 10V on the DAC output and therefore the gain is:

$$G_{DAC} = \frac{1A}{10V} = 0.1A/V \tag{34}$$

Therefore, the overall gain would be:

$$G_{overall} = 0.5 \times 0.1 = 0.05 \tag{35}$$

This overall gain was applied to all the signals from that needed to be injected to the load.

3.4.3 Sinusoid generation

The sinusoids were generated in MATLAB Simulink according to the schematic in Figure 3-16 below. They were then fed to the input of the DAC converter which was also accessed in MATLAB. The figure below shows the fundamental block for sinusoidal generation. This block in particular is set to generate a frequency of 1Hz with an amplitude of 2A and no phase shift. The sinusoidal signal that is generated by the formula in the block is:

$$V_o = V_p \times \sin(2\pi f t) \tag{36}$$

where V_p is the amplitude of the sinusoid and f is the frequency. This signal is then multiplied by the previous calculated gain of 0.05 to ensure the output is in the required range of the TTI LD300 load.

During the BIS, these blocks were connected in parallel and the corresponding output voltage added.

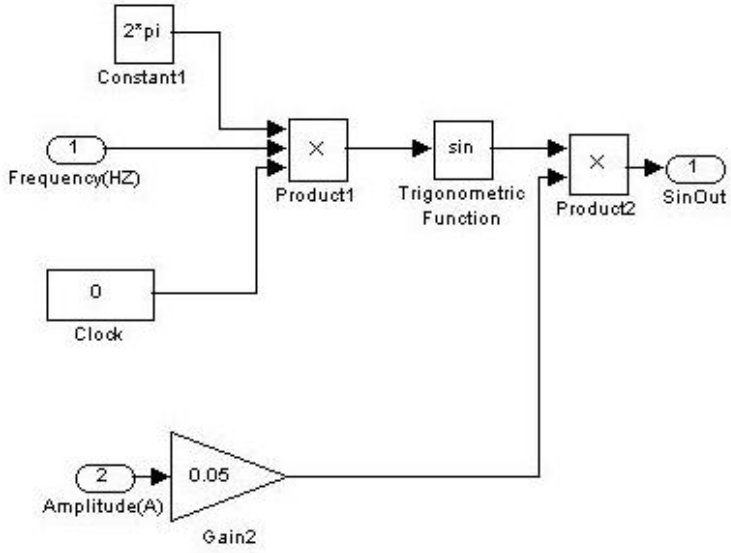

Figure 3-16: Functional sinusoidal generation Simulink block diagram

3.5 Data Acquisition

The data acquisition device chosen was the National Instruments NI USB 6366 shown in Figure 3-17. The NI USB 6366 has eight analog input channels which can be configured to a floating source or grounded source combination. In the experiments, all the inputs were configured to a grounded source i.e. the input signals were referenced to ground before input to the physical BNC pin. This was chosen over the floating source combination, which places the input to be in parallel with an effective resistance of $100G\Omega$ (input) and a 10pF capacitance as the voltages into the device were already referenced to ground. The figure below shows the NI USB connected with two BNC connectors to AI0 and AI1 with the two channels set to grounded source mode.

Figure 3-17: NI USB 6366 data acquisition device

3.5.1 Resolution

The ADC has a sixteen-bit resolution with input ranges of +/-10V, +/-5V, +/-2V and +/-1V. This sixteen-bit resolution is applicable to all ranges i.e. for the +/-10V range, the resolution would be $\frac{10-(-10)}{2^{16}} = 0.30mV$ whereas at the +/-5V the resolution would be $\frac{5-(-5)}{2^{16}} = 0.15mV$.

The cells have been tested by the manufacturer to have an impedance of less than $3m\Omega$ at 1kHz. This implies that the voltage rms magnitude with a 1A current peak to peak excitation at 1kHz would be:

$$V(rms) = \frac{1}{\sqrt{2}} \times 3 \times 10^{-3} = 2mV$$
$$\therefore V(peak\ to\ peak) = 2mV \times \sqrt{2} = 2.828mV \quad (37)$$

Implying that at a frequency of 1kHz for a 1A excitation signal, the peak to peak range of the voltage signal received at the Analog input of the device would be in steps of $\frac{2.828}{0.15}$ ~19 steps.

3.5.2 Sampling rate

The maximum sampling rate for the NI USB 6366 is 2MS/s (2MHz) per channel. The timing accuracy is 50ppm of the sample rate. The timing resolution is 10ns.

This therefore means that if sampling at 2MS/s which is the maximum sampling frequency given by the ADC, you can expect between 2000,100 and 1999,900 samples for every second. For comparison purposes if the ADC oscillator was to be used to build a clock, if the clock requires a sampling frequency of 1S/second, then the error after a year (~31,536,000 seconds) would be equal to twenty-six minutes!

The Nyquist theorem states that the sampling frequency should be at least twice the signal frequency you're measuring, however in the experiments performed throughout this thesis, the minimum sampling frequency used was ten times the sampling frequency.

3.5.3 Data transfer and input FIFO size

The NI USB 6366 has a 64MS (mega sample) FIFO size, for a recording it can store 64 million samples before it must transfer them via the USB connection to the host PC. Because the ratio of sampling frequency to measured frequency is a 10:1 in the experiments, the FIFO alone would be able to hold (64 million/10) = 6.4 million cycles before an overflow condition would occur and the data would have to be transferred to the host PC. For a typical EIS experiment the number of cycles recorded for each particular frequency is not more than five.

In the BIS experiments which are done in seconds, the maximum sampling frequency is 100kHz for a 10kHz sinusoid. This same sampling frequency is to be sustained for a period of three cycles of the lowest frequency which can be as low as 10mHz. This equates to sampling at 100kHz for three hundred seconds i.e. 30MS. This is still less than the input FIFO size of 64MS.

Data transfer is done using the USB cable and depends on the host PC capability however it supports data transfer speeds of up to 32 MB/s.

3.5.4 Differential non-linearity

The error in quantisation also known as the differential non-linearity for the NI USB 6366 analog input is stated as +/- 1 LSB which means that for the ADC being used in the +/-5V input range as per the experiments, the magnitude of the quantised voltage is $\frac{5-(-5)}{2^{16}} = 0.15mV$ and thus the error is +/- 0.15mV.

3.5.5 Calibration

The NI USB 6366 supports two kinds of calibration. Internal calibration and external calibration.

i. *Internal Calibration*

This calibration is usually performed using a software command and requires no external connection. This calibration is usually performed to help account for environmental conditions such as operating temperature that might have changed from the last external calibration. The temperature drift from the last internal calibration is usually smaller than the temperature drift from the last external calibration.

ii. *External Calibration*

The calibration is usually performed at the NI centre. This calibration is usually performed with a high precision calibrator and replaces previous external constants contained within the EPROM of the NI USB device. NI recommends external calibration be done on a two-year basis.

There is a software calibration wizard in Lab View that helps to quickly calibrate each analog input channel (See Figure 3-18 below). The calibration wizard requires that a suitable reference voltage is present and connected and that the device has been warmed up. Once the calibrator has been set up, the reference voltage is connected to the input channel and the corresponding output voltage is adjusted to correct for any errors that may have resulted since the last calibration, such as temperature drift etc.

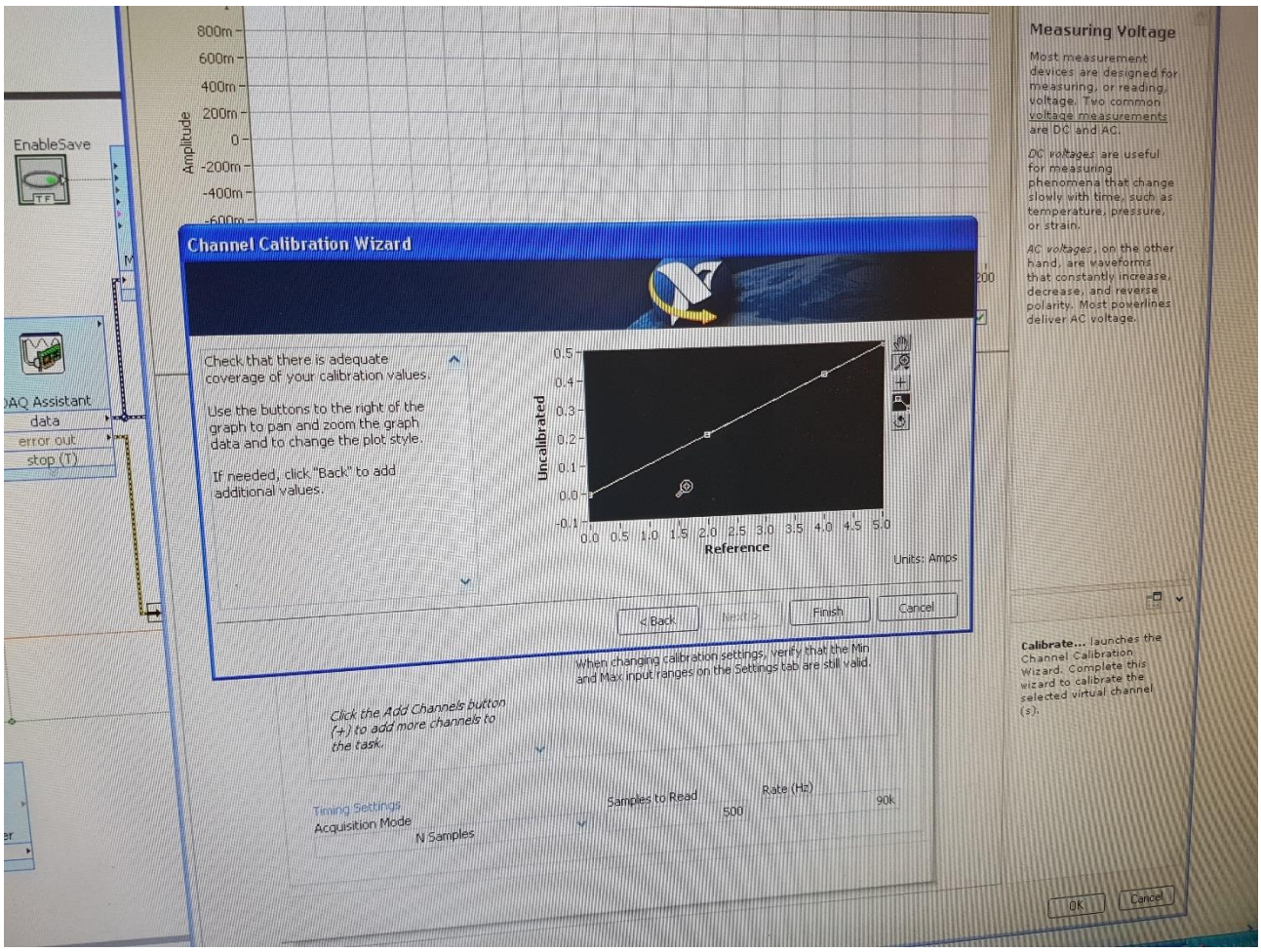

Figure 3-18: Channel calibration wizard

iii. ***Voltage and current scaling***

When the calibration is completed, the voltage and current can be scaled according to the values that are required by the output. For the EIS and BIS experiments, the voltage from the source was in the +/- 5V range as the Li-ion cell is never charged to above 4.3V. This meant that the voltage scaling could be a 1:1 between the input and voltage and the recorded voltage. The voltage scaling equation is therefore given by the following equation:

$$V_{cell} = V_{AIO} \tag{38}$$

where V_{AIO} is the voltage at the analog input channel measuring the voltage.

From the previous chapter we calculated the gain from the signal injection device needed to be 0.05 for the input signal to be in the required 0-4V range required by the TTI LD300 load. To get the correct current reading from the NI DAQ, the effect of this gain would have to be

reversed. This therefore means that the current scaling on the current channel would have to be 1/0.05 = 20A/V. The current channel is scaled to give a current corresponding to the following equation:

$$I_{cell} = \frac{V_{AI1}}{0.05} = 20V_{AI1} \tag{39}$$

where V_{AI1} is the voltage at the analog input channel measuring the current.

3.5.6 Absolute accuracy

The analog input absolute accuracy table is as follows for the ADC.

Nominal Range		Residual Gain Error (ppm of Reading)	Gain Tempco (ppm/°C)	Reference Tempco (ppm/°C)	Residual Offset Error (ppm of Range)	Offset Tempco (ppm of Range/°C)	INL Error (ppm of Range)	Random Noise, σ (μV rms)	Absolute Accuracy at Full Scale* (μV)
Positive Full Scale	Negative Full Scale								
10	–10	95	8	5	15	35	46	252	2498
5	–5	102	8	5	15	36	46	134	1289
2	–2	102	8	5	15	42	46	71	528
1	–1	120	8	5	15	50	46	61	291

Figure 3-19: Table showing the absolute accuracy at full scale in microvolts for the analog input calculated for 10000 samples, T_{LI} = 1 degree Celsius and T_{LE} = 10 degrees Celsius [54].

The absolute accuracy A_A is obtained as the sum of the gain errors, offset errors and the noise uncertainty for that particular voltage range i.e.:

$$A_A = (V_r \times G_E) + (V_r \times O_E) + N_U \tag{40}$$

where Vr, is the voltage range, G_E is the gain error, O_E is the offset error and N_U is the noise uncertainty.

The gain error in parts per million is calculated by the formula:

$$G_E = R_{GE} + G_{TMPCO} \times T_{LI} + R_{TMPCO} \times T_{LE} \tag{41}$$

where R_{GE} is the residual analog input gain error, G_{TMPCO} is the gain temperature coefficient, T_{LI} is the temperature change from last internal calibration, R_{TMPCO} is the reference temperature coefficient and T_{LE} is the temperature change from the last external calibration.

The offset error in parts per million is calculated by the formula:

$$O_E = R_{OE} + O_{TMPCO} \times T_{LI} + I_{NLE} \tag{42}$$

where R_{OE} is the residual offset error, O_{TMPCO} is the offset temperature coefficient, and I_{NLE} is the integral nonlinear error [54].

The noise uncertainty N_U is given by the formula:

$$N_U = \frac{3\sigma}{\sqrt{N}} \tag{43}$$

where N is the number of samples and 3 is the coverage factor [54].

From the above formula, the assumptions made are that the device is operating within $10°C$ of the last external calibration and therefore T_{LE} of $10°C$ is a valid assumption. The second assumption is that the readings are taken within 1°C of the last internal calibration. The final assumption is that the noise is normally distributed and falls within three standard deviations of its average value. Using this information, we can therefore calculate the absolute accuracy values for the +/-5V range channels used in EIS and BIS experiments.

During EIS measurements, the longest measurement period is three five cycle intervals. With ten samples per cycle (10:1 sampling ratio), this comes to $10 \times 5 \times 3 = 150\ samples$. For the input voltage range of +/-5V used, we can calculate the factors:

$$\begin{gathered} G_E = 102 + (8 \times 1) + (5 \times 10) = 160ppm \\ O_E = 15 + (36 \times 1) + 46 = 97ppm \\ N_U = \frac{3 \times 134}{\sqrt{150}} = 32.82\mu V \\ A_A(EIS) = 5 \times 160 + 5 \times 97 + 32.82 = 1317.82\mu V \end{gathered} \tag{44}$$

For BIS measurements, the readings are recorded for up to three periods of the lowest frequency (0.01Hz) which comes to a time interval of three hundred seconds. The sampling frequency is usually 100kHz and therefore the number of samples in a three hundred second

time interval are 30,000,000. The factors G_E , O_E are found to be the same as in the EIS measurements. The only changing factor is the noise uncertainty which in this case equates to:

$$N_U = \frac{3 \times 134}{\sqrt{30 \times 10^6}} = 0.073\mu V \tag{45}$$

thus, the absolute accuracy associated with the BIS measurements used in this thesis is:

$$A_A(BIS) = 5 \times 160 + 5 \times 97 + 0.073 = 1285.073\mu V \tag{46}$$

i. Noise uncertainty variation with sample size for experiments

The relationship between the noise uncertainty and the number of samples chosen for the recording is shown in Figure 3-20 below. It clearly shows that the higher the number of samples, the less the magnitude of the uncertainty.

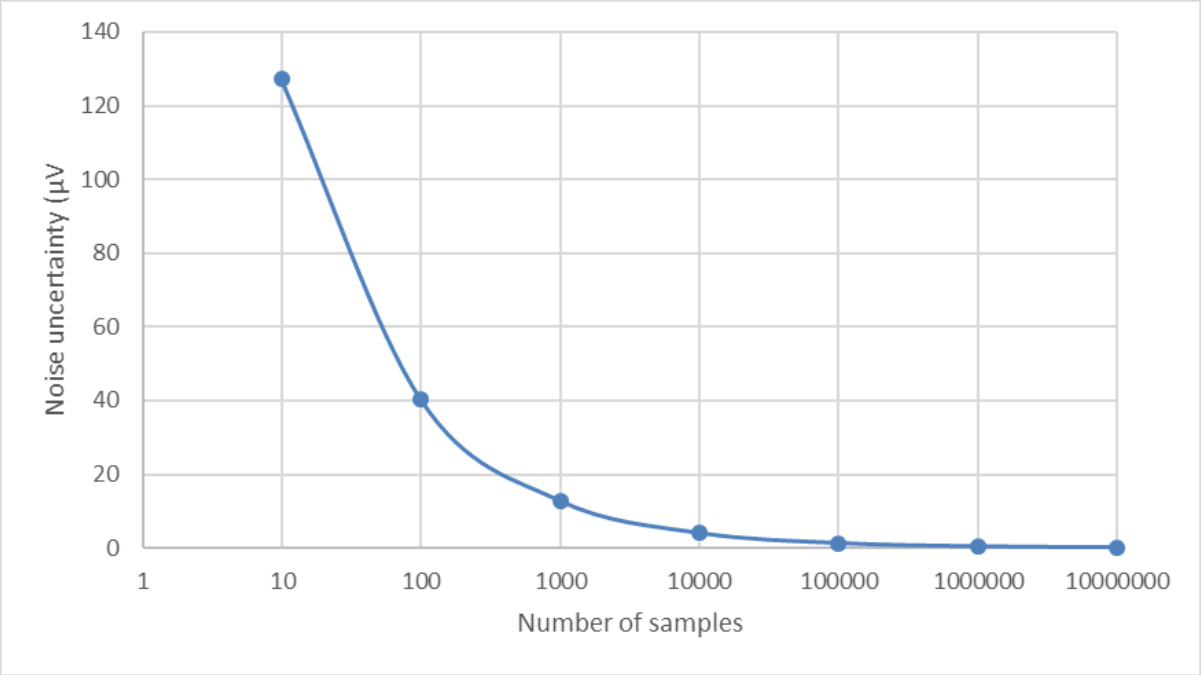

Figure 3-20: Noise uncertainty variation with number of samples

3.6 Load

The EIS and BIS experiments were implemented using the TTI LD300 DC electronic load shown in Figure 3-21 with and external voltage and current control. The TTI LD300 specifications are

mentioned below. The TTI LD300 load was found to be capable of operating within the 0.1hz - 10kHz range that is typically required of EIS experiments.

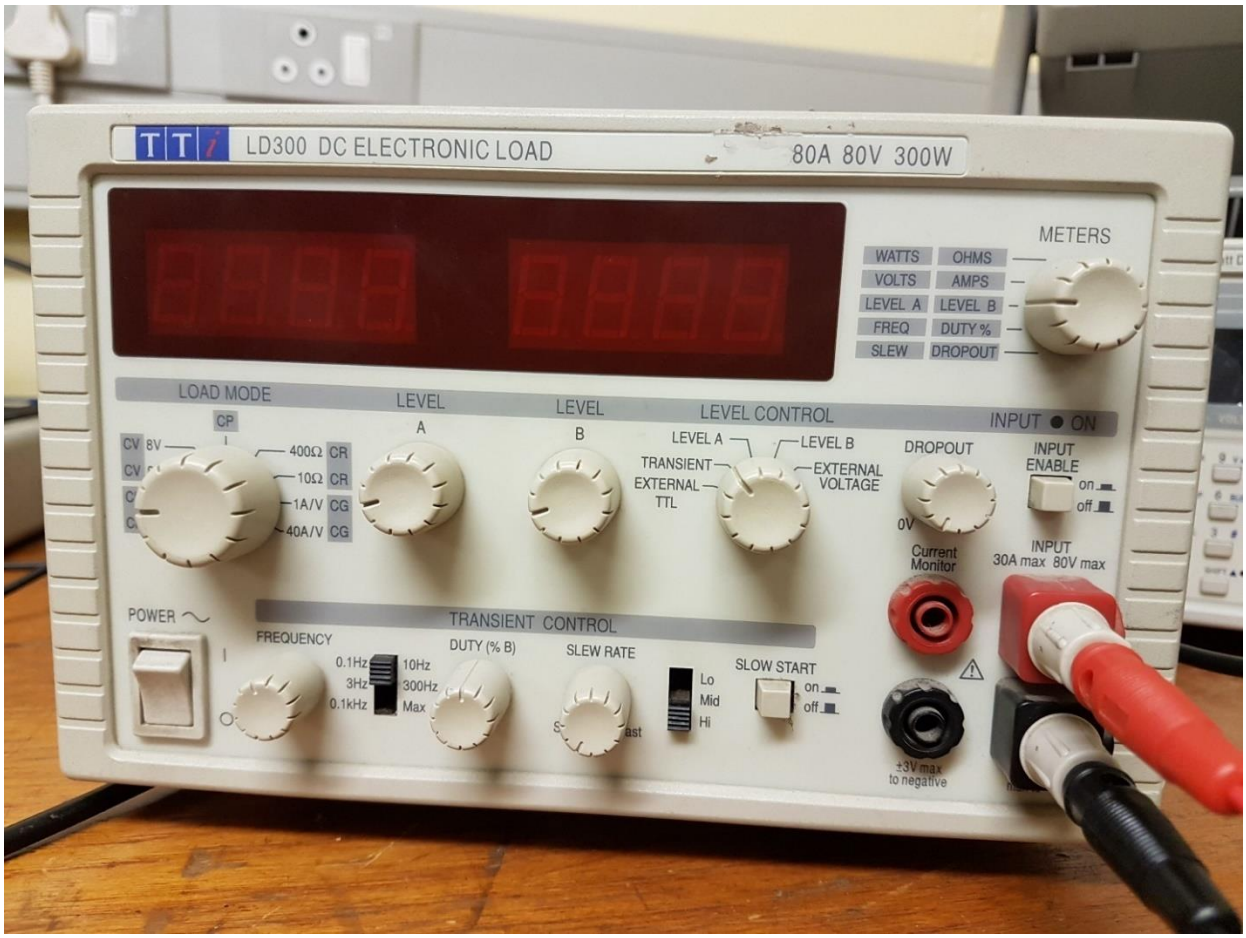

Figure 3-21: LD300 DC Electronic load used as the current driver for the EIS and BIS experiments

3.6.1 Modes of operation

The TTI LD300 offers five modes of operation. A constant current mode, a constant voltage mode, a constant resistance mode, a constant conductance mode and a constant power mode. There is also a remote-control mode in which the level of any of the above operating modes can be set externally. The input voltage range required for a full-scale level setting was 0-4V at the input.

Because the experiments were to be done in galvanostatic mode, the constant current mode was selected and an external control voltage was used to vary the current. The internal voltage sensor was used as the current monitor. The internal voltage sensor gave a voltage reading corresponding to 50mV/Amp. The figure below shows the connections to the analogue input terminal for the load. The constant current mode is implemented with the help of two parallel

FETs with each stage in a local current feedback loop to ensure equal power sharing. Figure 3-22 shows the current monitor connection and analogue control voltage connection to the load.

Figure 3-22: Current monitor connection and analogue control voltage connection to the load

3.6.2 Minimum operating voltage

The LD300 load can draw a constant current of up to 10A for an input voltage of 500mV. With an input voltage of 2V the load can maintain a current of 80A. This capability demonstrated that the load can operate within the voltage of a standard Li-ion cell (3.7V) with currents of up to 10A that were used in the experiments. Current measurement accuracy and resolution.

The LD300 load meter resolution for the current measurement was specified to be 1mA on an 8A range. This implied that for any current measurement, a 1mA adjustment would have to be factored in. The accuracy in setting the level for the load is specified to be $+/-(0.2\% + 20mA)$. Signifying that for a constant current of 1A, the value according to the formula will range between 1.022A and 0.978A.

3.6.3 Over discharge protection

Because the load can draw a constant current of up to 10A for an input voltage of 0.5V, the need for an over discharge protection mechanism was important, to prevent the cell from over discharging to voltage levels below 3V. The TTI LD300 comes with an adjustable voltage drop out. This drop out was set to 3.0V. If the voltage at the input of the load fell to below 3.0V, the load current was then reduced to zero.

In the case that there is a significant resistance between the source and the voltage sense part of the load, then as the current drops, the series resistance would drop, making the voltage at the terminal of the load to be bigger, resulting in instability. This effect is minimized by placing the load as close as possible to the source (the battery).

3.6.4 Slew rate adjustment

At high frequencies, the load was required to respond to changes in the external control voltage frequency and adjust the current accordingly with minimal distortion on the wave form. The slew rate is adjustable from the terminal. The slew rate for the LD300 can be adjusted from 8mA/ms to 2500A/ms.

Consider the triangular wave in Figure 3-23 below. If the LD300 load is required to give a current with such a profile without clipping, the minimum slew rate setting can be worked out as below.

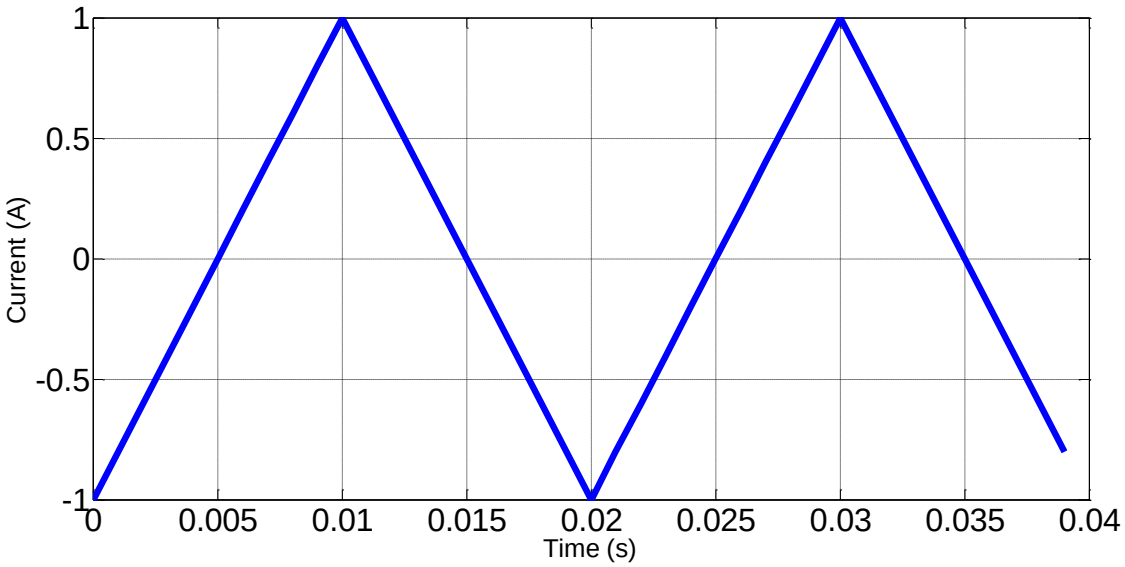

Figure 3-23: Triangular wave for slew rate calibration.

It is observed in the above graph that the current changes from +1A to -1A in 0.01 seconds. The maximum slope is 200A/s. Therefore, the minimum slew rate setting for the LD300 load to reproduce the triangular waveform without clipping is $\frac{1-^{-}1}{0.01\times10\text{^}3} = 0.2A/ms$ or 200mA/ms.

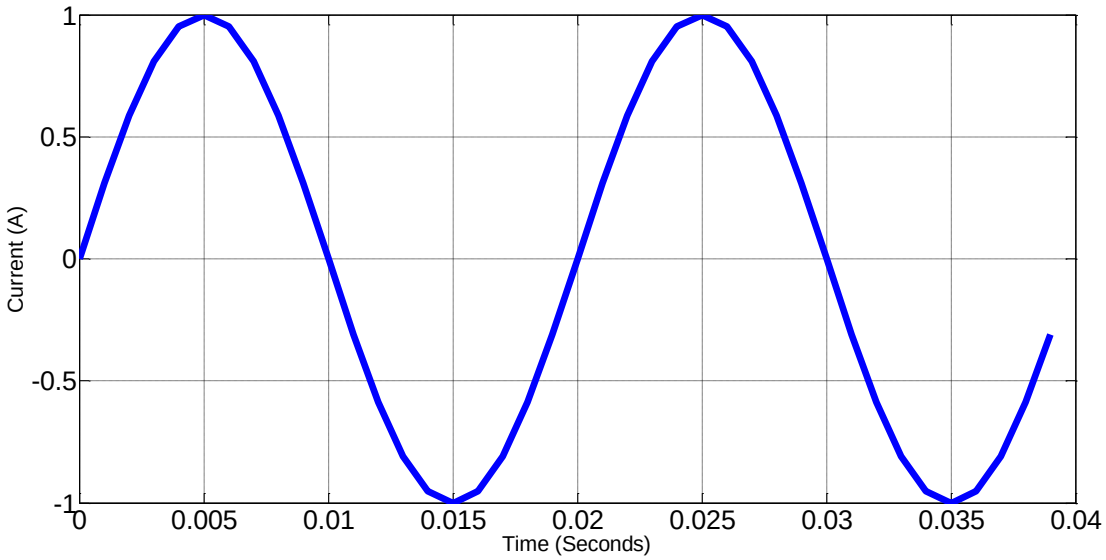

Figure 3-24: Sinusoidal wave for slew rate calibration

For the sinusoidal wave in Figure 3-24 above, the minimum slew rate setting required on the LD300 was calculated as follows:

The load would be required to adjust fast enough at points where the sinusoidal signal change is maximum. For the sinusoidal wave above, the steepest point is obtained when $t = n \times \frac{T}{2}$ were: T is the period, and n is an integer number 0, 1,2 … For simplification, we can assume $n = 0$.

We can then simplify this for any arbitrary sinusoid of amplitude A and frequency f. If the sinusoid is given by $A \times \sin(2\pi f t)$, then it can be shown the equation for the magnitude of the slope of the wave form when its gradient is at its peak is given by $S = 2\pi f \times A$.

The slope for this graph at these instants is $s = 2 \times \pi \times (0.02)$= 314A/s.

The minimum slew rate therefore would have to be 0.314A/ms to produce the above current profile without distortion; fifty seven percent higher than the minimum slew rate required for the same amplitude and frequency triangular wave.

The maximum peak current used in the experiment is 1A, and therefore at the 2500A/ms setting, the maximum frequency that could be obtained for a sinusoidal signal without slew distortion would be $f = \frac{S}{2\pi A} = \frac{2500 \times 10^3}{2\pi(1)} = 398.9khz$, which is above the required 0.01 -10khz for EIS experiments. For all experiments, the slew rate was adjusted to 2500A/ms.

The graph in Figure 3-25 below has been generated to show the relationship between the slew rate setting, the peak to peak amplitude of the excitation signal and the maximum frequency the load can support.

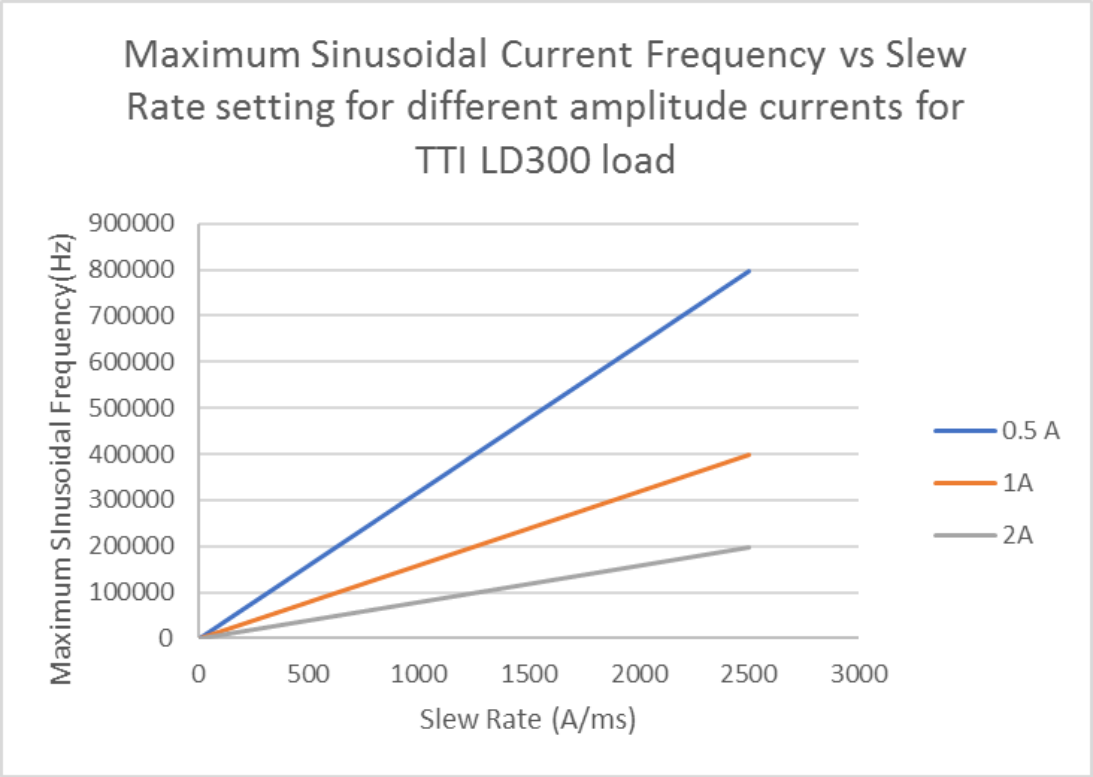

Figure 3-25: Maximum frequency for each peak to peak current for a particular slew rate setting

3.6.5 External voltage control

In the external voltage control mode, the current level is set to be linearly proportional to the voltage at the remote-control input on the back panel of the load. This is how the voltage is set for the load. The control voltage terminal has an input impedance of $400k\Omega$ to the negative load terminal.

3.7 Grounding and shielding

Grounding and shielding of the cables was needed to minimise the noise and inductive effects of the signals. During experimentation, there were different ground signals, each separated from each other to minimize the effect of noise and coupling in the sampled signals to the ADC.

3.7.1 Types of ground signals in the experiments

There are two main ground signals that were encountered. The signal ground(reference) and the power supply ground.

i. Signal ground

These were the ground reference signals that were coming from the battery from the voltage and current measurement signals. Each of these were kept separate from the other and none of them were mixed. When connected to the ADC, the grounded source signal setting was applied to them, to ensure the ground selected was not that of the ADC power supply which could have interference. The NI USB 6366 has the capability of choosing which ground reference signal should be used. By moving the slider, one can switch from a free source (which means the ADC power supply will be the ground reference) and the grounded source mode (where the signal reference will be the ground reference for that signal). Furthermore, the cabling of the signal input line was twisted pair cabling. Figure 3-26 shows the grounded source setting of the NI USB 6366 device analog input channels.

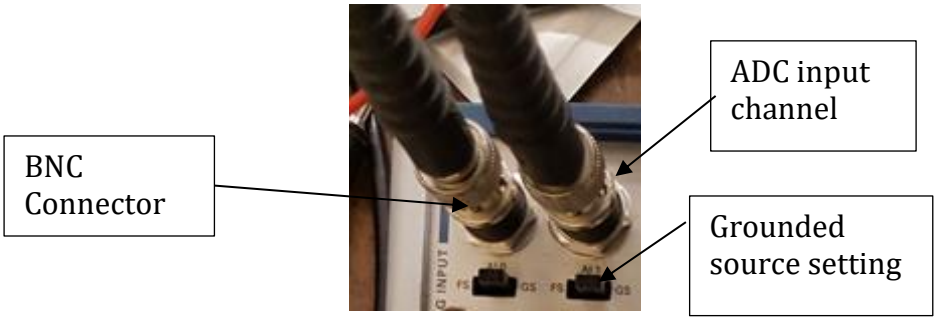

Figure 3-26: Grounding and connection of input signals

ii. Power supply grounds

The power supply grounds are all connected by sharing the same ring main circuit. Care was noted to ensure they were kept separate from the signal grounds.

3.7.2 Shielding and cabling

The connectors used at the signal inputs were BNC connectors. The cables to the connectors were shielded over a twisted pair. These cables were chosen to minimize inductive effects noise as well as coupling.

4. SOC Measurement and Impedance Spectroscopy Implementation

4.1 State of Charge Measurement

When determining the state of charge, a combination of the open circuit voltage to determine the initial state of charge, and then coulomb counting was implemented. This was addressed in section 2.5.2.

4.1.1 Initial state of charge estimation

The main difficulty when determining the state of charge by coulomb counting is the estimation of the initial state of charge. A simple method for determining the initial state of charge is creating a look up table for each of the open circuit voltages from end of discharge (approximately 3.3V) to end of charge (4.2V). Towards the end of charge voltage and end of discharge voltage, the terminal voltage of the cell rises and falls rapidly, enabling the observer to estimate the state of charge easily. Away from these voltages, the voltage profile of the terminal voltage vs state of charge is relatively flat and therefore it is difficult to place a value on what the initial state of charge is, as the voltage does not rise or fall significantly for relatively large state of charge changes.

The look up table for the initial state of charge was implemented with MATLAB Simulink. The terminal voltage from the cell was fed into the ADC channel of the dSPACE module.

The function that converted the read open circuit voltage was:

$$Init_{SOC} = f(V_T) \tag{47}$$

where V_t is the terminal voltage of the cell and $f(V_t)$ is the nonlinear relationship between the SOC and the terminal voltage implemented as a simple look up table.

4.1.2 Integration time constant calculation

From equation (6), if the assumption is made that the loss current is negligible and the current flowing is 0.5C = 10A, then we can assume that the constant current $(I_{batt} - I_{loss}) \approx I_{batt} =$

$10A$. The capacity of the cell is 20Ah and therefore in Ampere seconds will equate to $20 \times 3600 = 72000As$. Equation (6) then becomes:

$$SOC_{final} = SOC_{initial} + \frac{10}{72000}\int_0^t d(t) = SOC_{initial} + \frac{1}{7200}\int_0^t d(t) \tag{48}$$

4.1.3 Laplace transformation

To implement the integration in MATLAB, the Laplace transform was applied to the integral and the result of the SOC constant current discharge test were plotted. The Laplace transform of a time integral is:

$$\mathcal{L}\left\{\int_0^t g(t)\right\} = \frac{G(s)}{s} \tag{49}$$

Therefore, the analog signal that represents the current is multiplied by 1/s in the block diagram in Figure 4-1 below.

4.1.4 State of charge measurement block diagram

The block diagram showing how the state of charge measurement was implemented is shown in Figure 4-1 below. DS1104ADC_C5, DS1104ADC_C6 and DS1104ADC_C7 are the inputs from the dSPACE kit analog to digital converter ports representing channel 5, 6 and channel 7 respectively.

DS1104ADC_C5 was used to measure the open circuit voltage before the charging/discharging took place to estimate the initial state of charge.

DS1104ADC_C6 was used to measure the current into the cell during the charging.

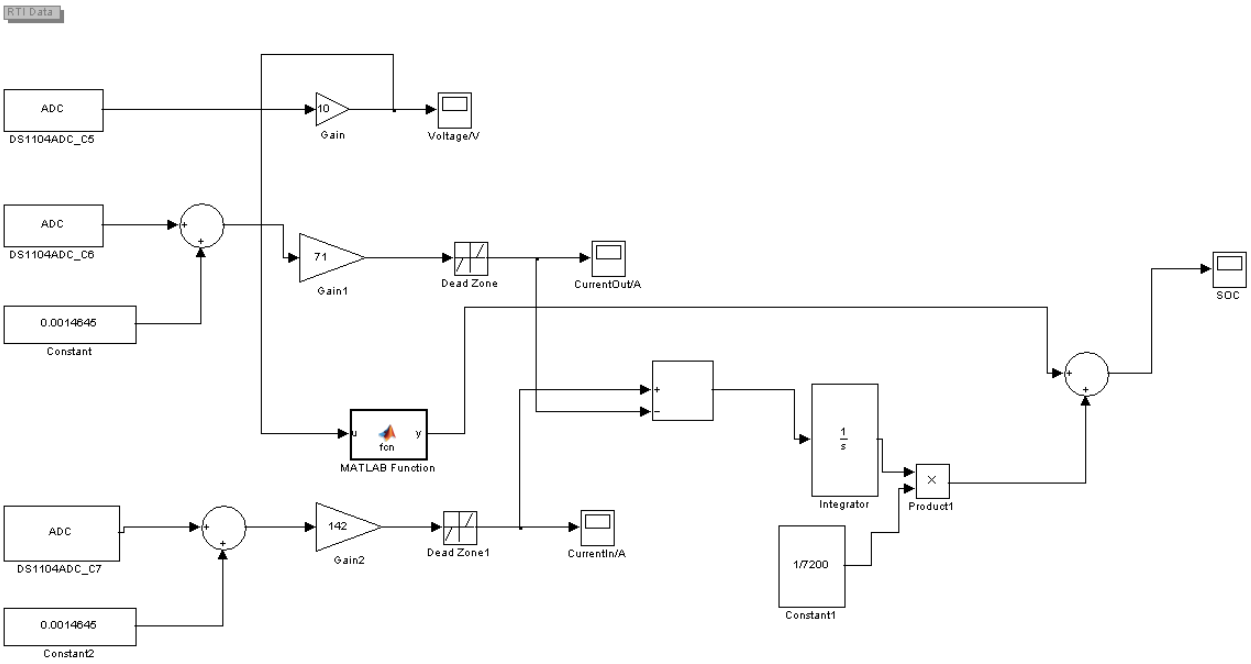

Figure 4-1: State of charge measurement block diagram

4.2 EIS Implementation

This section describes how EIS was implemented using the available hardware in the lab.

4.2.1 Hardware connections

The signal generator output was connected to the analog input port of the TTI LD300 via a standard BNC connector. The voltage out of the signal generator was calibrated to produce the required output current according to the TTI LD300 datasheet.

4.2.2 Cell conditioning

The cell was subjected to a constant current charging profile and thereafter a constant voltage profile as mentioned in previous chapters. The cell was charged with a constant current of 0.5C. From the step response data, shown in Figure 3-8 above, it was established the cell would take approximately one thousand three hundred seconds (twenty minutes) after a constant charge for the open circuit voltage to reach steady state. This rest period was then observed before the experiment was started.

4.2.3 Mode of operation

The EIS was carried out in galvanostatic mode. The current was used as the excitation signal and the corresponding output voltage was then measured at the terminals of the cell.

4.2.4 Frequency selection

The frequencies for testing were selected based on a logarithmic scale from 0.02hz to 2kHz which corresponds to about 4-5 points per decade. The frequency range was chosen based on earlier work done in [42], [55] in performing similar EIS measurements.

4.2.5 Sampling rate and cycle count

The sampling rate was chosen with the Nyquist sampling criterion in mind. i.e. the minimum sampling frequency was to be twice the measured frequency. The final sampling frequency depended upon the frequency to be tested. The higher the frequency to be tested, the higher the sampling frequency, as well as the number of cycles required from which to obtain the magnitude response. The factor of sample frequency to the measured frequency was kept at ten.

Table 4.1: Table of frequencies, cycles and sample rates used for EIS measurement

Frequency point	Frequency (Hz)	Cycle count	Sample Frequency (Hz)	Time (s)
f_0	0.020	3	2	150.0000
f_1	0.048	5	4.8	104.1667
f_2	0.158	5	15.8	31.6456
f_3	0.514	5	51.4	9.7276
f_4	0.690	5	69	7.2464
f_5	0.93	10	93	10.7722
f_6	1.25	10	125	8.0000
f_7	1.68	10	168	5.9689
f_8	5.46	10	546	1.8326
f_9	9.85	10	985	1.0155
f_{10}	17.77	10	1777	0.5627
f_{11}	32.07	20	3207	0.6236
f_{12}	57.89	20	5789	0.3455
f_{13}	104	20	10400	0.1914
f_{14}	189	40	18900	0.2122
f_{15}	340	40	34000	0.1176
f_{16}	614	40	61400	0.0651
f_{17}	1108	40	110800	0.0361
f_{18}	2000	40	200000	0.0200
			Total Measurement Time(s)	332.5495119
			2-minute recovery period(s)	2160
			Total Time Taken	**2492.549512 (forty minutes)**

4.2.6 Excitation amplitude

The amplitude of the excitation was adjusted at each measurement frequency so as not to impact the linearity of the EIS measurement, as well as to maximise signal to noise ratio as mentioned in [55]; i.e. the excitation amplitude was selected so as not to produce a voltage response of greater than 5mV at each individual frequency.

4.2.7 Charge profile between measurements

The charging profile between EIS experiments was a standard constant current - constant voltage profile like [56]. The current was kept to 4A during the constant current portion of the profile and left to drop to a minimum of 1 A in the constant voltage portion of the profile. The cell was then given a rest period of an hour after charging, before the EIS measurement could

be performed. Figure 4-2 below shows the current and terminal voltage of the cell during the charging period.

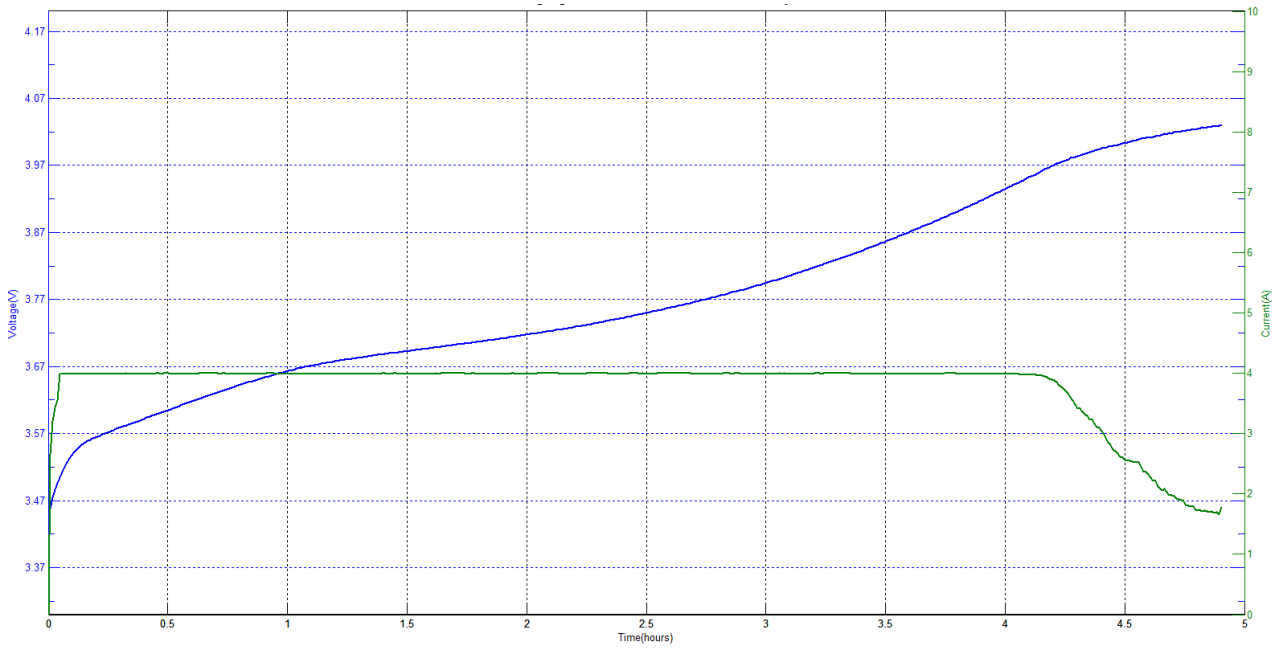

Figure 4-2: Charging profile of the cell indicating the change in the battery terminal voltage

4.2.8 FFT analysis

The Fast Fourier Transform was used to analyse the measured response signal. National Instruments recommends an application-based approach in the selection of window functions for FFT based analysis. See Figure 9-1 in the appendix for the NI recommendations. For EIS, since there is only one sinusoidal component being detected in the output, National Instruments recommends a flat top window[57]. The FFT Analysis was performed in NI's LabVIEW program. The block diagram is shown in Figure 9-3. The measured impedance and phase were then saved to a file and plotted, using MATLAB software.

4.2.9 EIS procedure

The flow diagram below describes the sequence in which the EIS experiments were performed. The cell was subjected to a constant charge and thereafter a constant voltage charge profile as shown in Figure 4-2. Afterwards, the cell was then left with no current being drawn for a period of about twenty minutes (as calculated in section 3.3.4) for its open circuit voltage to reach steady state. After this procedure, the cell's initial state of charge/open circuit voltage was

measured. The signals were injected one frequency at a time as shown in Table 4.1 above. The minimum number of cycles for which the signals were measured was three cycles, at the lowest frequency. At higher frequencies, more cycles had to be taken. This is because the longer the recording, the better the frequency resolution in the frequency domain of the FFT. The frequency resolution in the FFT is given by:

$$FFT_{frequency\ resolution} = \frac{f_s}{N} \tag{50}$$

where N is the number of samples and f_s is the sampling frequency. As can be seen from equation (50), the bigger the number of cycles, the more the sampling points and better the frequency resolution. It should also be noted that at lower frequencies i.e. below 1hz, the number of recording cycles was kept to a minimum for the state of charge of the cell to be maintained.

For each individual frequency test, the experiment was repeated three times as shown by the repetition counter. The data was then analysed using FFT analysis.

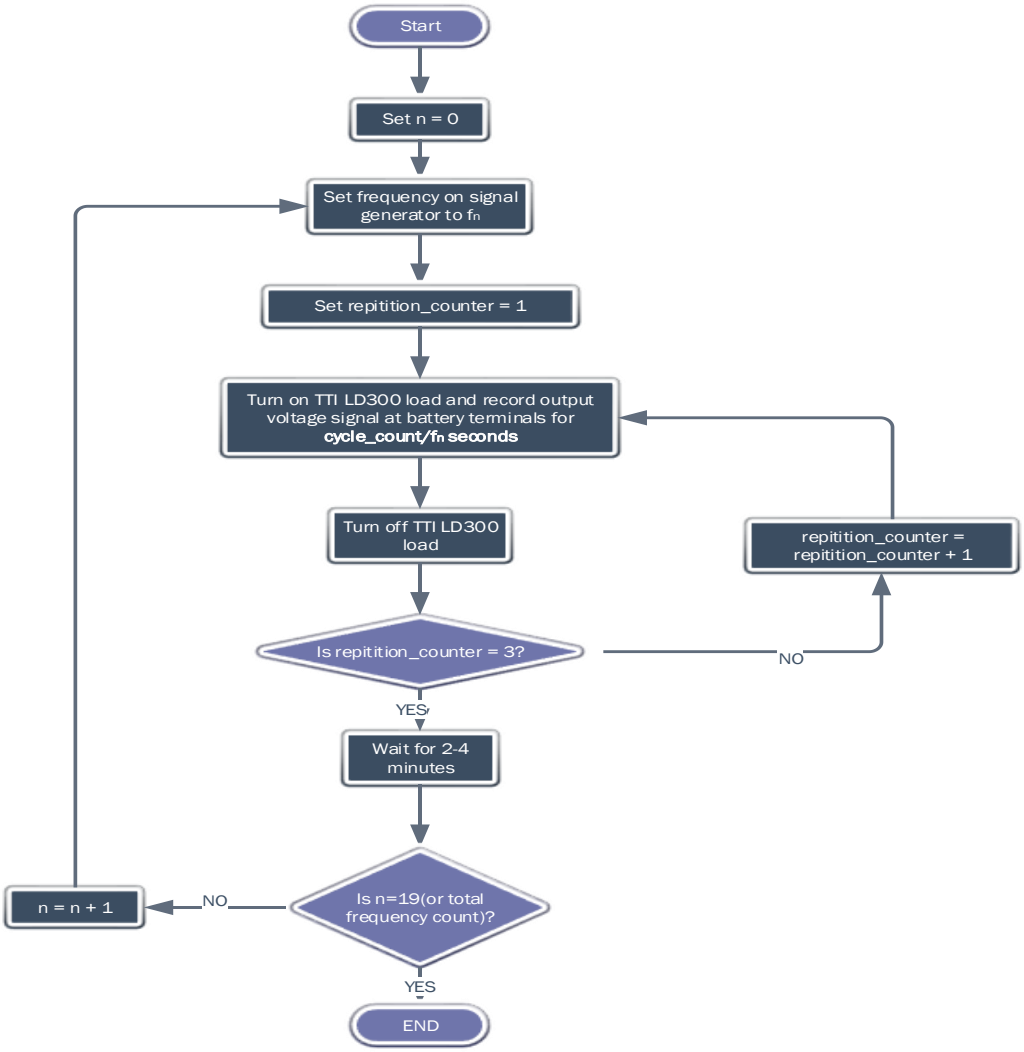

Figure 4-3. Flow chart showing the EIS procedure that was implemented on the test cells

4.3 BIS Implementation

This section explains how the multisine excitation was performed. It describes how the multisine signals were optimised and generated before injecting them into the cells. It also describes the signal extraction techniques used to extract the phase and magnitude components of the current excitation signals from the voltage response.

4.3.1 Magnitude optimization

To optimise the magnitude spectrum of the multisine to be injected, a full EIS was performed on the test cell. This was done to obtain the magnitude spectra of the impedance of the cell. This is shown in Figure 4-4.

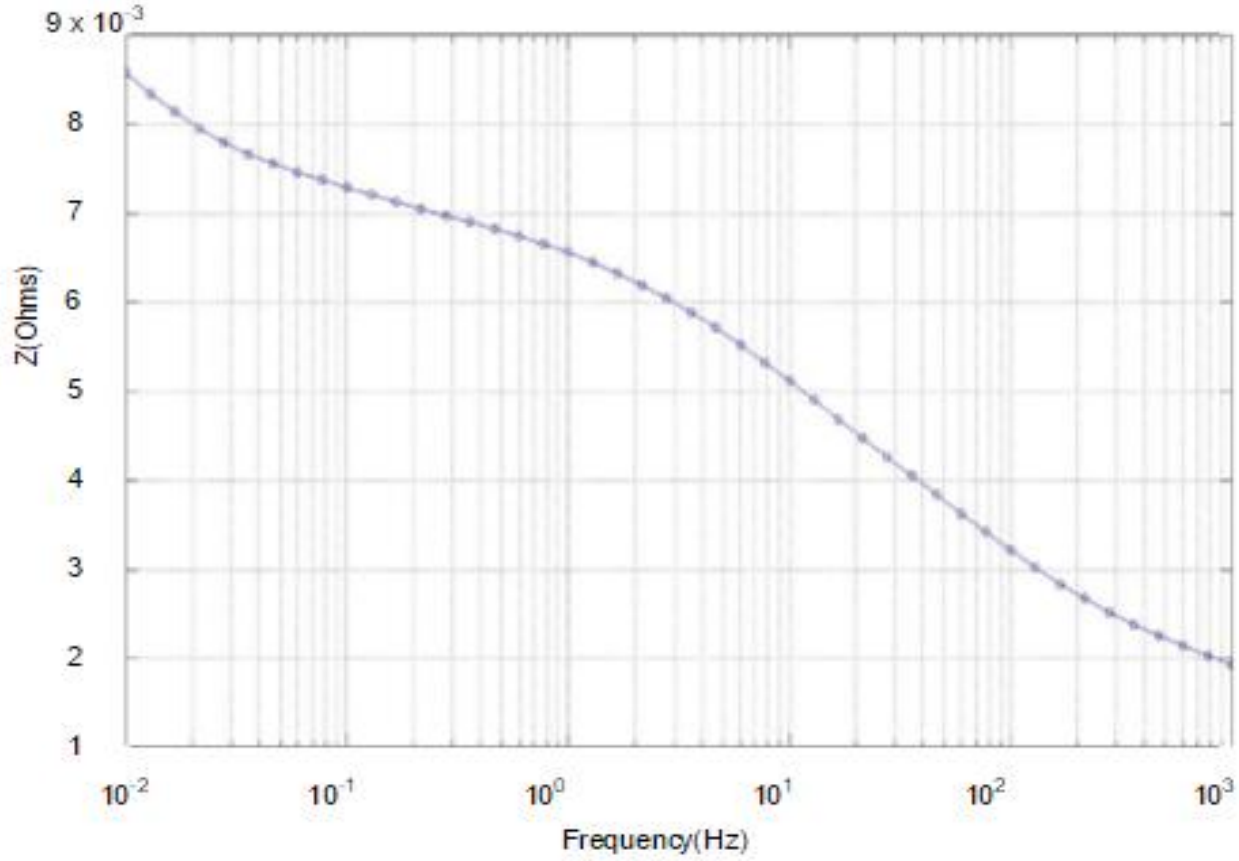

Figure 4-4: Magnitude spectra of the cell impedance

From the magnitude response, it was found that as the frequency increased, the magnitude of the cell's impedance reduced. From this observation, the magnitude spectrum for the multisine signal to be injected was chosen to be the inverse of the magnitude spectrum of the cell. This was done to ensure that the higher frequency regions of the cells with a low impedance are sufficiently excited to improve the output signal to noise ratio as suggested in [3] and [6]. This is shown in Figure 4-5. Secondly, the inverse magnitude spectrum ensures that in the low frequency regions, i.e. the high impedance sections, the magnitude of the output voltage response is less than 10mV, ensuring the cell is operating within its linear region[58].

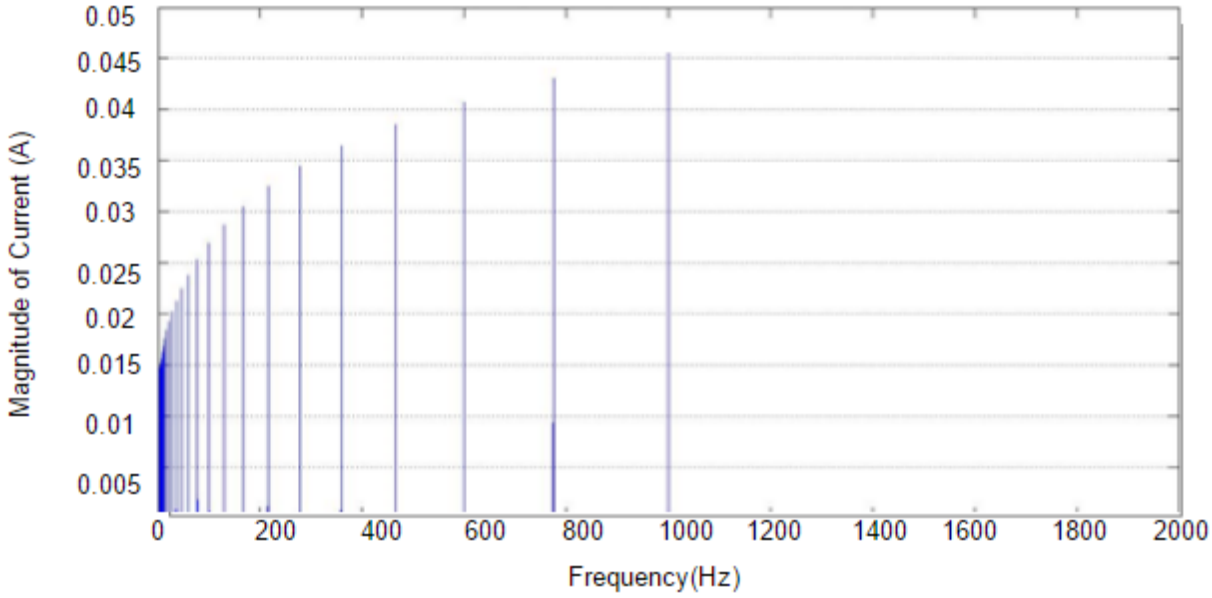

Figure 4-5: Magnitude spectrum of multisine signal

The time representation of the optimised magnitude spectrum of the multisine signal was then reconstructed and is shown in Figure 4-8. The peak value of the multisine signal for the same number of frequencies is much less than for the un-optimised signal in Figure 4-6.

4.3.2 Frequency optimization

The frequencies were selected to be a multiple of a power of two to the base frequency f_0. This is because the selection of frequencies in this manner removes the need for compensation and allows for measurement of the excitation signal within one period of the fundamental frequency [3].

$$f_n = f_0 \times 2^n \quad n = 0{:}\,N-1 \tag{51}$$

4.3.3 Phase optimization

As mentioned in 2.8.3, time optimization improves the crest factor of the multi-sine excitation signal. This then allows for more energy to be injected into the cell for a given range of frequencies. For the purposes of this study however, phase optimization was not applied to the signal. This was because results with the phase optimization did not yield a significant difference in the magnitude spectra from the ones with no phase optimization. This can be seen

with the Newman phase optimised signal in Figure 4-7 compared with the magnitude optimised, non-phase optimised signal in Figure 4-8. The phases for the Newman optimised signal were chosen according to equation (28).

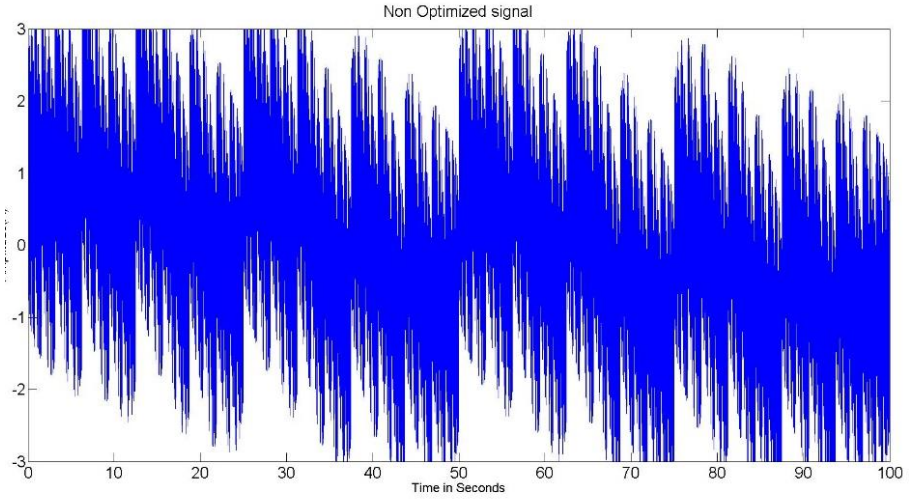

Figure 4-6: Non-optimised signal

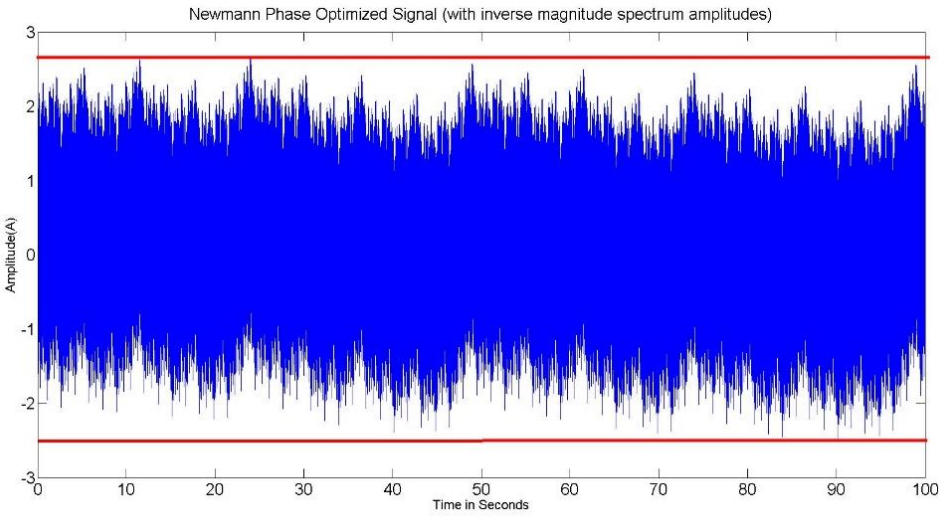

Figure 4-7: Newman phase optimised signal with inverse magnitude spectrum

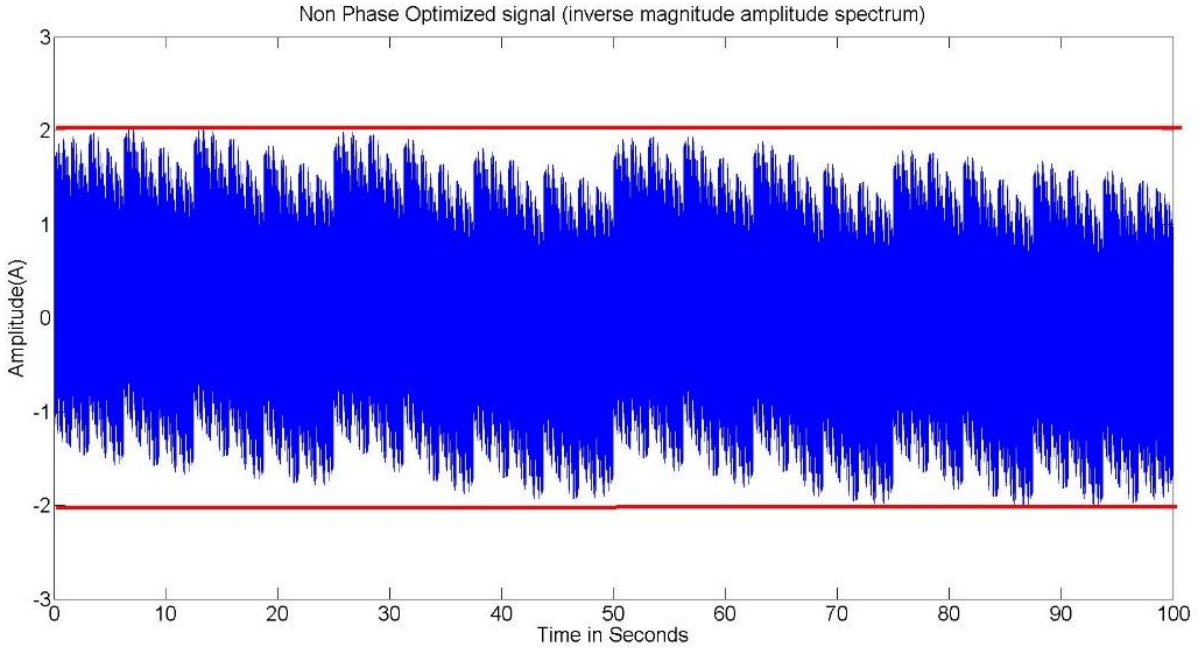

Figure 4-8: Magnitude optimised signal with no phase optimization

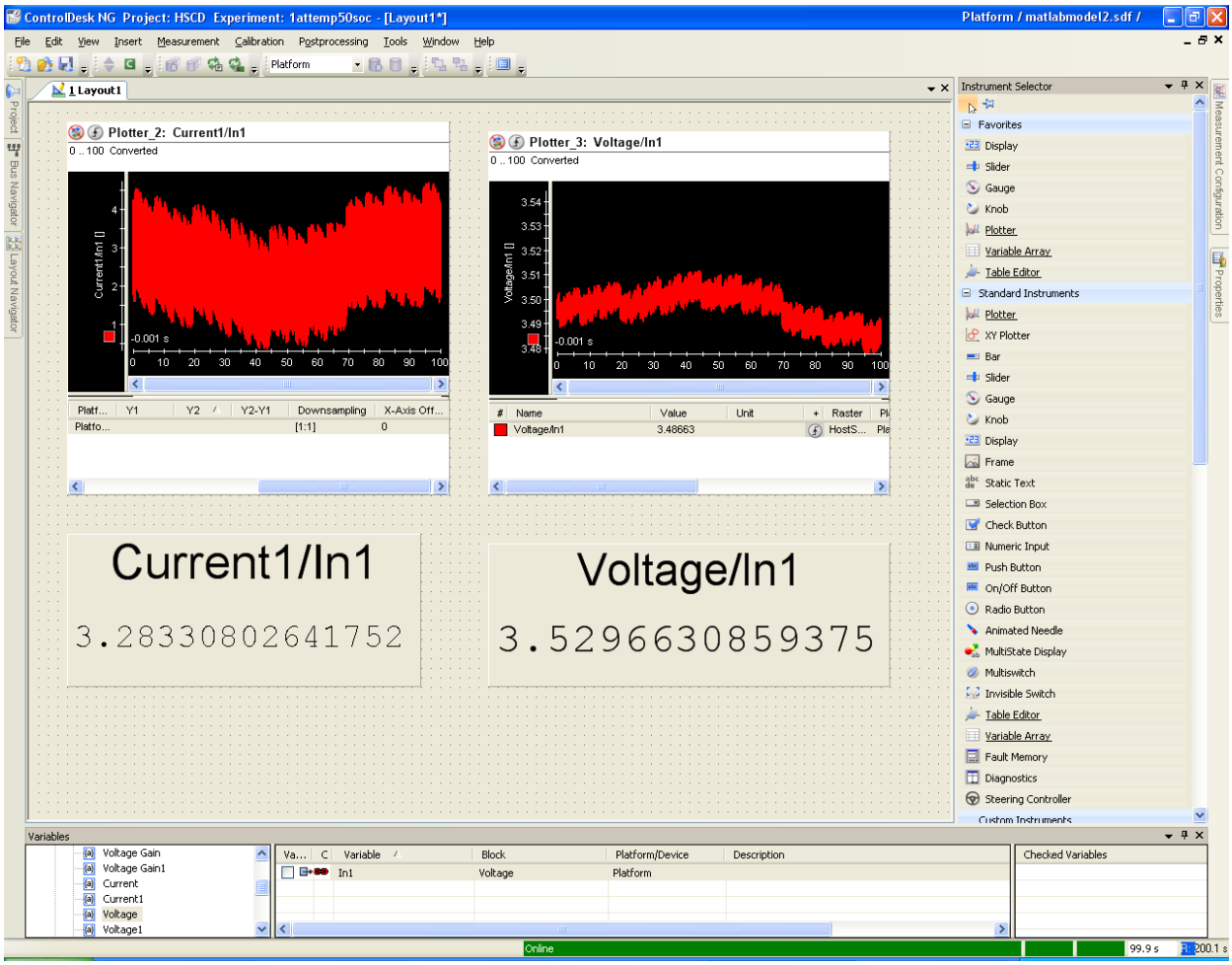

Figure 4-9: dSPACE snapshot of generated multisine together with the output voltage response

4.3.4 Hardware connections

The CLP1104 dSPACE DAC port was connected to the analog input of the TTI LD300 load. The DAC voltage was adjusted according to the TTI LD300 datasheet to generate the required current.

4.3.5 BIS/HCSD procedure

The BIS and HCSD procedure required the cell to be conditioned as discussed in section 4.2.2. After cell conditioning, the frequencies were selected to be a power of two harmonic as described in 4.3.2. After magnitude optimization, the frequencies were summed up and then injected into the cell with the help of the dSPACE module. The recordings lasted for two to three periods of the lowest frequency. The spectrum was analysed accordingly. Both FFT and synchronous detection techniques were used to analyse the output signal. The procedure is shown in the flow chart in Figure 4-10 below.

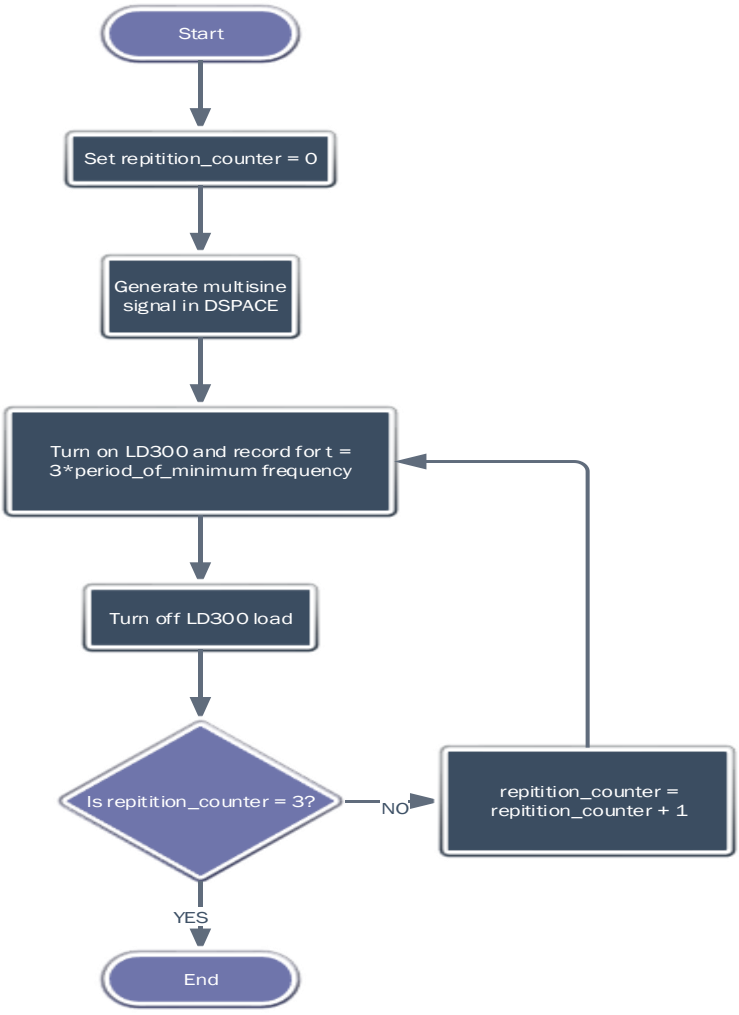

Figure 4-10: Flow diagram of the BIS/HCSD procedure

4.3.6 Multisine generation

The multisine generation was subdivided into three subsystems and implemented in MATLAB with the aid of Simulink as shown in Figure 4-11. The Simulink blocks for each of the subsystems can be found in the APPENDIX.

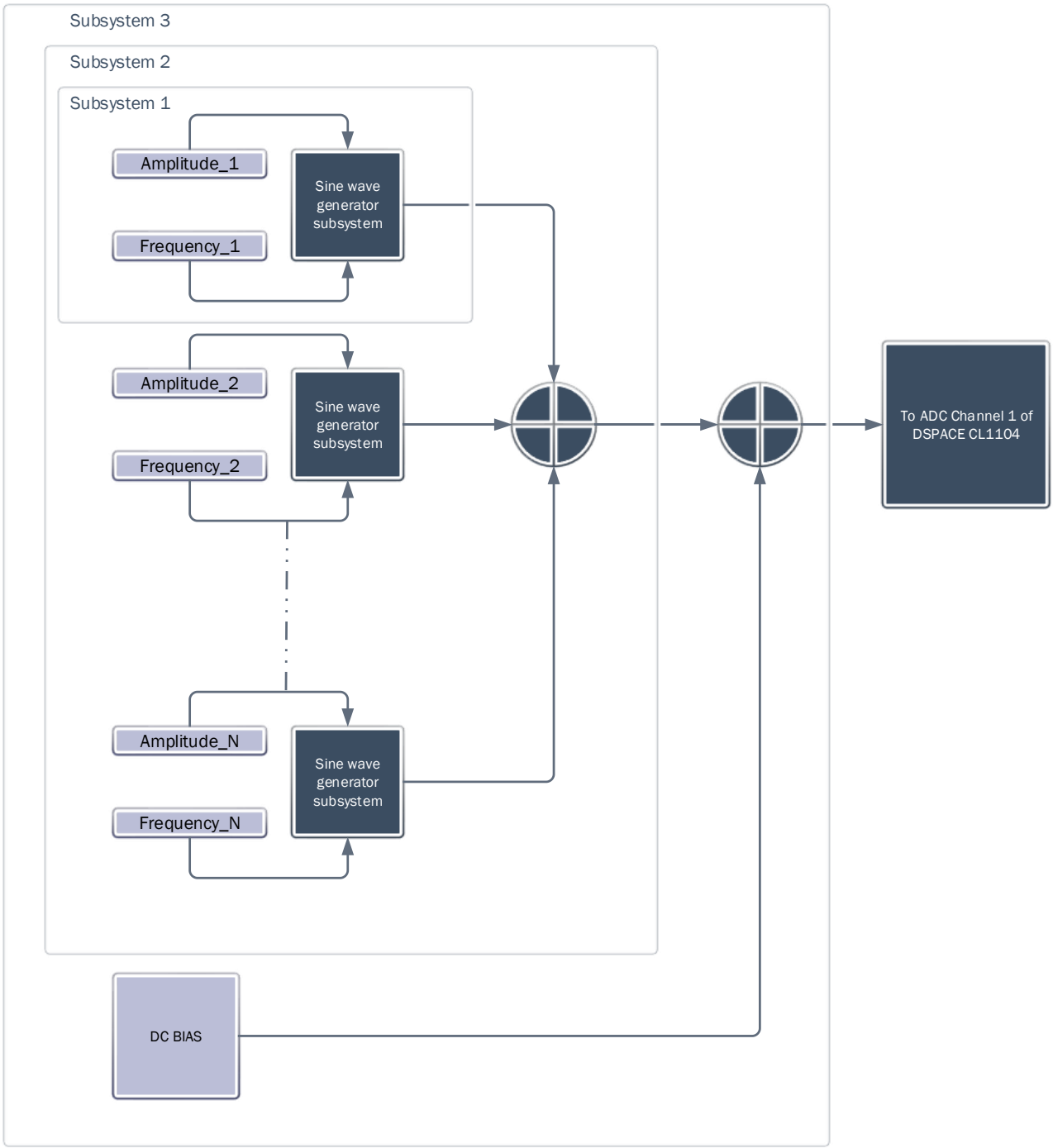

Figure 4-11: Block diagram showing how the multisine signals were generated

4.3.7 Duration of the broadband impedance measurement techniques in comparison with EIS

The broadband techniques took approximately one hundred seconds to complete. This time corresponds to two cycles of the lowest frequency component. This time taken for the broadband techniques to complete is determined by the period of the lowest frequency component and the number of cycles of the lowest frequency component. The time taken for EIS was approximately 10 minutes without accounting for the two-minute recovery time between two successive frequency point impedance measurements. The total time therefore for EIS came to approximately forty minutes as shown in Table 4.1. Because of the short duration of the broadband impedance measurement techniques, they can be applied to cells in online environments as they would be completed in a very short time span, eliminating the necessity of disconnecting the cell from its system or the environment under which it is operating. Furthermore, because broadband impedance measurements can be performed within one period of the lowest frequency [3], the need for a recovery time between measurements is eliminated.

4.3.8 Signal analysis

i. EIS/BIS

The results from EIS and BIS were analysed according to the process shown in Figure 4-12 below. The LabVIEW VI that implements this shown in Figure 9-3 in the APPENDIX.

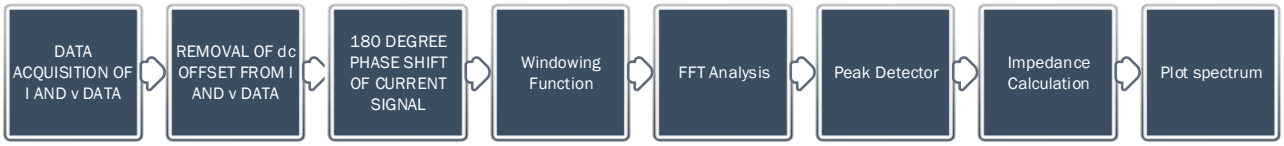

Figure 4-12: Signal analysis for EIS as well as BIS from LabVIEW

ii. Synchronous detection

Synchronous detection was also performed as shown in Figure 4-13 and the LabVIEW VI that implements this process is shown in Figure 9-2 of the Appendix.

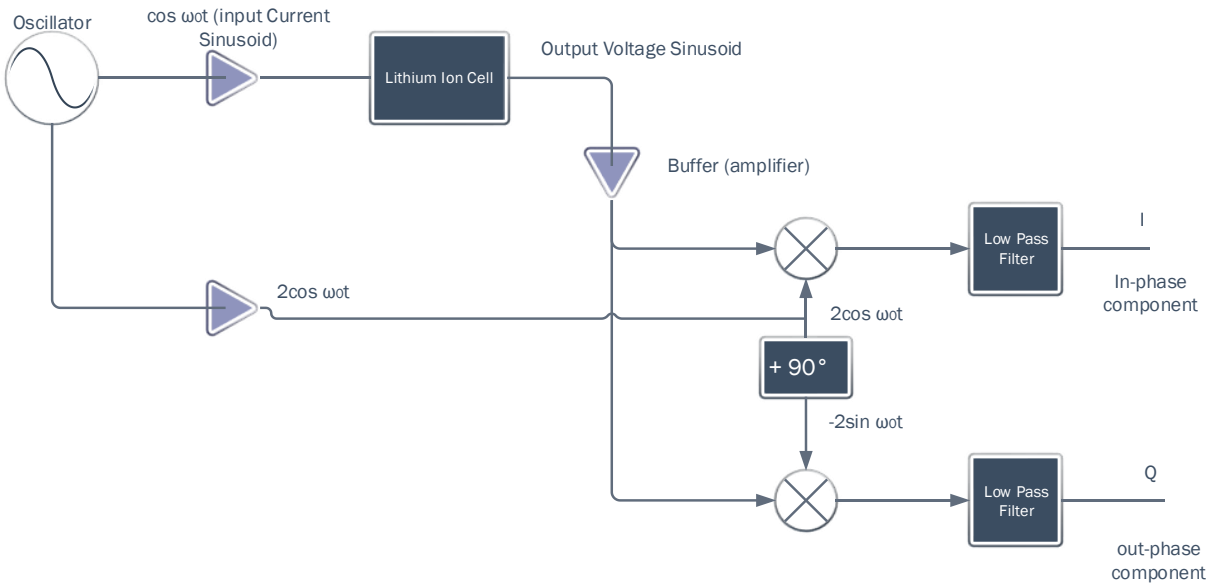

Figure 4-13: Synchronous detection schematic diagram

The synchronous detection technique was used to extract both phase and magnitude information from the signals. From the above block diagram, we can see that the input current sinusoid is injected into the Li-ion cell. Its response is then multiplied by the sinusoidal component it was generated with and another that has been phase shifted by 90° to obtain the in-phase and quadrature components of the signal. The signals are then passed through a low pass filter.

The input sinusoid can be represented as:

$$I = I_a \cos(\omega t) \tag{52}$$

After passing it through the cell, the voltage response is a scaled and phase shifted version of the current at the input, provided the cell is operating within its linear region. To ensure the cell is operating within its linear region, the excitation current is kept small enough such that the output voltage response amplitude at each frequency point does not exceed 10mV [58]. The voltage response at the output in the linear region of operation of the cell is therefore given by the equation:

$$V = kI_a \cos(\omega t + \theta) = V_a \cos(\omega t + \ \theta) \tag{53}$$

From the block diagram, it is observed that the output voltage signal is multiplied by the two sinusoidal components.

To extract the in-phase component of the signal, the voltage signal is multiplied by a sinusoid of the same frequency and phase as was used in the current injection. A scaling factor of two is used.

From the block diagram, the in-phase component is given by:

$$V_o(in\ phase) = V_a \cos(\omega t + \theta) \times 2\cos(\omega t) \tag{54}$$

From the trigonometric identity $\cos A \times \cos B = \frac{1}{2}(\cos(A+B) + \cos(A-B))$, we can express equation (54) as a sum of its two frequency components:

$$V_o(in\ phase) = 2V_a \times \frac{1}{2}(\cos(2\omega t + \theta) + \cos(\theta)) \tag{55}$$

which are then passed through a low pass filter to eliminate the higher frequency component, leaving only the DC term:

$$V_o(in\ phase) = V_a \cos\theta \tag{56}$$

And similarly, to extract the quadrature component of the signal, the voltage signal is multiplied by a sinusoid of the same frequency but phase shifted by ninety degrees. A scaling factor of two was used.

We can observe that in the block diagram, the quadrature component is given by:

$$V_o(out\ of\ phase) = V_a \cos(\omega t + \theta) \times -2\sin(\omega t) \tag{57}$$

From the trigonometric identity, $\cos A \times \sin B = \frac{1}{2}(\sin(A+B) - \sin(A-B))$, we can express the quadrature component as an algebraic sum of its frequency components:

$$V_o(out\ of\ phase) = V_a \sin(2\omega t + \theta) + V_a \sin\theta \tag{58}$$

This signal is also then passed through a low pass filter to eliminate the higher frequency component leaving only the DC term:

$$V_o(out\ of\ phase) = V_a \sin\theta \tag{59}$$

Trigonometrical equations were then applied to obtain both V_a and θ, which correspond to the magnitude of the voltage amplitude and the phase shift for that particular frequency.

$$\begin{aligned} V_a &= \sqrt{((V_a \sin(\theta))^2 + (V_a \cos(\theta))^2}, \\ \theta &= \tan^{-1}\frac{V_a \sin\theta}{V_a \cos\theta} \end{aligned} \tag{60}$$

5. Experimental Results and Discussion

5.1 EIS with SOC Variation

Figure 5-1 shows the Nyquist plot for a variation of the SOC at a DC bias of 0.4A for the EIS technique. The graphs showed a general reduction in the size of the charge transfer resistance loop as the state of charge was increased.

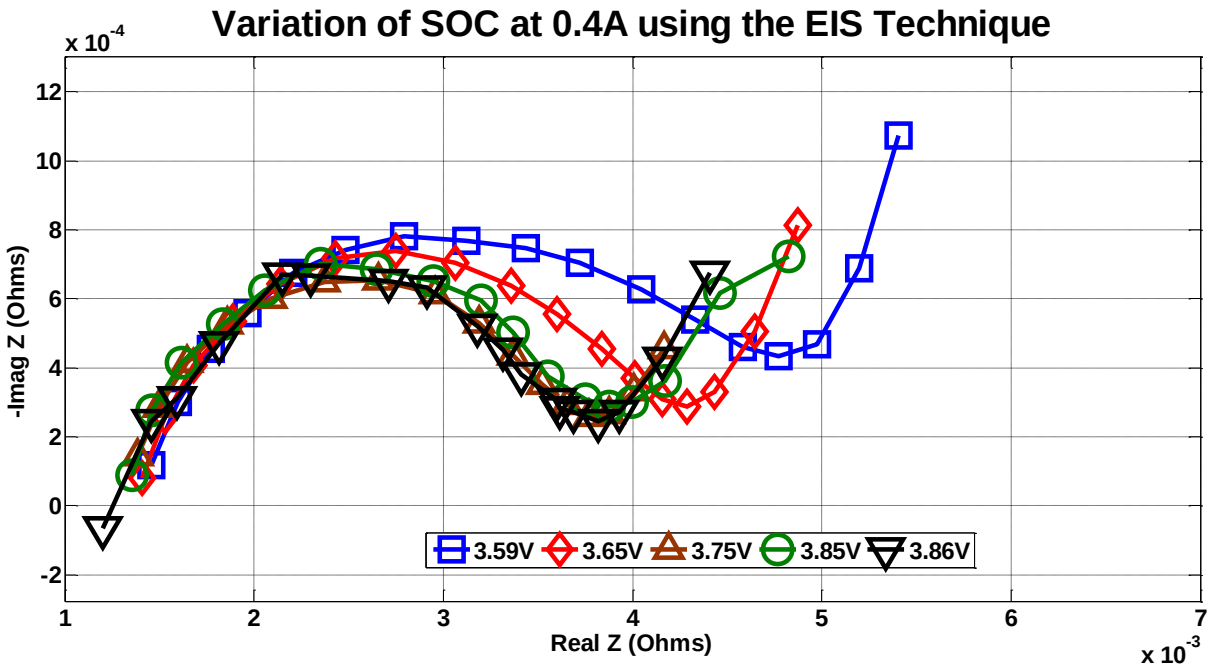

Figure 5-1: Variation of impedance spectra at different SOCs

5.2 Comparison of EIS with the Broadband Techniques at Different SOC

Figure 5-2 and Figure 5-3 showed that the impedance plots for the three impedance techniques compared well at a particular state of charge and DC current bias. The slight variances caused in impedance spectra between the broadband techniques and EIS results can be accounted for due to the longer time it takes to obtain the frequency impedance spectra for EIS. Both the BIS technique as well as the HCSD were carried out in under sixty for one cycle of the lowest frequency. The EIS took about ten minutes without accounting for the recovery period between successive frequency point impedance measurements, and forty minutes to complete when the recovery time is considered.

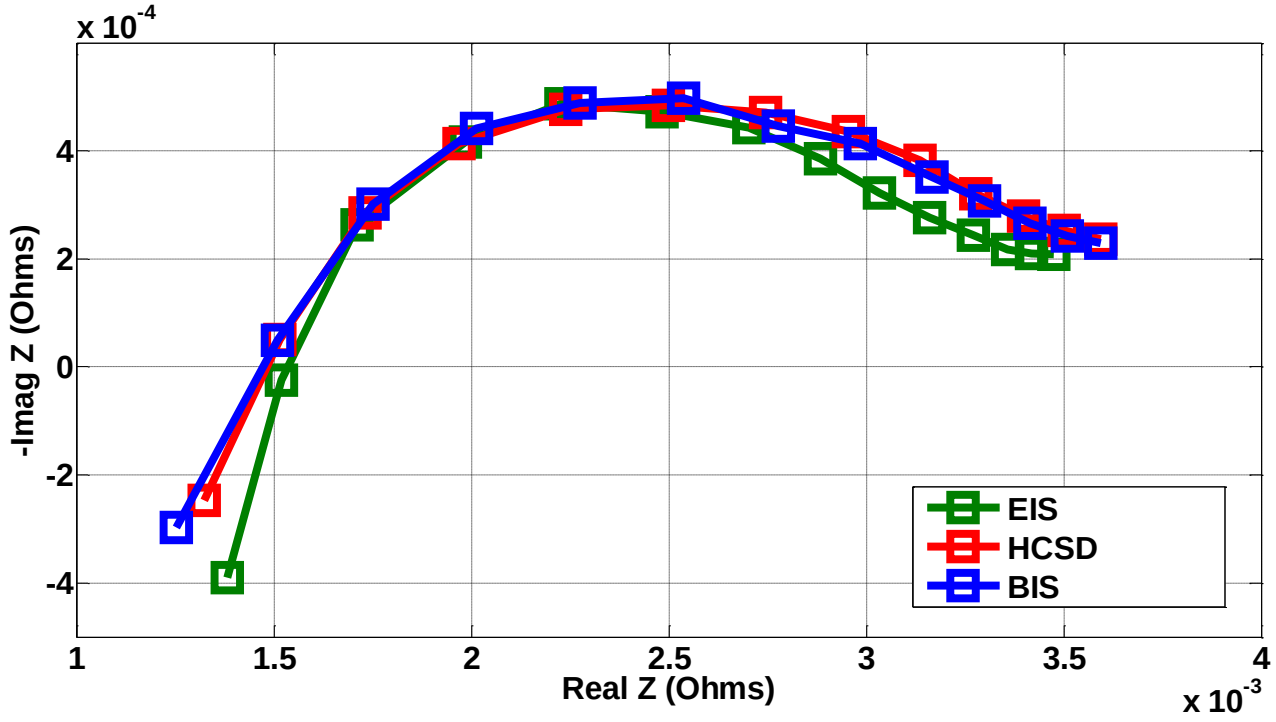

Figure 5-2: Variation of results from EIS, HCSD and BIS experiments at 3.66 OCV

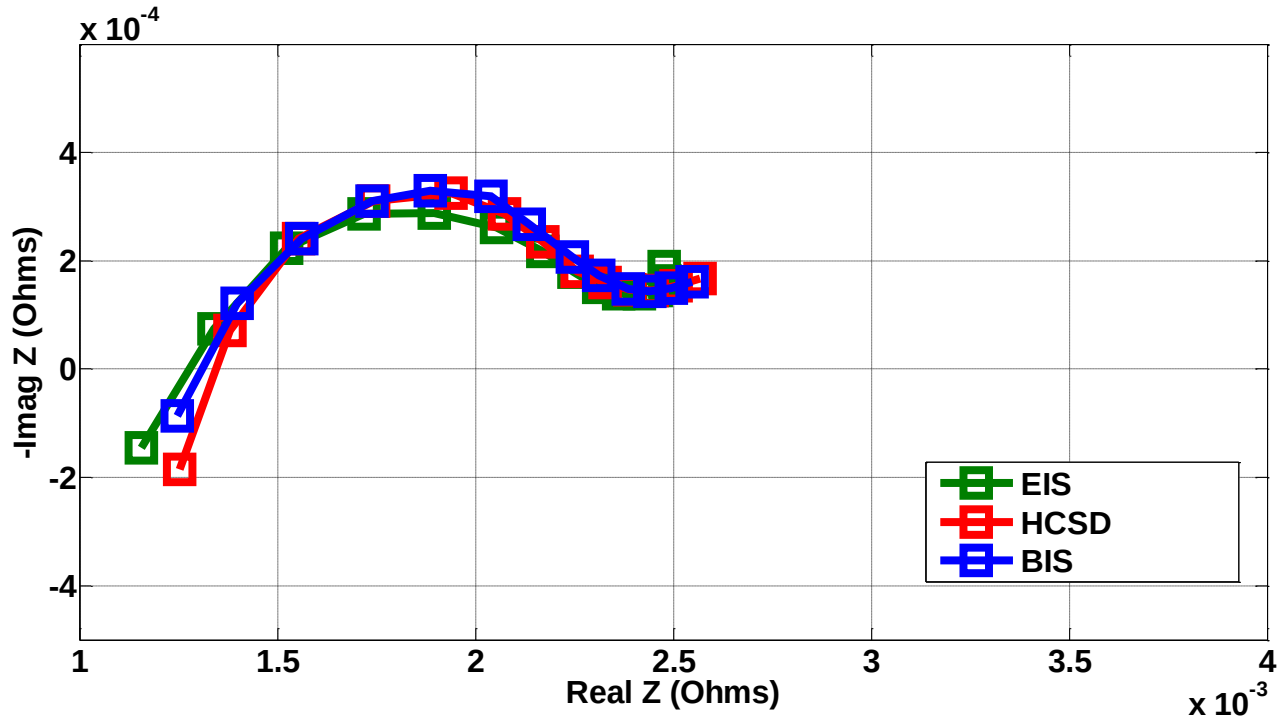

Figure 5-3: Variation of EIS, HCSD and BIS impedance plots at 4.12 OCV

5.3 Comparison of EIS with the Broadband Techniques at Different DC Biases

Figure 5-4 shows the variation of impedance spectra with DC bias for the NCM cells tested at 25°C using EIS. At this temperature, it was observed that the size of the charge transfer

resistance loop reduced slightly with an increase in in DC bias current. This indicated that the charge transfer resistance dropped with an increase in DC Bias. This relation is shown in equation (18). This change in the size of the charge transfer resistance loop was not as prominent as the one caused by the change in SOC. The reason for this effect is that higher temperatures increase the value of i_0 calculated using (19) and reduce the effect of DC bias on R_{ct} in (18). At 25°C the temperature is high enough such that the effect of the DC bias on the charge transfer resistance is less than the effect of the change in SOC on the charge transfer resistance. If the temperature is reduced, the value of i_0 reduces, which in turn increases the size of the charge transfer resistance. The increase of the size of the charge transfer resistance at lower temperatures due to the reduction of DC bias current becomes more evident. This phenomenon is explored in [26]. These results are like the ones obtained for LiFePO4 cell chemistry at 25°C using EIS.

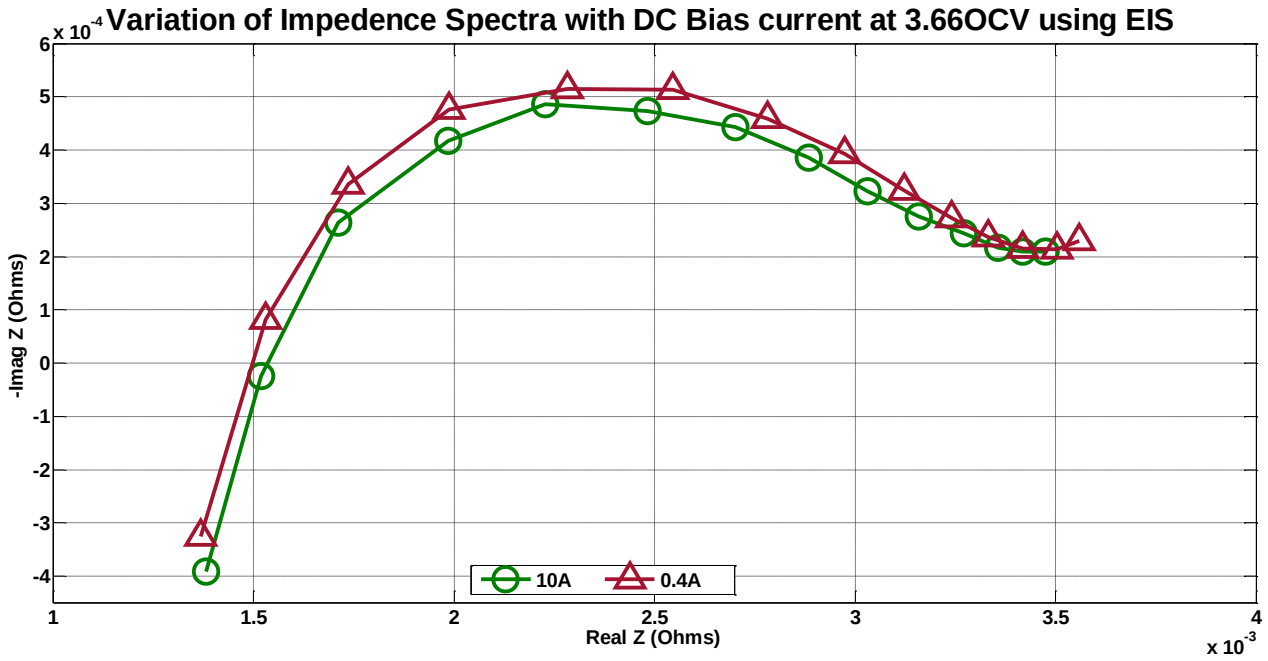

Figure 5-4: Variation of impedance spectra with dc bias at 3.66 OCV using EIS

Both HCSD and BIS capture the variation of impedance spectra with DC Bias current at 25°C adequately as shown in Figure 5-4 and Figure 5-5 respectively.

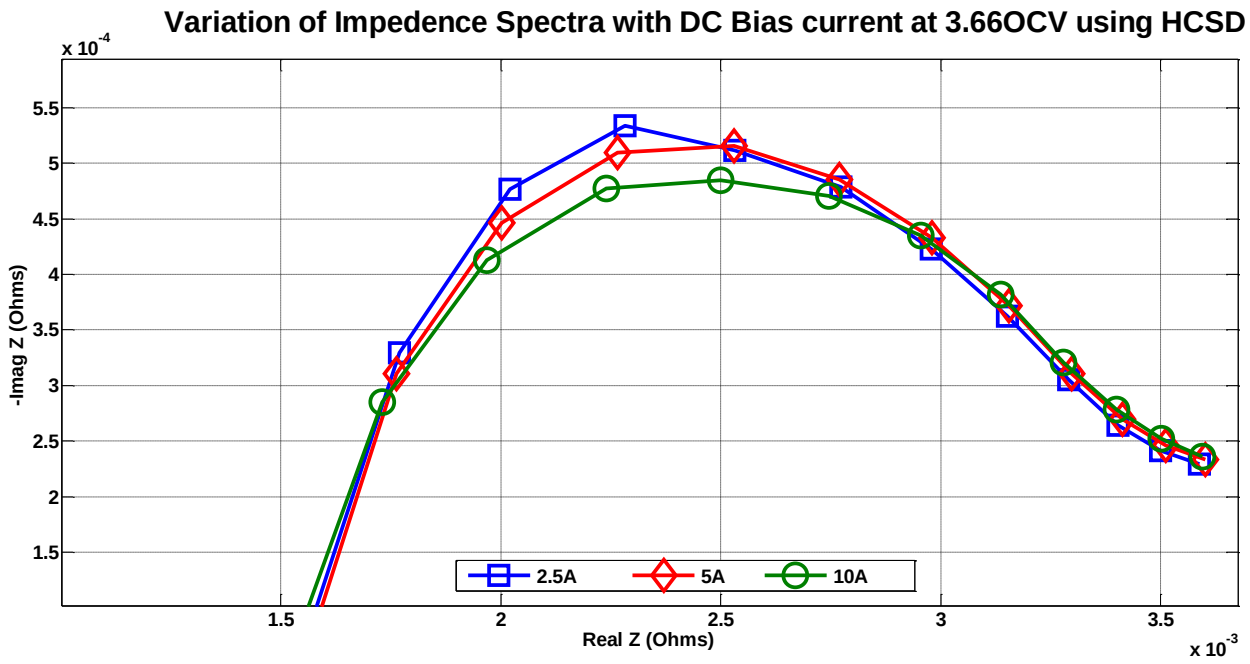

Figure 5-5: Variation of impedance spectra with DC BIAS current at 3.66OCV using HCSD

Both methods showed a slight reduction in the charge transfer resistance loop as the DC current is increased. This signals a reduction in the charge transfer resistance.

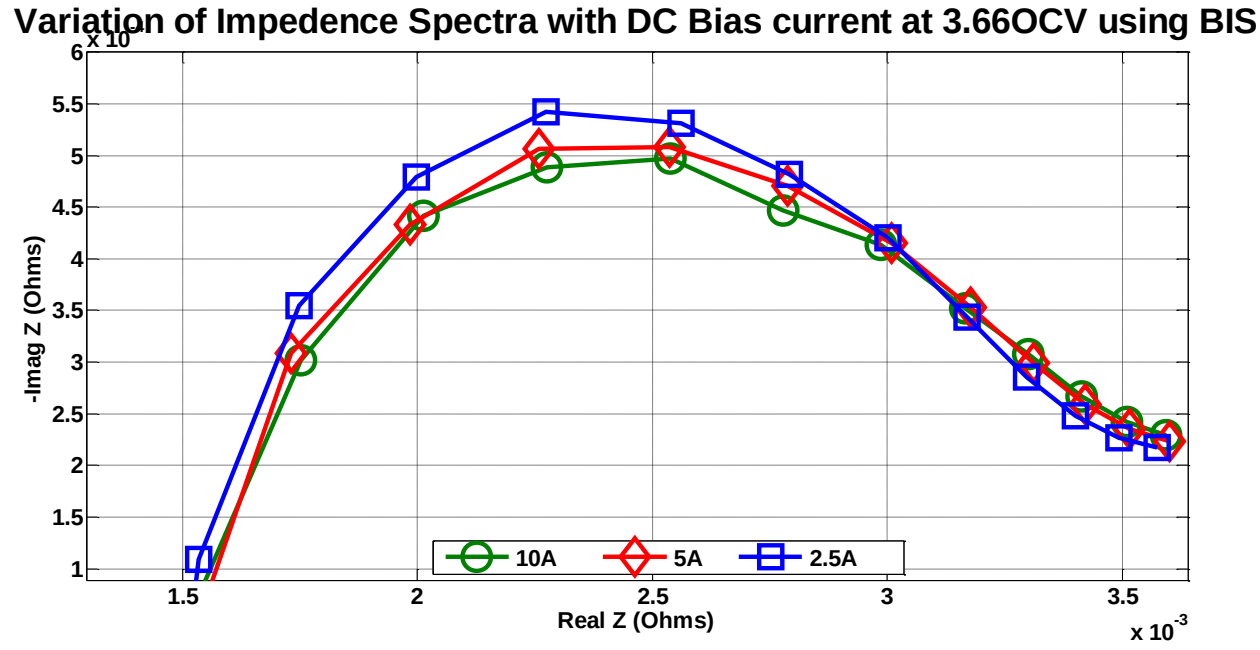

Figure 5-6: Variation of impedance spectra with DC Bias at 3.66OCV using BIS

5.4 A Comparison of the HCSD and BIS Techniques

The impedance spectra for BIS and HCSD was compared for different states of charge. It was found that as the state of charge increased, the size of the charge transfer resistance loop decreased, however the HCSD technique was not capable of distinguishing between the impedance spectra at the higher states of charge in comparison to the BIS technique. As shown in Figure 5-2 and Figure 5-3, the higher the state of charge, the lower the cell impedance and vice versa. Therefore, optimizing the amplitude spectrum in the BIS technique by means of the inverse magnitude spectrum ensures that the higher frequency regions with low impedance are sufficiently excited to improve the output signal to noise ratio. This reduces the uncertainty in the impedance frequency response at low impedance states characterised by high state of charge and high frequency. This is shown in Figure 5-7 and Figure 5-8 below. Furthermore, because of this profile, the excitation in the low frequency region where the magnitude of the voltage response is at its greatest is under 10mV, which is low enough for the cell to be operating within a linear region[58].

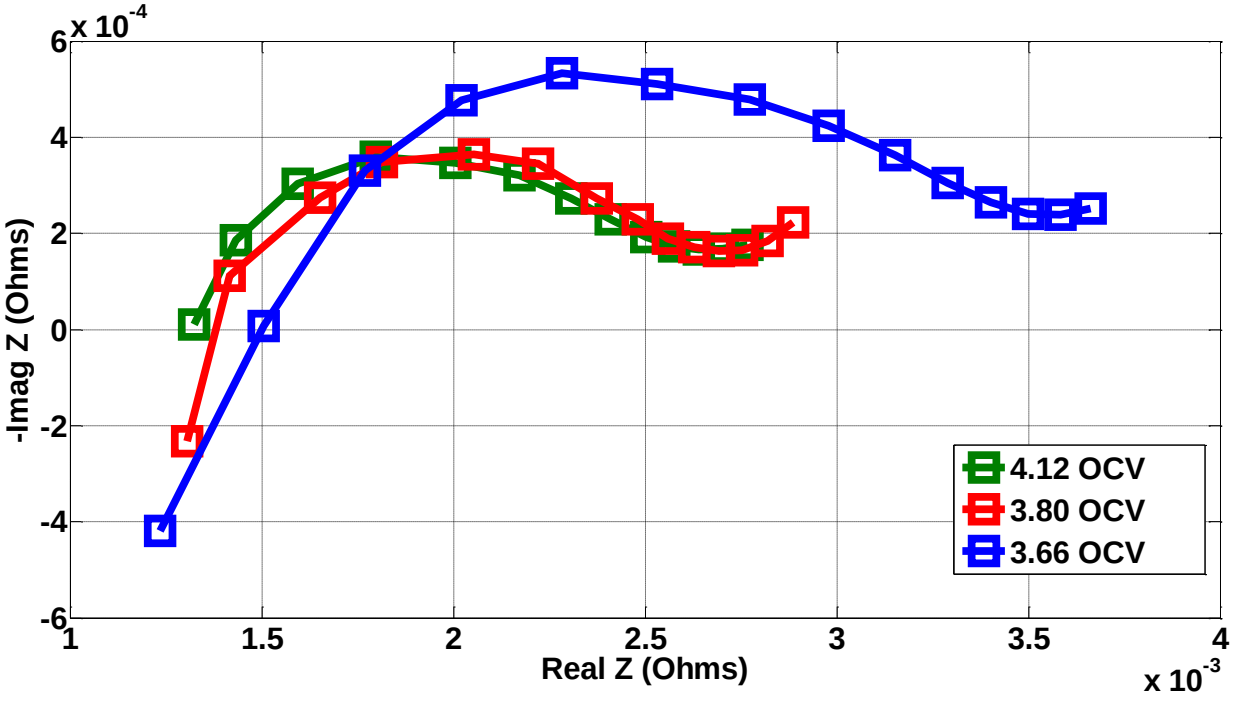

Figure 5-7: Impedance plot for Li-ion cell from HCSD experiment at different OCVs

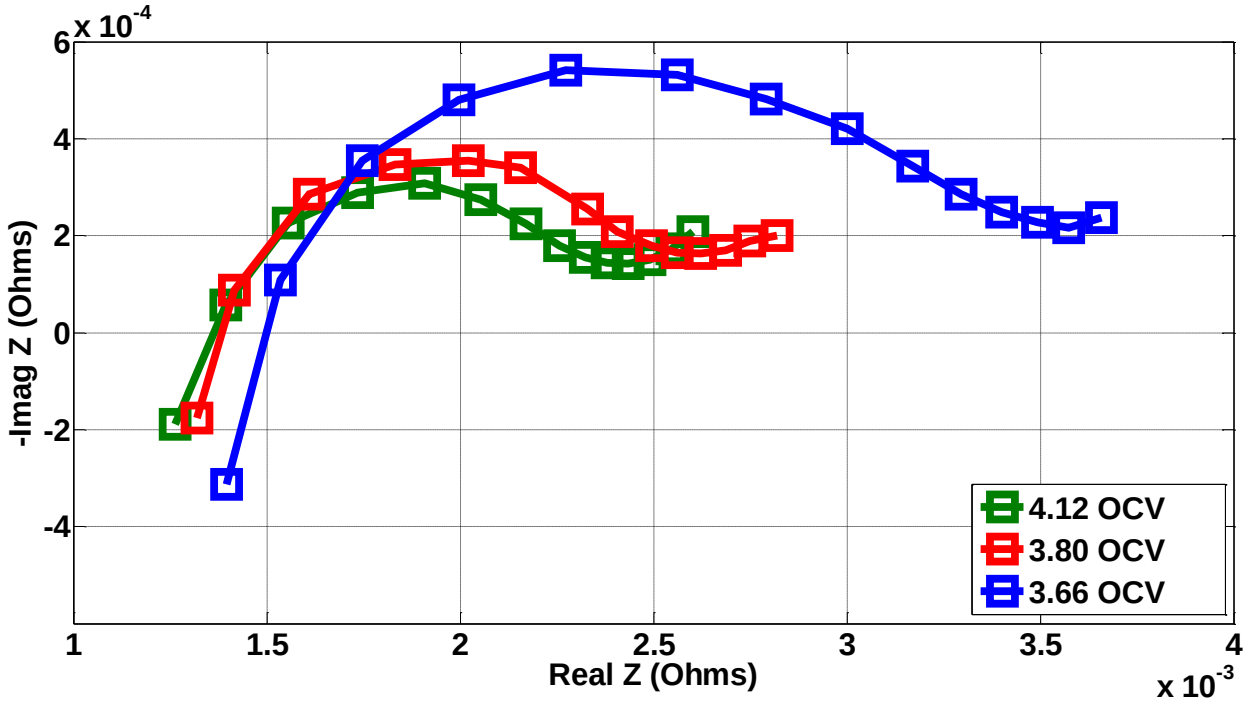

Figure 5-8: Impedance plot from BIS experiment at different OCVs

5.5 Concluding Remarks from Results

- There was a general reduction in the size of the charge transfer resistance loop as the state of charge was increased. Since the charge-transfer resistance loop edges closer to the x axis as the state of charge is increased, it is easier to estimate the charge transfer resistance at higher states of charge, as opposed to lower states of charge. Because of this relationship between the charge transfer resistance and SOC, it can be used to estimate the state of charge of the cell.
- Conducting an EIS test, took approximately ten minutes (without accounting for rest periods) while BIS, HCSD took approximately one hundred seconds. Because of the short duration of the broadband impedance measurement techniques, in comparison with EIS, they can be applied to cells in online environments. This would allow the measurement to be completed in a very short time span, eliminating the necessity of disconnecting the cell from its system or the environment under which it is operating.
- The broadband impedance techniques could replicate the information from EIS in the middle and high frequency regions (i.e. 1Hz and greater).
- EIS can provide more reliable impedance spectra as compared to the broadband techniques in the lower frequency regions because the limited amount of time to record

the lower frequency cycles in the broadband techniques means that the frequency resolution in the lower frequency regions of the FFT is low for the broadband signals.

- EIS with a DC Bias is limited to frequencies greater than 1Hz as any measurements performed at lower frequencies result in a significant change in the state of charge of the cell for the required number of cycles.

6. Equivalent Circuit Modelling and Parameter Extraction

A full EIS was performed on the cell to obtain the initial impedance spectra. The EIS was carried out at 3.75V DC and 0.4A DC Bias and at room temperature. This was done to obtain the general shape of the EIS curve from which the model was to be derived. A typical impedance plot is shown in Figure 6-1.

By observing the EIS graph obtained, a corresponding model for the cell was derived using the techniques discussed in section 2.6.5.

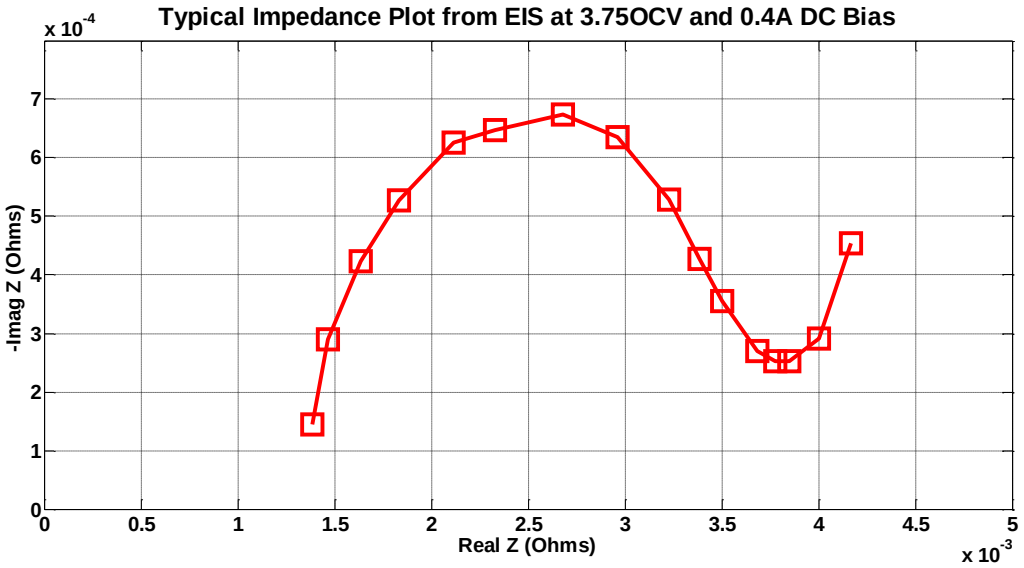

Figure 6-1: Typical impedance plot from EIS experiment

6.1 Choice of Equivalent Circuit Model

By observing the impedance spectrum from various measurements at different open circuit voltages and DC bias currents, the equivalent circuit model below was chosen. The parallel combination of a constant phase element with a resistor, which is sometimes referred to as a Z_{arc} element, is shown on the impedance spectra as a loop. The equivalent circuit consisted of an inductor in series with a resistor and two parallel combinations of Z_{arc} elements, shown in Figure 6-2. The Z_{arc} elements represent the charge transfer resistance loop and the loop associated with the diffusion processes.

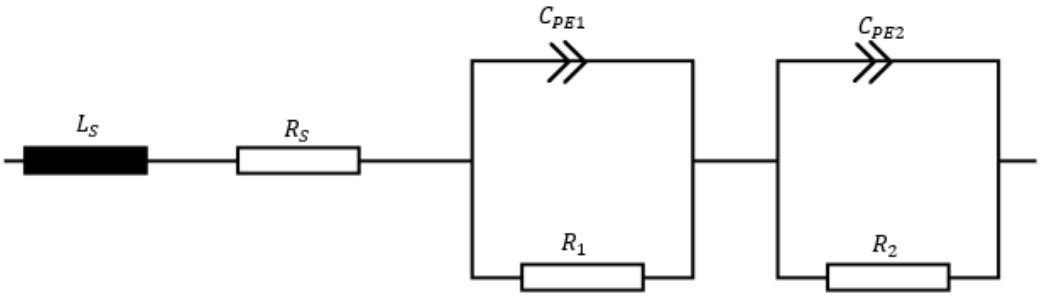

Figure 6-2: Equivalent circuit model chosen for the analysis

The impedance of the above circuit can be computed as:

$$Z_T = j\omega L_S + R_S + \frac{1}{\frac{1}{R_1} + C_{PE1}.(j\omega)^{\psi_1}} + \frac{1}{\frac{1}{R_2} + C_{PE2}.(j\omega)^{\psi_2}} \tag{61}$$

6.2 Parameter Extraction

A similar procedure to the one carried out in [35] was used to extract the model parameters. The depression factors ψ_1 and ψ_2 as well as the inductance L_s were fixed at 0.8, 0.6 and $5 \times 10^{-7} H$ respectively, and a complex non linear least squares algorithm (see attached matlab script in the appendix) was used to extract the parameters from the model for each spectrum obtained. Figure 6-5 shows the effect of varying the depression factor. The spectrum produced from the model was then compared with the measured data spectrum in a similar way to [48]. It was found that the model fitted well with the experimental results during the tests at different open circuit voltages as shown in Figure 6-3 and Figure 6-4.

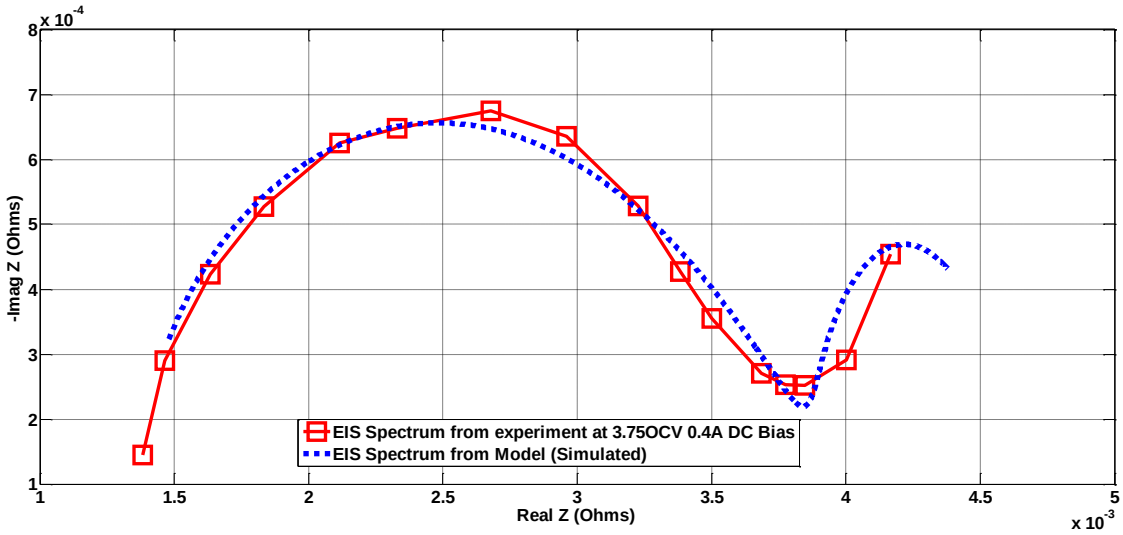

Figure 6-3: Comparison of Experimental EIS with Simulated EIS Spectra from the chosen model

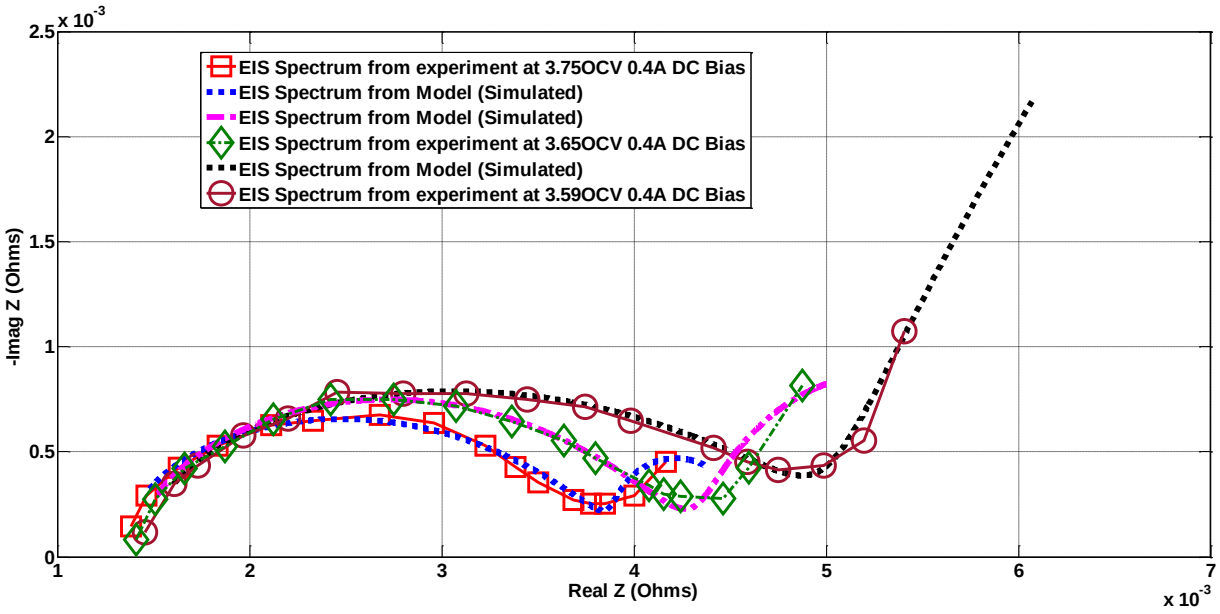

Figure 6-4: Comparison of Experimental EIS at different SOC with model simulated spectra

The effect of varying the depression factor gave rise to the reduction in the size of the charge transfer resistance loop in the simulated spectrum. This is shown in Figure 6-5. These results are also depicted in [26].

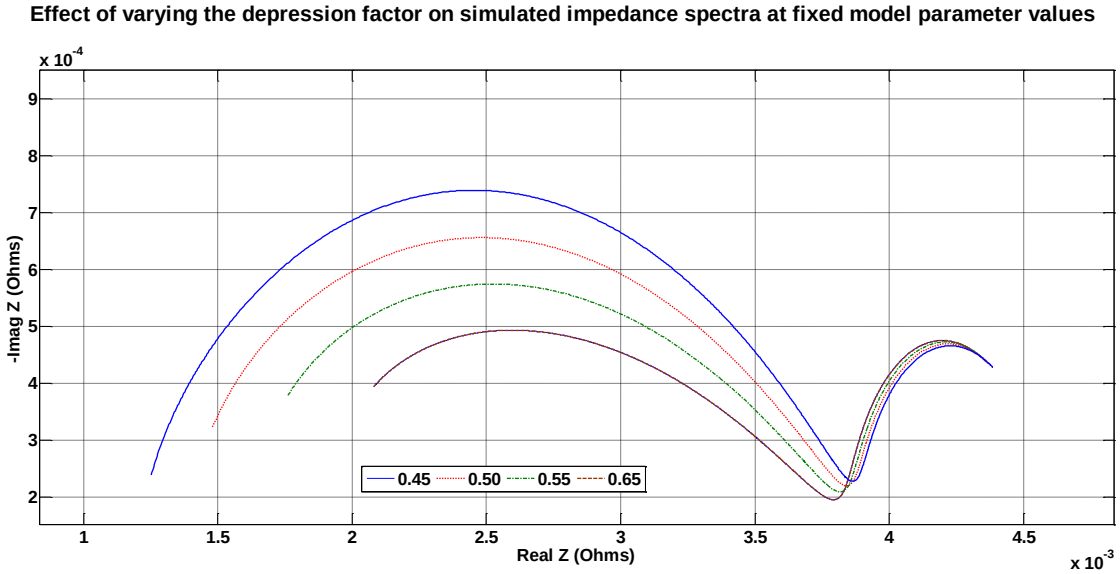

Figure 6-5: Effect of varying the depression factor on simulated EIS spectrum with fixed R1, R2, Ls, CPE2 values

6.3 Representation of Parameters

For each state of charge, the non-fixed model parameters, i.e. $R_1, R_2, R_S,\ CPE1, CPE2$ were extracted and plotted on a two-dimensional axis with the parameter on the Y-axis and the open circuit voltage on the X-axis.

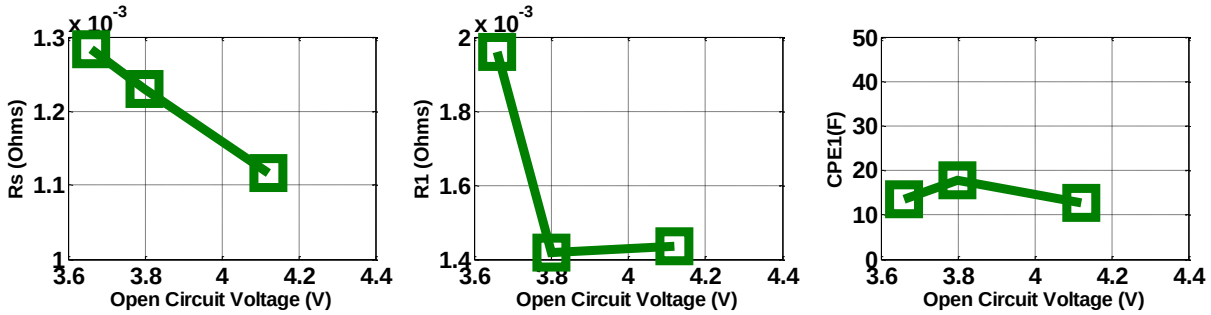

Figure 6-6: Sample representation of parameter variation representation

6.4 Variation of Parameters at Different States of Charge for EIS

Figure 6-7 shows the variation in the model parameters at different states of charge for EIS. The increase in SOC showed a reduction in the size of the ohmic resistance R_s and a reduction in R_1, the resistance associated with the charge transfer process, which corresponds with the findings arrived at by Li Rian et. al., [59] . The parameter R_2 which is associated with the diffusion process is shown to increase whereas the generalized capacitance CPE1 remains constant. The generalized capacitance CPE2 is shown to increase with SOC.

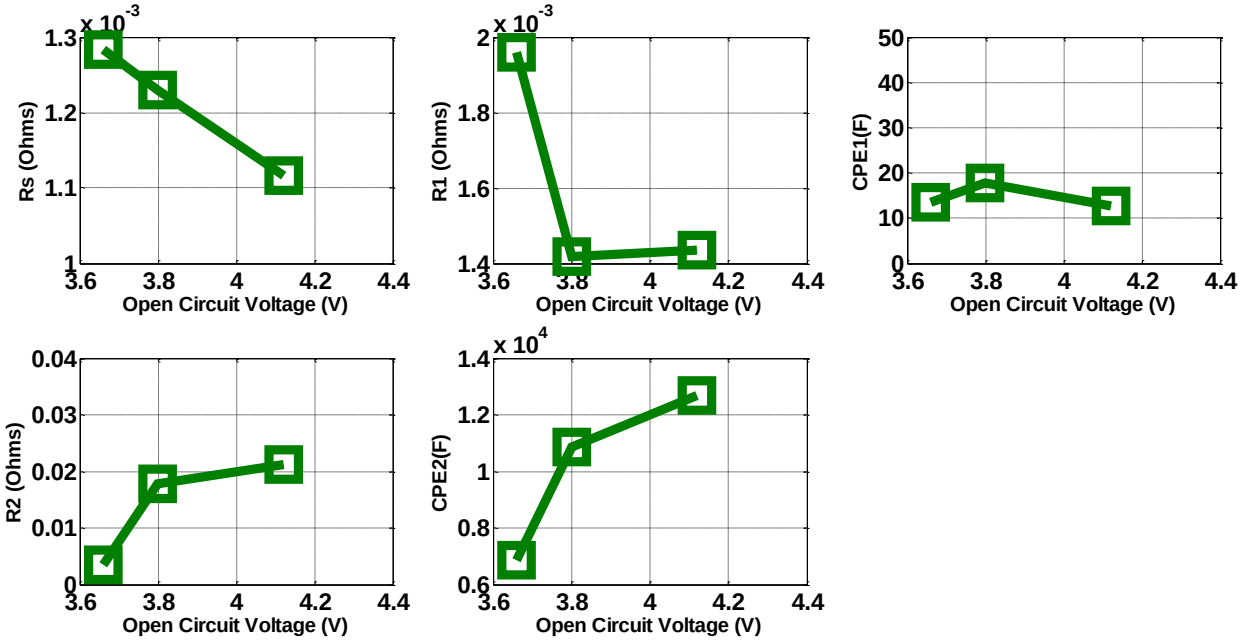

Figure 6-7: Variation of the different parameters with SOC from EIS experiment

6.5 EIS Parameter Extraction Comparison with BIS

The results obtained by varying the state of charge and model parameters for BIS were compared with EIS. The results proved to be similar for both techniques as shown in Figure 6-8 below.

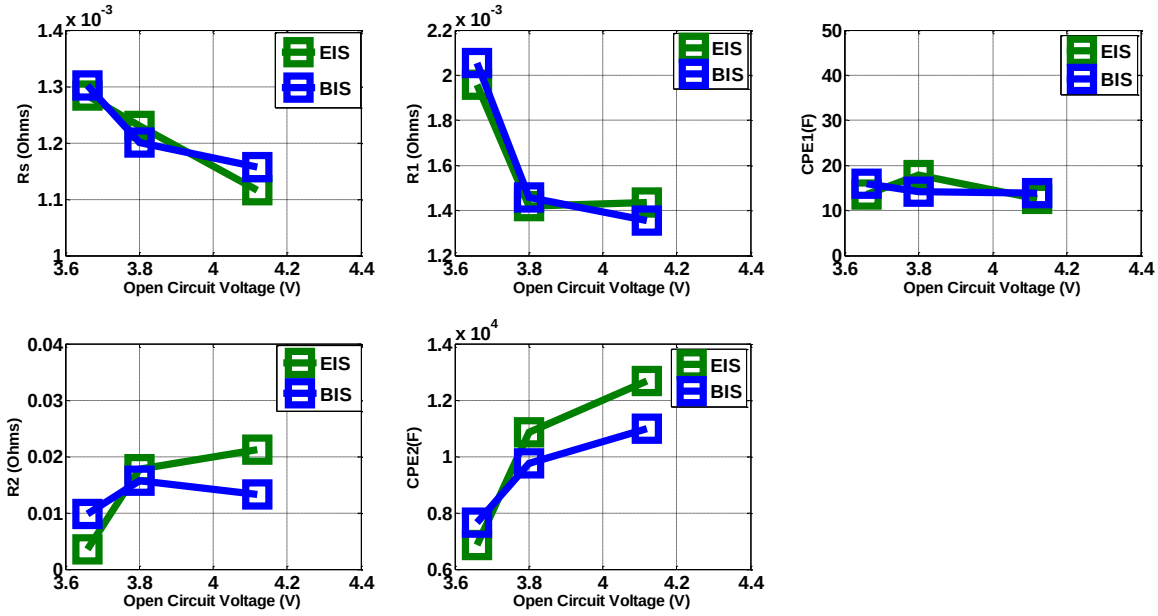

Figure 6-8: Parameter comparison between EIS and BIS

7. Conclusions

The purpose of this study was to compare the spectra obtained by EIS, and the broadband signal techniques, as well as to assess the viability of the broadband technique as an alternative approach to acquiring impedance spectra for Li-ion cells online.

- The overall time required to conduct an EIS experiment indicates that it is unsuitable for rapid online condition monitoring, whereas Multisine approaches such as HCSD and BIS, allow for full impedance measurement within one period of the minimum excitation frequency, thus drastically reducing the measurement time and making it more suitable for online condition monitoring.
- Galvanostatic EIS on Li-ion cells in the presence of a DC Bias current must be performed carefully so as not to alter the state of charge i.e. at low frequencies, the number of cycles that can be recorded is reduced.
- The results show that the broadband impedance spectroscopy method is a suitable alternative to both EIS and HCSD in the determination of EIS spectra at room temperature. It adequately captures the variation of SOC as well as DC bias. BIS is suitable in applications where there is sufficient computational power for FFT analysis. HCSD avoids the use of performing FFT based computation; however, there is an additional step which requires synchronous detection and a low pass filter.
- Since both BIS and HCSD involve summing up different frequency sinusoids separated by a factor which is a power of two, of the fundamental, they are faced with the problem of having a lower resolution especially at higher frequencies. It is worth also noting that though both methods can extract impedance spectra from one period of the lowest frequency, the impedance spectra were obtained for a minimum of three periods. This was to allow for the voltage response at lower frequencies to reach steady state prior to synchronous detection.
- It was also shown that using BIS in combination with a parameter extraction technique, which was based on the non-linear least squares algorithm, online condition monitoring can be achieved with a relatively high level of detailed information in a short period of time. Cell characteristics such as internal resistance can be monitored throughout the cell ageing process, as explained in the literature review, and have a direct correlation to the state of health of the cell.

8. Recommendations

As an extension of the work covered by this study, future work can involve using broadband techniques in:

- The determination of cell faults, and cell failure common to Li-ion cells.
- Full tests in an online environment which mimic a real-time load such as an electric vehicle that can predict state of charge.
- Using the models of the Li-ion cell to predict run-time performance.
- Condition monitoring of Li-ion cells at different stages of the ageing process. The cells can be made to undergo an accelerated ageing process, after which the impedance spectra in these conditions are studied.
- Assessing the viability of these broadband impedance techniques in the characterization of non-Li-ion based secondary cells such as lead acid cells.
- Assessing the different spectra obtained during varying temperature conditions.

References

[1] N. A. Chaturvedi *et al*, "Algorithms for advanced battery-management systems," *IEEE Control Systems,* vol. 30, *(3),* pp. 49-68, 2010.

[2] J. Tarascon and M. Armand, "Issues and challenges facing rechargeable lithium batteries," *Nature,* vol. 414, *(6861),* pp. 359-367, 2001.

[3] J. P. Christophersen *et al*, "Rapid Impedance Spectrum Measurements for State-of-Health Assessment of Energy Storage Devices," *SAE International Journal of Passenger Cars-Electronic and Electrical Systems,* vol. 5, *(2012-01-0657),* pp. 246-256, 2012.

[4] US Department Of Energy, "Battery test manual ForPlug-in hybrid electric vehicles," US Department of Energy, 2008.

[5] International Electrotechnical Commission, "Secondary cells and batteries containing alkaline or other non-acid electrolytes - secondary lithium cells and batteries for portable applications," 2011.

[6] C. de Beer, P. S. Barendse and P. Pillay, "Fuel Cell Condition Monitoring Using Optimized Broadband Impedance Spectroscopy," *IEEE Trans. Ind. Electron.,* vol. 62, *(8),* pp. 5306-5316, 2015.

[7] D. Linden, "Handbook of batteries," in *Fuel and Energy Abstracts,* 1995, pp. 265.

[8] University of Washington, "Classification of Cells or Batteries," 2017. Available: http://depts.washington.edu/matseed/batteries/MSE/classification.html.

[9] NASA, "Curiosity's Daily Update: Curiosity Closes in on its New 'Home'," 2012. Available: http://mars.nasa.gov/msl/news/whatsnew/index.cfm?FuseAction=ShowNews&NewsID=1282.

[10] B. Lawson, "Cell-chemistries-How batteries Work," 2005.

[11] Nova Battery Systems, "Inside Lithium Ion Battery," 2016.

[12] I. Buchmann, "Types of Lithium-Ion," 2015.

[13] A. D. Robertson and P. G. Bruce, "Mechanism of electrochemical activity in Li2MnO3," *Chemistry of Materials,* vol. 15, *(10),* pp. 1984-1992, 2003.

[14] The Boston Consulting Group, "Batteries for Electric cars," 2010.

[15] R. Klein *et al*, "Electrochemical model based observer design for a lithium-ion battery," *IEEE Trans. Control Syst. Technol.,* vol. 21, *(2),* pp. 289-301, 2013.

[16] M. Chen and G. A. Rincon-Mora, "Accurate electrical battery model capable of predicting runtime and IV performance," *IEEE Trans. Energy Convers.,* vol. 21, *(2),* pp. 504-511, 2006.

[17] M. Pedram and Q. Wu, "Design considerations for battery-powered electronics," in *Proceedings of the 36th Annual ACM/IEEE Design Automation Conference,* 1999, pp. 861-866.

[18] C. Chiasserini and R. R. Rao, "Energy efficient battery management," *IEEE J. Select. Areas Commun.,* vol. 19, *(7),* pp. 1235-1245, 2001.

[19] L. Cai and R. E. White, "Mathematical modeling of a lithium ion battery with thermal effects in COMSOL Inc. Multiphysics (MP) software," *J. Power Sources,* vol. 196, *(14),* pp. 5985-5989, 2011.

[20] M. Valvo *et al*, "Development and application of an improved equivalent circuit model of a lead acid battery," in *Energy Conversion Engineering Conference, 1996. IECEC 96., Proceedings of the 31st Intersociety,* 1996, pp. 1159-1163.

[21] M. Ceraolo, "New dynamical models of lead-acid batteries," *IEEE Trans. Power Syst.,* vol. 15, *(4),* pp. 1184-1190, 2000.

[22] S. Buller *et al*, "Impedance-based simulation models of supercapacitors and Li-ion batteries for power electronic applications," *IEEE Trans. Ind. Appl.,* vol. 41, *(3),* pp. 742-747, 2005.

[23] P. Baudry *et al*, "Electro-thermal modelling of polymer lithium batteries for starting period and pulse power," *J. Power Sources,* vol. 54, *(2),* pp. 393-396, 1995.

[24] S. C. Hageman, "Simple PSpice models let you simulate common battery types," *Edn,* vol. 38, *(22),* pp. 117-&, 1993.

[25] S. Gold, "A PSPICE macromodel for lithium-ion batteries," in *Battery Conference on Applications and Advances, 1997., Twelfth Annual,* 1997, pp. 215-222.

[26] D. Andre *et al*, "Characterization of high-power lithium-ion batteries by electrochemical impedance spectroscopy. II: Modelling," *J. Power Sources,* vol. 196, *(12),* pp. 5349-5356, 2011.

[27] M. Charkhgard and M. Farrokhi, "State-of-charge estimation for lithium-ion batteries using neural networks and EKF," *IEEE Trans. Ind. Electron.,* vol. 57, *(12),* pp. 4178-4187, 2010.

[28] H. He, R. Xiong and J. Fan, "Evaluation of lithium-ion battery equivalent circuit models for state of charge estimation by an experimental approach," *Energies,* vol. 4, *(4),* pp. 582-598, 2011.

[29] B. Lawson, "Lithium Battery Failures," 2016.

[30] S. Piller, M. Perrin and A. Jossen, "Methods for state-of-charge determination and their applications," *J. Power Sources,* vol. 96, *(1),* pp. 113-120, 2001.

[31] C. Ehret *et al*, "State-of-charge determination for lead-acid batteries in PV-applications," in *Proceedings of the 16th European Photovoltaic Solar Energy Conference, Glasgow,* 2000, pp. 2486-2489.

[32] A. J. Salkind *et al*, "Determination of state-of-charge and state-of-health of batteries by fuzzy logic methodology," *J. Power Sources,* vol. 80, *(1),* pp. 293-300, 1999.

[33] S. Rodrigues, N. Munichandraiah and A. Shukla, "A review of state-of-charge indication of batteries by means of ac impedance measurements," *J. Power Sources,* vol. 87, *(1),* pp. 12-20, 2000.

[34] F. Huet, "A review of impedance measurements for determination of the state-of-charge or state-of-health of secondary batteries," *J. Power Sources,* vol. 70, *(1),* pp. 59-69, 1998.

[35] D. I. Stroe *et al*, "Diagnosis of lithium-ion batteries state-of-health based on electrochemical impedance spectroscopy technique," in *2014 IEEE Energy Conversion Congress and Exposition (ECCE),* 2014, pp. 4576-4582.

[36] M. Hughes *et al*, "The impedance of 23 Ah Ni-Cd cells with sintered electrodes: measurements in the range 10 kHz-0.001 Hz as an indication of residual capacity," *J. Appl. Electrochem.,* vol. 15, *(1),* pp. 129-137, 1985.

[37] Z. Stoynov, B. Savova-Stoynov and T. Kossev, "Non-stationary impedance analysis of lead/acid batteries," *J. Power Sources,* vol. 30, *(1),* pp. 275-285, 1990.

[38] P. Roberge *et al*, "Non-destructive characterization of sealed lead/acid battery cells with electrochemical impedance spectroscopy," *J. Power Sources,* vol. 32, *(3),* pp. 261-270, 1990.

[39] D. Andre *et al*, "Characterization of high-power lithium-ion batteries by electrochemical impedance spectroscopy. I. Experimental investigation," *J. Power Sources,* vol. 196, *(12),* pp. 5334-5341, 2011.

[40] T. Momma *et al*, "Ac impedance analysis of lithium ion battery under temperature control," *J. Power Sources,* vol. 216, pp. 304-307, 2012.

[41] A. J. Bard *et al*, *Electrochemical Methods: Fundamentals and Applications.* Wiley New York, 1980*2*.

[42] L. W. Juang *et al*, "The impact of DC bias current on the modeling of lithium iron phosphate and lead-acid batteries observed using electrochemical impedance spectroscopy," in *2014 IEEE Energy Conversion Congress and Exposition (ECCE),* 2014, pp. 2575-2581.

[43] Gamry Instruments, "Basics of electrochemistry (EIS)," 2016.

[44] J. L. Morrison and W. H. Morrison, *Method of Detecting System Function by Measuring Frequency Response,* 2008.

[45] J. Morrison and W. Morrison, "Real time estimation of battery impedance," in *2006 IEEE Aerospace Conference,* 2006, pp. 13 pp.

[46] R. Hoffmann, J. Slade and J. Morrison, "Development and test of a real time battery impedance estimation system," in *2006 IEEE Aerospace Conference,* 2006, pp. 8 pp.

[47] E. Van der Ouderaa, J. Schoukens and J. Renneboog, "Peak factor minimization of input and output signals of linear systems," *IEEE Transactions on Instrumentation and Measurement,* vol. 37, *(2),* pp. 207-212, 1988.

[48] J. Ojarand, M. Min and P. Annus, "Crest factor optimization of the multisine waveform for bioimpedance spectroscopy," *Physiol. Meas.,* vol. 35, *(6),* pp. 1019, 2014.

[49] S. Boyd, "Multitone signals with low crest factor," *IEEE Transactions on Circuits and Systems,* vol. 33, *(10),* pp. 1018-1022, 1986.

[50] L. Ran *et al*, "Prediction of state of charge of lithium-ion rechargeable battery with electrochemical impedance spectroscopy theory," in *2010 5th IEEE Conference on Industrial Electronics and Applications,* 2010, pp. 684-688.

[51] W. Morrison *et al*, "An advanced calibration procedure for complex impedance spectrum measurements of advanced energy storage devices," in *58th International Instrumentation Symposium Proceedings,* 2012, .

[52] Thurlby Thandar Instruments Ltd., "QPX1200 DC power supply," .

[53] G. EIG, "EIG-ePLB-C020 high energy product," Energy Innovation Group, 2012.

[54] National Instruments, "NI 6366 X series data acquisition," National Instruments, .

[55] C. de Beer *et al*, "Electrical Circuit Analysis of CO Poisoning in High-Temperature PEM Fuel Cells for Fault Diagnostics and Mitigation," *IEEE Trans. Ind. Appl.,* vol. 51, *(1),* pp. 619-630, 2015.

[56] W. Haiying *et al*, "Study on correlation with SOH and EIS model of li-ion battery," in *Strategic Technology (IFOST), 2011 6th International Forum On,* 2011, pp. 261-264.

[57] National Instruments, "Understanding FFTs and Windowing," 2015.

[58] J. Illig, *Physically Based Impedance Modelling of Lithium-Ion Cells.* KIT Scientific Publishing, 2014*27*.

[59] L. W. Juang *et al*, "The impact of DC bias current on the modeling of lithium iron phosphate and lead-acid batteries observed using electrochemical impedance spectroscopy," in *2014 IEEE Energy Conversion Congress and Exposition (ECCE),* 2014, pp. 2575-2581.

[60] Thurlby Thandar Instruments Ltd., "DC electronic load, 80A, 80V, 300W," Thurlby Thandar Instruments Ltd., .

9. Appendices

9.1 Appendix A

Signal Content	Window
Sine wave or combination of sine waves	Hann
Sine wave (amplitude accuracy is important)	Flat Top
Narrowband random signal (vibration data)	Hann
Broadband random (white noise)	Uniform
Closely spaced sine waves	Uniform, Hamming
Excitation signals (hammer blow)	Force
Response signals	Exponential
Unknown content	Hann
Sine wave or combination of sine waves	Hann
Sine wave (amplitude accuracy is important)	Flat Top
Narrowband random signal (vibration data)	Hann
Broadband random (white noise)	Uniform
Two tones with frequencies close but amplitudes very different	Kaiser-Bessel
Two tones with frequencies close and almost equal amplitudes	Uniform
Accurate single tone amplitude measurements	Flat Top

Figure 9-1: Recommended windowing functions based on different applications

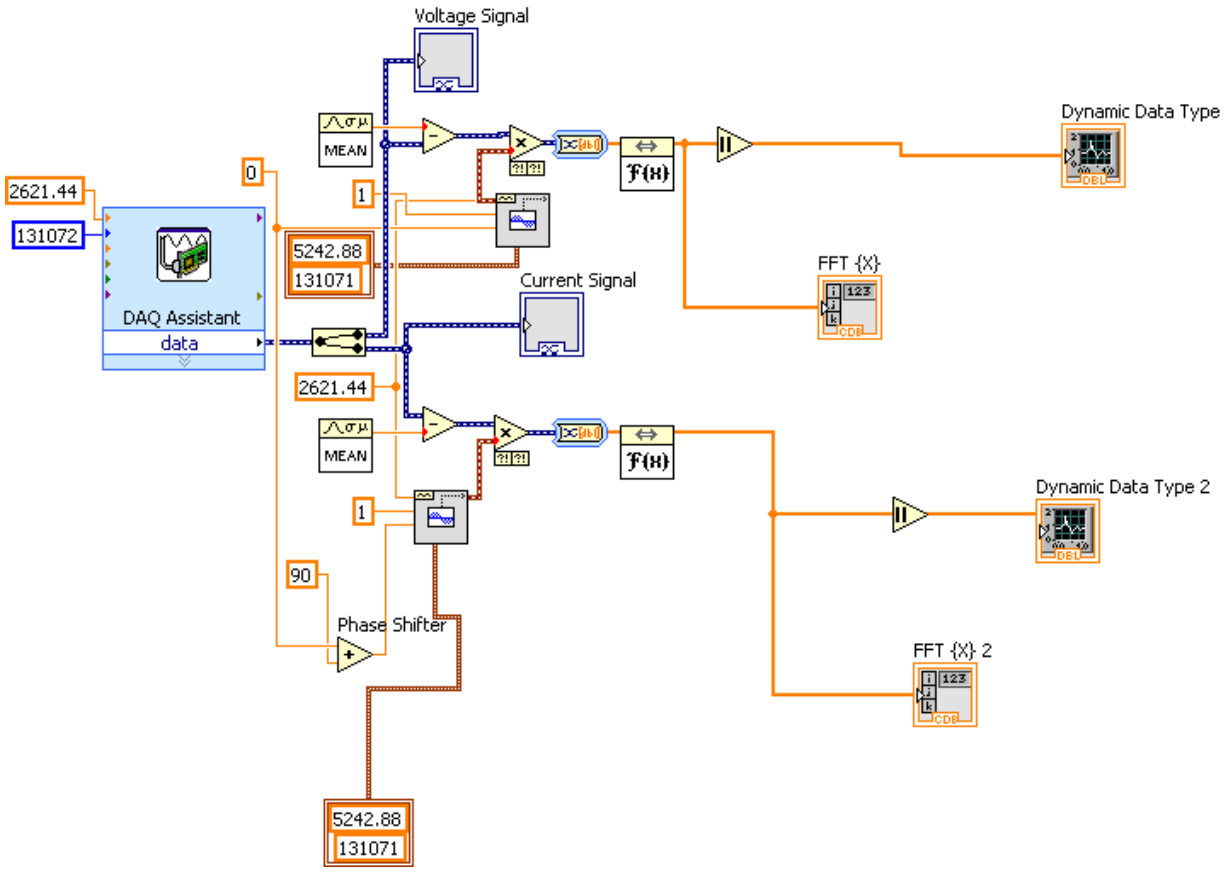

Figure 9-2: Synchronous detector VI MATLAB

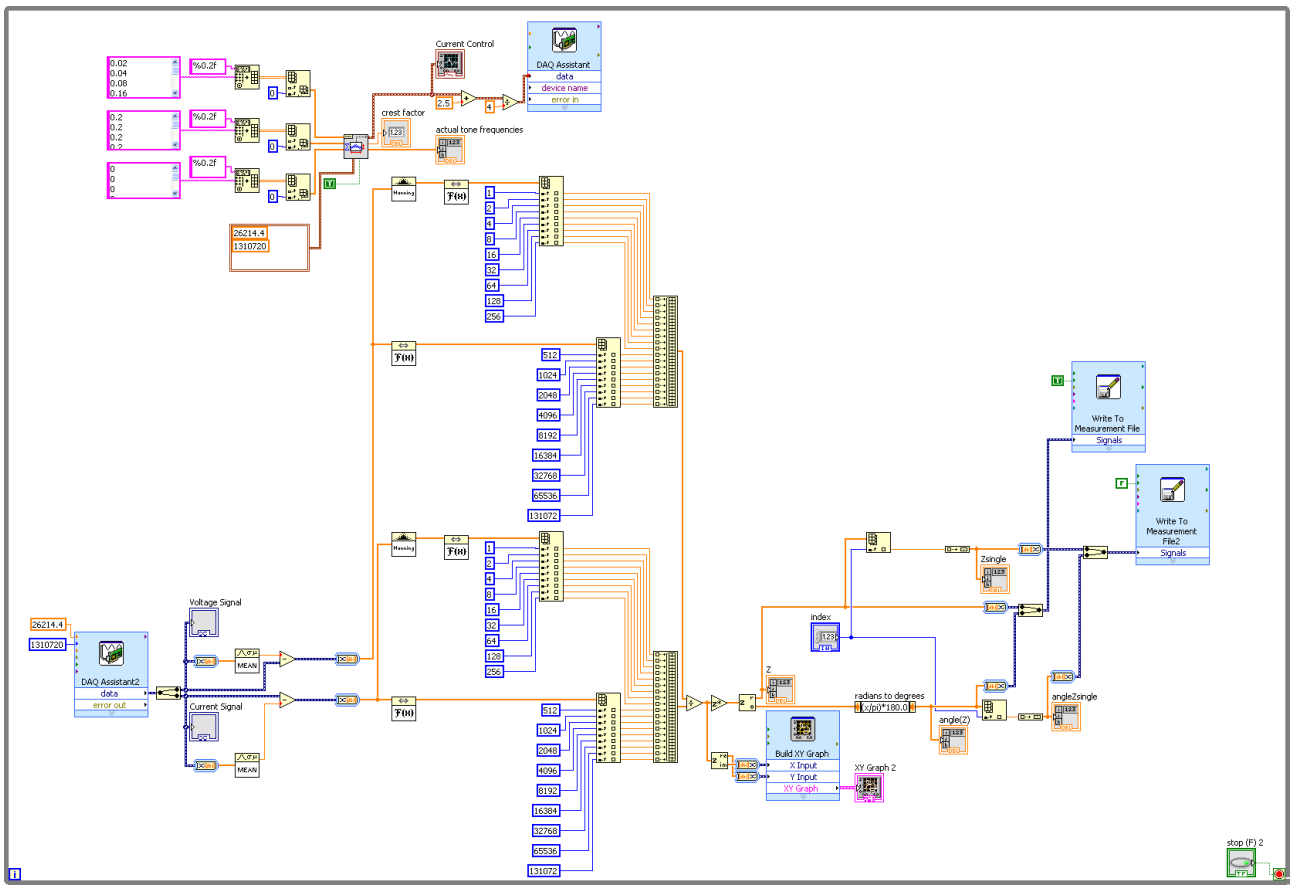

Figure 9-3: Block Diagram for EIS as well as BIS measurements from LabVIEW

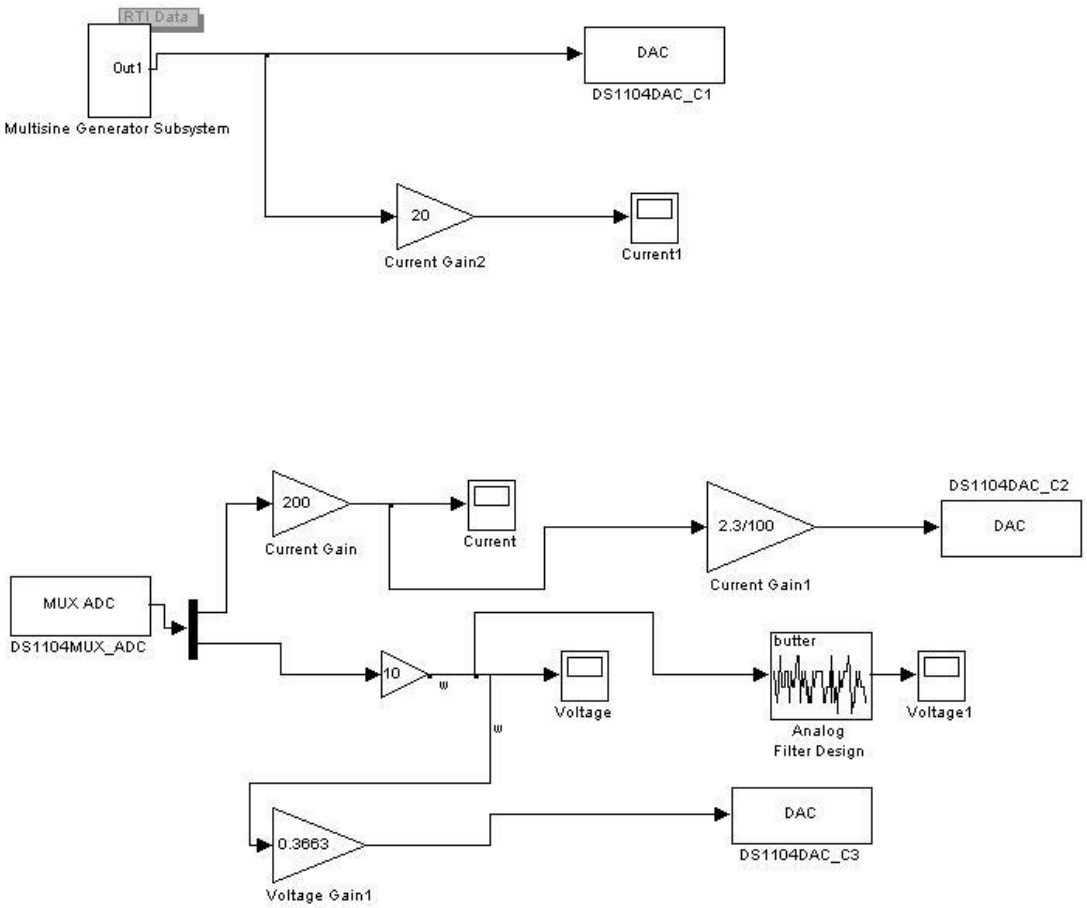

Figure 9-4: Multisine generator Simulink block diagram

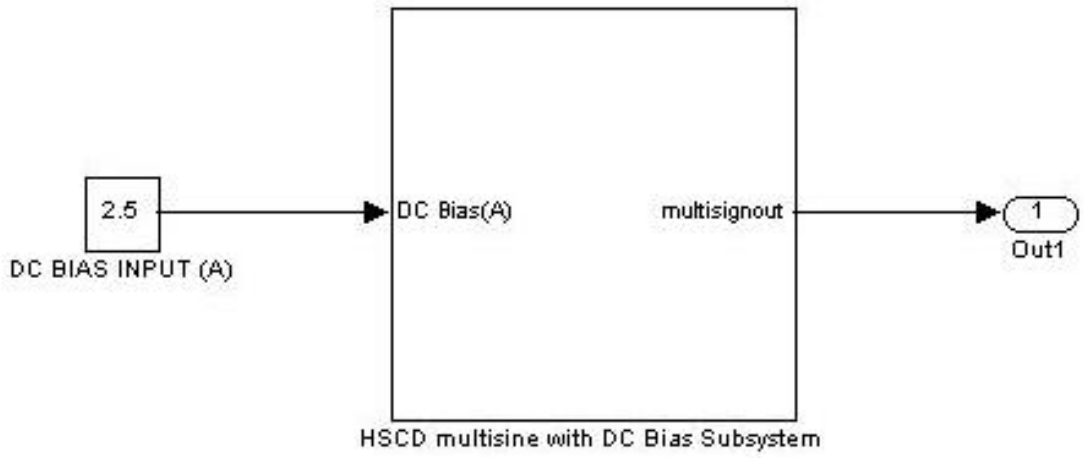

Figure 9-5: Subsystem 1-Multisine generation and DC Bias addition

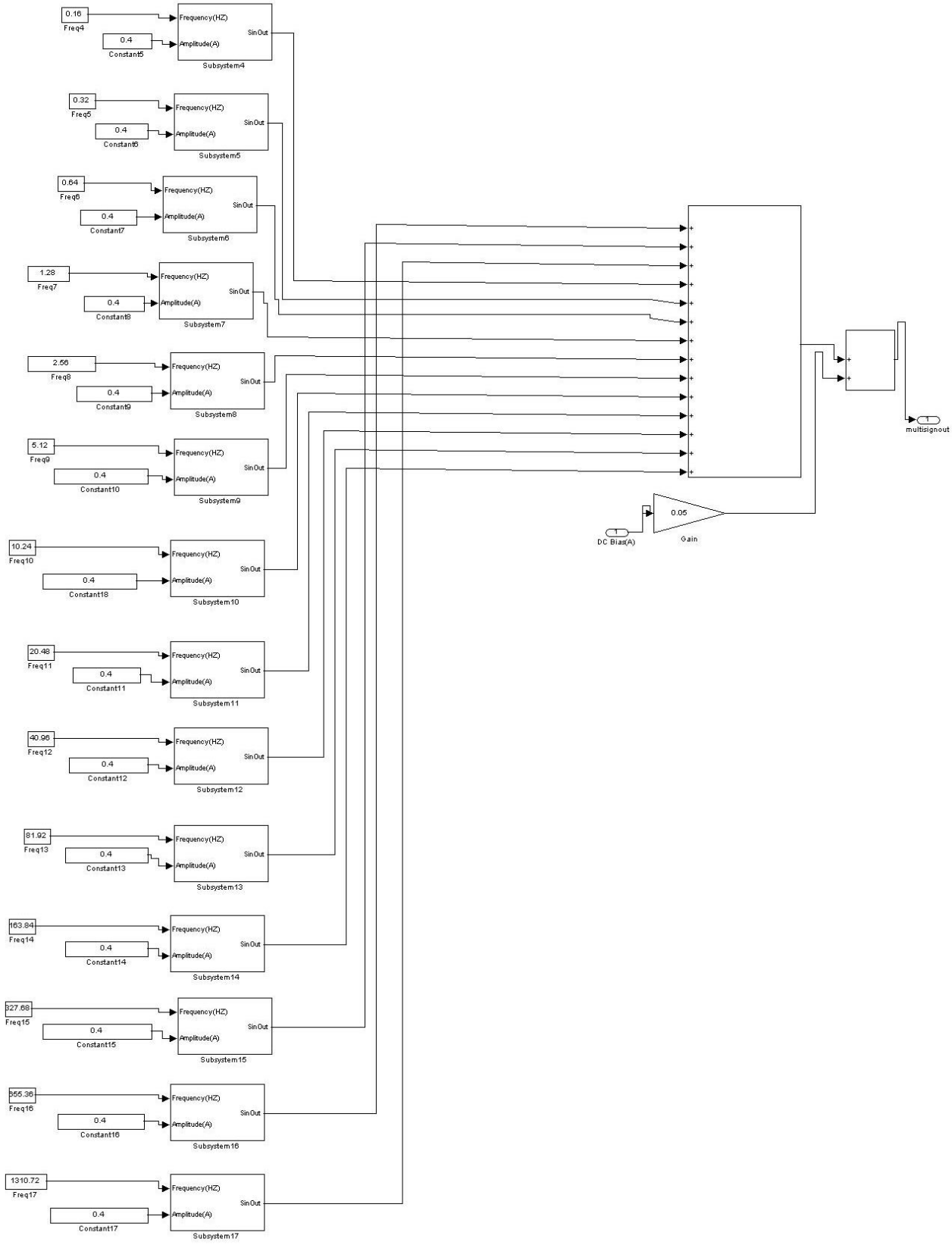

Figure 9-6: Subsystem 2

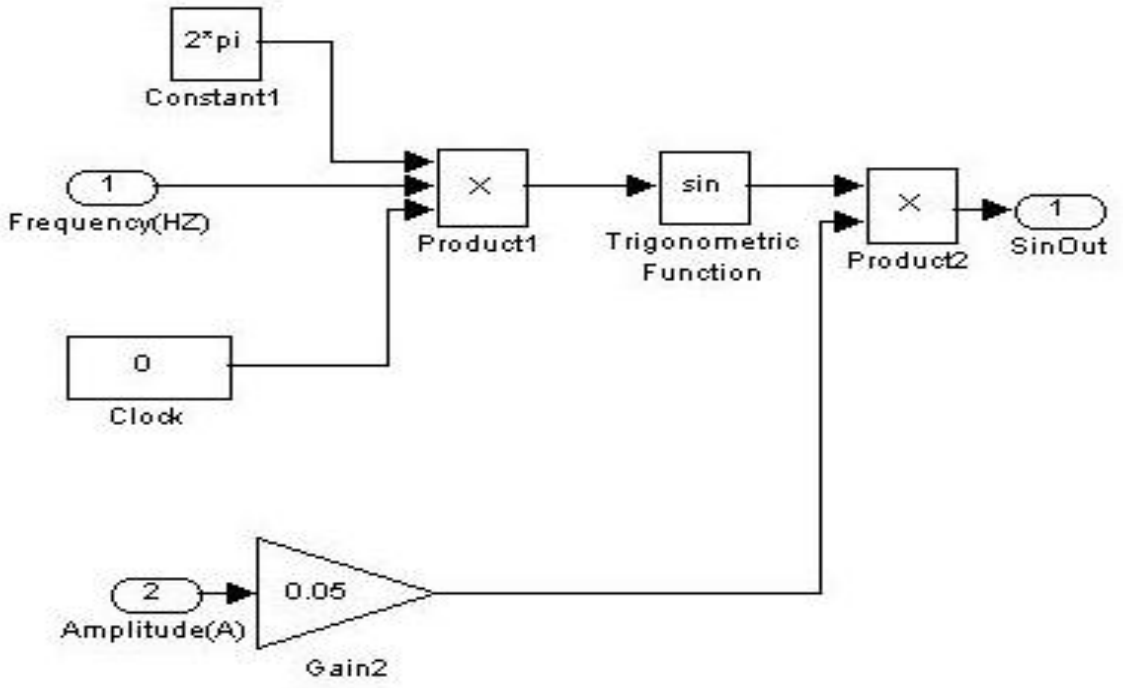

Figure 9-7: Subsystem 3

```
% This code implements a complex nonlinear least square fitting algorithm
% that extracts the Rs, R1, R2, CPE1, CPE2 values from the double
% R/Constant phase element circuit that models the CO20 Lithium-ion cells
%written and compiled by ALFRED WALIGO
clc
clear
%Model Fitting equations.
%Z = 1j*w*L + R_s + 1./(1./R_1 + (1j*w*CPE1).^PSI1) + 1./(1./R_2 + (1j*w*CPE2).^PSI2) ;
%This equation represents the impedance of the cell after taking into
%consideration the RC sections

%experimental data inserted here
ZData25412BIS = [0.00260099923994224 + 0.00020838282816624405i;0.00255026805921872 +
0.00016602691721501 1i;0.00249035346214626 + 0.00014663359558413 9i;0.00243325826377292 +
0.00014088292855612 7i;0.00238054078365489 + 0.00014021657700450 8i;0.00232404308144893 +
0.00015187085161196 2i;0.00226584907871484 + 0.00017154221132102 0i;0.00218358595555900 +
0.00021691277616422 9i;0.00206260480532903 + 0.00028596071084101 6i;0.00191509738022532 +
0.00032212734167424 2i;0.00174520637804405 + 0.00031832483100499 1i;0.00154565639201208 +
0.00022536707353163 3i;0.00137598143961521 + 0.00013580202113949 3i;0.00126360764900614 -
0.00018901804274799 3i];
ZData25412EIS = [0.00247678190784825 + 0.00018922838306020 3i;0.00249608719875277 +
0.00015668342676414 3i;0.00246178537821542 + 0.00014411367598106 4i;0.00241419680230987 +
0.00013556474363484 1i;0.00236693234663531 + 0.00013882458878557 9i;0.00230243455676885 +
0.00014506588777732 4i;0.00226653955030797 + 0.00017125264053363 5i;0.00217501258418184 +
0.00021889782696641 3i;0.00206656236268972 + 0.00026116853009937 3i;0.00191812464268894 +
0.00030358171076241 7i;0.00170177681851810 + 0.00029989941639557 5i;0.00153870535952837 +
0.00025687704560485 0i;0.00132724686586336 + 0.00011242667412978 4i;0.00115586906824799 -
0.00014557368260615 9i];
ZData25380EIS = [0.00270868650708506 + 0.00027883042577048 4i;0.00268978654940150 +
0.00019712259804191 1i;0.00264237467340862 + 0.00018723537413824 5i;0.00256354764667598 +
0.00016728557386110 4i;0.00249788669961053 + 0.00015990946159884 3i;0.00243784399625870 +
0.00017335700131641 1i;0.00237974582130838 + 0.00021007338233410 1i;0.00225584728455930 +
0.00025308699837497 7i;0.00212928766651217 + 0.00029771146842854 05i;0.00193855601776116 +
0.00033915271781599 7i;0.00173351809791673 + 0.00034235070351199 8i;0.00155876528954193 +
0.00026421917439744 9i;0.00143596054747584 + 9.34789072084517e-05i;0.00129142160070845 -
0.00020119455565108 5i];
ZData25380BIS = [0.00282052318627838 + 0.00020086745242535 8i;0.00274919995523593 +
0.00018867533995875 0i;0.00268727550452614 + 0.00017030602030332 4i;0.00262226744752020 +
0.00016307629539679 2i;0.00256072882385478 + 0.00016438944819942 3i;0.00249586607440116 +
```

```
0.0001797905719565741;0.00240701610984535 + 0.000208157264934316i;0.00233041162474655 +
0.0002551086768887801;0.00215697006056783 + 0.000340411910668696i;0.00202157018968237 +
0.0003540142360113331;0.00183191050809758 + 0.000346182997993046i;0.00160908701959572 +
0.0002861545173730391;0.00141563850791078 + 8.73902704228130e-05i;0.00131959488327931 -
0.0001764023482482571];
ZData25366EIS = [0.00359811338428842 + 0.00023836122546361 7i;0.00352004520017392 +
0.0002265540509460791;0.00341925127854104 + 0.0002249670706505021;0.00333899376321440 +
0.0002439133355116231;0.00323572161669375 + 0.0002787066746195431;0.00313687408355896 +
0.0003348138833680011;0.00298074766960645 + 0.0003972657107274741;0.00278685238397700 +
0.0004571444469002981;0.00254883397452137 + 0.0004956725070178601;0.00228712159084172 +
0.0004951654259731781;0.00201063773327990 + 0.0004228922019070231;0.00176692357478946 +
0.0002521218803432771;0.00155767994951240 - 7.68429438845537e-05i;0.00138321925521028 -
0.0005264071542214451];
ZData25366BIS = [0.00365830541137084 + 0.000237397382325146i;0.00357440966982988 +
0.0002171555024092801;0.00349330367979407 + 0.0002269284289116831;0.00340028016917620 +
0.0002482912581723941;0.00329533100936228 + 0.0002853985222687111;0.00316975055854178 +
0.0003437307682889901;0.00300170108491878 + 0.0004204183592535061;0.00279205663786452 +
0.0004818687671290341;0.00256081204814173 + 0.0005312345042790711;0.00227294522347772 +
0.0005419696690599441;0.00199727114076171 + 0.0004793996143932541;0.00174730831117215 +
0.0003549685418578821;0.00153514630249127 + 0.0001088431437775541;0.00139518609515305 -
0.0003120937962686361];
%data

%ZDATAB = [0.00347470566199850 + 0.000209240441778326i;0.00341762434317382 +
0.0002085101818377191;0.00335756473928212 + 0.0002175752624581501;0.00327064644837243 +
0.0002417083455725941;0.00315958112955909 + 0.0002733765366361981;0.00303233483057451 +
0.0003225882244244571;0.00288480702546588 + 0.0003790534702374491;0.00270217181123306 +
0.0004341062520279921;0.00248316315882277 + 0.0004719600731425551;0.00222688558333511 +
0.0004770846983824621;0.00198561192548418 + 0.0004236790580399781;0.00171129269173576 +
0.0002773176097004571;0.00151849334922170 - 4.10627011195643e-06i;0.00138181842163220 -
0.0003907350120451121];
ZDATAB = ZData25366BIS';
ZDATAB = conj(ZDATAB);
ZDATAB = fliplr(ZDATAB);
ZDATA = conj(ZDATAB);
ZDataB = [0.00138345013214100 + 0.000144729858282000i,0.00146545315954994 +
0.0002906596586475321,0.00163311448528264 + 0.0004229729045222881,0.00183358669934012 +
0.0005276588064298841,0.00211442866337513 + 0.0006254729630429021,0.00232865830416469 +
0.0006474870673958161,0.00267839540605509 + 0.0006744197867967571,0.00296056241032965 +
0.0006354952513930211,0.00322607074865160 + 0.0005280421618531061,0.00338318147874699 +
0.0004268291014718961,0.00350102789753206 + 0.0003551966507474711,0.00368508858002775 +
0.0002704573115097761,0.00377553024367196 + 0.0002530363197612731,0.00384772302396648 +
0.0002525144170890761,0.00400239040596750 + 0.0002916162516379041,0.00416738495548790 +
0.0004536150711485621];
ZData = conj(ZDataB);
wData = [2000,1108,614,340,189,104,57.89,32.07,17.77,9.85,5.46,1.68,0.514,0.158,0.93,0.048];
WDATA = [1310.72,655.36,327.68,163.84,81.92, 40.96, 20.48, 10.24, 5.12, 2.56, 1.28, 0.64, 0.32,
0.16];
L = 5*10^-7; n1 = 0.8 ;n2 = 0.6 ;
fun = @(param,WDATA)1j.*WDATA.*L + param(1) + 1./(1./param(2) + ((1j.*WDATA).^n1.*param(3))) +
1./(1/param(4)+((1j.*WDATA).^n2.*param(5)));
param0 = [0.0015, 0.0012, 0.1 0.1, 20]; %Initial values specification
w = log space(-1,3,500);
w1 = fliplr(w);
options = optimset('TolFun',1e-9, 'Display', 'iter', 'MaxFunEvals',10000, 'MaxIter', 1000); %non-
linear solver options
LB= [0,0,0,0,0]; %lower bounds of the result set
UB = param0;
paramT = lsqcurvefit(fun,param0,WDATA,ZDATA,LB,[],options);
Z = 1j.*w1.*L+ paramT(1) + 1./(1./paramT(2) + ((1j.*w1).^n1.*paramT(3))) +
1./(1/paramT(4)+(1j.*w1).^n2.*paramT(5));

%plot of simulated data
plot(conj(Z));
hold on

%plot of experimental data
plot(ZDATAB,'r');
```

9.2 Appendix B

ePLB C **High Energy Product**

+ Technology

Lithium Ion Polymer Battery
Li(NiCoMn)O_2-based Cathode
High Energy Density
Optimized for PHEV, EV

+ Product General Specification

Mechanical Characteristics

Model	C020
Length	217.0 ± 1 mm (excluding terminal)
Width	130 ± 1 mm
Thickness	7.1 ± 0.2mm
Weight	approx. 428 g

Electrical Characteristics

Nominal Voltage	3.65 V
Nominal Capacity	20 Ah
AC Impedance(1 KHz)	< 3mΩ
Specific Energy	174 Wh/Kg
Energy Density	370 Wh/L
Specific Power(DOD50%, 10sec)	2300 W/Kg
Power Density(DOD50%, 10sec)	4600 W/L

Operating Conditions

Charge Conditions

Recommended Charge Method	CC/CV
Maximum Charge Voltage	4.15 V
Recommended Charge Current	0.5 C Current

Discharge Conditions

Recommended Voltage Limit for Discharge	3.0 V
Lower Voltage Limit for Discharge	2.5 V
Maximum Discharge Current(Continuous)	up to 5 C Current
Maximum Discharge Current(Peak < 10sec)	10 C Current

Operating Temperature	-30℃ / + 55℃
Recommended Charge Temperature	0℃ / + 40℃
Storage Temperature	-30℃ / + 55℃

Cycle Life at 25℃ : (1 C Charge/ 1C Discharge, DOD 100%)
1000 Cycles to 80% Nominal Capacity

+ ePLB C020 Performance

Rate Capability

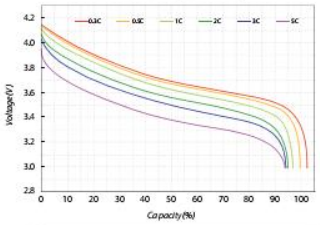

CHARGE : CC(0.5C)/CV(4.15V to 0.05C) at 25℃
DISCHARGE : CC to 3.0V at 25℃

Pulse Power Characteristics

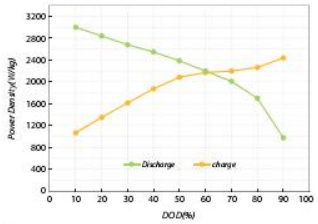

HPPC calculated from FreedomCAR Battery Test Manual

Cycle Life

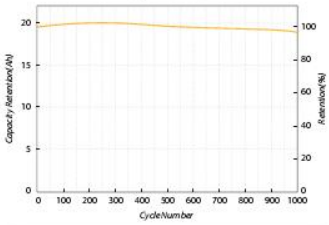

CHARGE : CC(1.0C)/CV(4.15V to 0.05C) at 25℃
DISCHARGE : CC(1.0C) to 3.0V at 25℃(DOD100%)

Figure 9-8: Datasheet for NCM C020 cells used for testing [53]

DEVICE SPECIFICATIONS

NI 6366

X Series Data Acquisition 2 MS/s/ch, 8 AI, 24 DIO, 2 AO

The following specifications are typical at 25 °C, unless otherwise noted. For more information about the NI 6366, refer to the *X Series User Manual* available from *ni.com/manuals*.

Analog Input

Number of channels	8 differential
ADC resolution	16 bits
DNL	No missing codes guaranteed
INL	Refer to the *AI Absolute Accuracy* section.
Sample rate	
Single channel maximum	2.00 MS/s
Minimum	No minimum
Timing resolution	10 ns
Timing accuracy	50 ppm of sample rate
Input coupling	DC
Input range	±1 V, ±2 V, ±5 V, ±10 V
Maximum working voltage for all analog inputs	
Positive input (AI+)	±11 V for all ranges, Measurement Category I
Negative input (AI-)	±11 V for all ranges, Measurement Category I

Caution Do not use for measurements within Categories II, III, and IV.

CMRR (at 60 Hz)	75 dB
Bandwidth	1 MHz
THD	-80 dBFS

Figure 9-9: NI 6366 device specifications [54]

Input impedance	
Device on	
AI+ to AI GND	>100 GΩ in parallel with 100 pF
AI- to AI GND	>100 GΩ in parallel with 100 pF
Device off	
AI+ to AI GND	2 kΩ
AI- to AI GND	2 kΩ
Input bias current	±10 pA
Crosstalk (at 100 kHz)	
Adjacent channels	-80 dB
Non-adjacent channels	-100 dB
Input FIFO size	
PXIe	8,182 samples shared among channels used
USB (32 MS)	32 MS shared among channels used
USB (64 MS)	64 MS shared among channels used
Data transfers	
PXIe	DMA (scatter-gather), programmed I/O
USB	USB Signal Stream, programmed I/O
Overvoltage protection for all analog input channels	
Device on	±36 V
Device off	±15 V
Input current during overvoltage conditions	±20 mA max/AI pin

Analog Triggers

Number of triggers	1
Source	AI <0..7>, APFI 0
Functions	Start Trigger, Reference Trigger, Pause Trigger, Sample Clock, Sample Clock Timebase
Source level	
AI <0..7>	±Full scale
APFI 0	±10 V
Resolution	16 bits

Figure 9-10: NI 6366 Analog Input specifications [54]

Modes	Analog edge triggering, analog edge triggering with hysteresis, and analog window triggering
Bandwidth (-3 dB)	
AI <0..7>	3.4 MHz
APFI 0	3.9 MHz
Accuracy	±1% of range
APFI 0 characteristics	
Input impedance	10 kΩ
Coupling	DC
Protection, power on	±30 V
Protection, power off	±15 V

AI Absolute Accuracy

Table 1. AI Absolute Accuracy

Nominal Range Positive Full Scale	Nominal Range Negative Full Scale	Residual Gain Error (ppm of Reading)	Offset Tempco (ppm of Range/°C)	Random Noise, σ (μVrms)	Absolute Accuracy at Full Scale (μV)
10	-10	114	35	252	2,688
5	-5	120	36	134	1,379
2	-2	120	42	71	564
1	-1	138	50	61	313

Note For more information about absolute accuracy at full scale, refer to the *AI Absolute Accuracy Example* section.

Gain tempco	8 ppm/°C
Reference tempco	5 ppm/°C
Residual offset error	15 ppm of range
INL error	46 ppm of range

Note Accuracies listed are valid for up to two years from the device external calibration.

Figure 9-11: NI 6366 Analog input absolute accuracy [54]

THURLBY THANDAR INSTRUMENTS

QPX1200L

1200 watt *PowerFlex* dc power supply - 60V, 50A max.

- *PowerFlex design gives variable voltage/current combinations*
- *Up to 60 volts and up to 50 amps within a power envelope*
- *Linear final regulation provides very low output noise*
- *Setting by direct numeric entry or by spin wheel*
- *High setting resolution of 1mV in up to 60 volts*
- *Multiple non-volatile setting memories*
- *Bench or rack mounting with front and rear terminals*
- *Analog, RS232, USB & LAN (LXI) interfaces standard, GPIB optional*

Figure 9-12: QPX 1200L power supply specifications [52]

QPX1200L 1.2kW PowerFlex dc power supply - 60V, 50A max.

Unrivalled Flexibility

The QPX1200L offers users a level of flexibility that can not be achieved with conventional laboratory power supplies.

With a current capability of 20 amps at the maximum output of 60 volts, its PowerFlex design offers increasing output current with reducing output voltage. The QPX1200L can therefore perform the task of many different power supplies.

Example voltage/current combinations include 60V/20A, 48V/25A, 37.5V/30A, 26V/40A, and 20V/50A.

High precision

With setting controlled by an instrumentation quality 16 bit DAC, the QPX1200L offers high accuracy and stability.

Low noise

Mixed mode regulation with a linear output stage gives the QPX1200L exceptionally low output noise for a unit of this power, and ensures good transient response.

Bench or rack mounting

Unlike most higher power laboratory PSUs, the QPX1200L is equally suited to bench or rack-mount applications.

Output and sense terminals are provided on both the front and rear panels. The case has integral tilt feet, and a 3U rack mount is available as an option.

A wide range of interfaces

The QPX1200 has analog, RS-232, USB and LAN interfaces as standard, the latter conforming with the LXI standard.
An optional GPIB interface can be specified at time of order.

OUTPUT SPECIFICATIONS

Voltage Range:	0V to 60V.
Current Range:	0A to 50A.
Power Range:	Up to 1200W - see PowerFlex power envelope graph.
Operating Mode:	Constant voltage or constant current with automatic cross-over and mode indication.
Voltage Setting:	By floating point numeric entry or rotary jog wheel; resolution 1mV.
Current Setting:	By floating point numeric entry or rotary jog wheel; resolution 10mA.
Setting Accuracy:	Voltage - 0.1% ± 2mV. Current 0.3% ± 20mA
Setting Stores:	Up to 10 set-ups can be saved and recalled via the keyboard or remote interfaces.
Load regulation:	<0.01% +5mV for a 90% load change.
Line regulation:	<0.01% +5mV for a 10% line voltage change.
Ripple & Noise:	Typically <3mV rms, <20mV pk-pk, (20MHz bandwidth).
Transient Response:	<250µs to within 50mV of set level for 90% load change.
Temp. Coefficient:	Typically <100ppm/°C.
Output Protection:	Forward protection by OVP trip; maximum voltage that should be applied to the terminals is 70V. Reverse protection by diode clamp.
Protection Functions:	Power Limiter, over-voltage, over-current and temperature trips.
Status Indication:	Display indication of Output On, CV, CI and Power Limit. Message on display for over-voltage trip.
Output Switch:	Push switch operating electronic power control. LED indication of On state
Output Terminals:	Front and rear output and sense terminals. Safety terminals accepting 6mm wire diameter, 6mm plugs or 8mm spades at 50 Amps max, or 4mm plugs at 30 Amps max.
Sensing:	Selectable local or remote sensing.

Designed and manufactured in Europe by:

Thurlby Thandar Instruments Ltd.
Glebe Road, Huntingdon. Cambs. PE29 7DR U.K.
Tel: +44 (0)1480 412451 Fax: +44 (0)1480 450409
Email: sales@tti-test.com **Web: www.tti-test.com**

POWER ENVELOPE

The maximum current at any voltage settings is limited by the power envelope which is set to give 20A at 60V rising to 50A at 20V under all ac supply conditions.
At lower output voltages the power is restricted by the 50 amps current maximum.

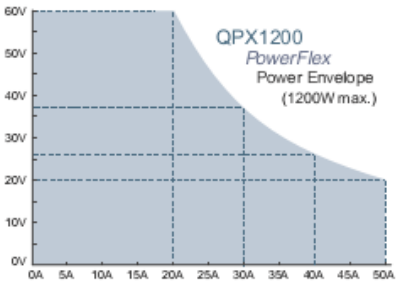

OUTPUT PROTECTION

Output Protection:	Output will withstand forward voltages of up to 70V a. Reverse protection by diode clamp.
Fault Condition Trip:	The output will be shut down if any of the four trip conditions listed below occur
Over Voltage (OVP):	Settable 2V to 65V in 0.1V steps
Over Current (OCP):	Settable 2A to 55A in 0.1A steps
Over Temperature:	Monitors internal temperature rise to protect against excess ambient temperature or blocked ventilation slots.
Sense Error:	Monitors the voltage between the remote sense terminals and output terminals to protect against mis-wiring.

METERING

Display Type:	Large dot-matrix black-on-white backlit LCD.
Meter Function:	5 digit voltage meter and 4 digit current meter. Display of limits values, memory contents etc. Wide range of alpha-numeric messages.
Limits Display:	Limits settings can be displayed simultaneously with measurements.
Meter Resolution:	Voltage: 1mV. Current: 10mA
Meter Accuracy:	Voltage: 0.1% of reading ± 2 digits Current: 0.3% of reading ± 2 digits

BUS INTERFACES

Quasi-Analog:	Voltage or current, 0 - 5V or 0 - 10V. (Digitised)
USB:	Standard USB harware connection.
RS-232:	Variable baud rate 19,200 max.
LAN:	Conforming to Ethernet standard and LXI standard.
GPIB (Option G):	Conforming with IEEE-488.1 and IEEE-488.2.

N.B. All bus interfaces incorporate full control, readback and status reporting.

Bus Type Selection:	From front panel (RS232/USB/LAN/GPIB).
Address Selection:	From front panel (1 to 31).
Baud Selection:	RS-232 only. From front panel (600 to 19200 baud).
Setting Resolution:	Voltage - 1mV, Current 1mA.
Readback Resolution:	Voltage - 10mV, Current 10mA.
Accuracy:	See specifications under Outputs and Metering.

GENERAL

AC Input:	110V to 240V AC ±10%, 50/60Hz. Installation Category II.
Power Consumption:	1600VA max.
Operating Range:	+5°C to +40°C, 20% to 80% RH.
Storage Range:	-40°C to + 70°C.
Environmental:	Indoor use at altitudes to 2000m, Pollution Degree 2.
Safety:	Complies with EN61010-1.
EMC:	Complies with EN61326.
Size:	350 x 130 x 413mm (WxHxD) (3U height) .
Weight:	9.2kg (20lb).
Benchtop Operation:	Folding legs are incorporated that can be used to angle the front panel upwards when required.
Rack Mount Option:	19 inch 3U rack mount.

82100-1320 Iss. 2

Figure 9-13: QPX 1200L power supply electrical characteristics [52]

THURLBY THANDAR INSTRUMENTS

LD300

DC Electronic Load, 80A, 80V, 300W

constant current, resistance, voltage and power

transient generator, variable slew rate, soft start

current monitor output, analogue remote control

Figure 9-14: LD300 DC electronic load [60]

CI, CR, CG, CV and CP modes

transient generator, variable slew rate

Multiple modes of operation

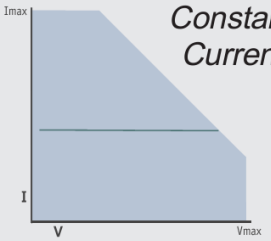

Constant current mode is used for load testing of normal voltage-source power supplies and for constant current discharge testing of batteries.

This mode provides rapid measurement of power source regulation (V/I characteristics).

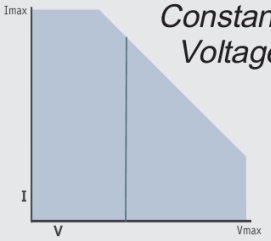

Constant voltage mode is used for load testing of constant current power supplies. The unit operates as a high power shunt regulator.

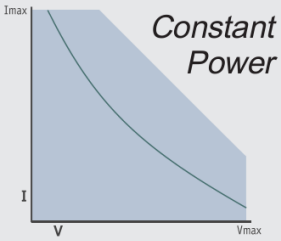

Constant power mode simulates a load whose power consumption is independant of the applied voltage. This is true of many types of equipment that incoporate switchmode regulators.

This mode may be particularly suitable for testing power sources of portable devices such as Lithium-ion batteries.

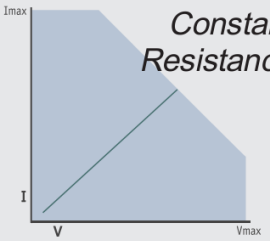

Constant resistance mode simulates a standard resistive load by providing a current drain proportional to voltage. Settings are displayed in Ohms or milli-Ohms.

Unlike fixed resistors or rheostats, the load provides a precisely controllable resistance with high power dissipation over a wide value range.

Constant Conductance

Constant conductance (CG) mode is also incorporated. As well as showing settings in amps per volt, this mode provides better resolution when setting very low equivalent resistance values.

Adjustable voltage drop-out

Some power sources, such as rechargeable batteries, can be damaged if their output voltage falls below a certain level.

The LD300 provides automatic protection by incoprorating fully variable voltage dropout (CI, CR, CG and CP modes).

Resistive discharge (conductance mode) with voltage dropout.

Note that in CR mode the load performs the equation I = (V -Vd)/R where Vd is the drop-out voltage.

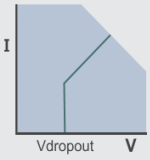

If the voltage applied to the load falls below a preset level, the load current is rapidly reduced to zero.

Transient generator and variable slew

The LD300 incorporates a full variable frequency, variable duty cycle transient generator.

Switching between the two preset levels can be done at any frequency between 0.1Hz and 10kHz.

The transient generator can be used in all operating modes.

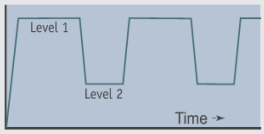

The rate of change between levels (slew rate) is controllable over a wide range.

Slew rate control applies to all changes of level including remote control and manual changes between level A and level B.

A slow-start function can be selected for situations where latching would otherwise occur at switch-on.

High resolution setting & measurement

The levels for each operating mode are set using high quality ten turn potentiometers for both level A and level B.

Levels are displayed using four digit meters which provide resolution down to 1mA, 1mV and 1mΩ.

Settings for slew rate, transient frequency, duty cycle and drop-out voltage can also be displayed.

In measurement mode the meters have an accuracy of 0.1% for voltage and 0.2% for current.

Remote control

The LD300 incorporates analogue remote control for all modes of operation. When "external voltage" is selected the level becomes linearly proportional to the voltage applied to the remote control inputs on the rear panel.

Any waveform can be used as the control voltage allowing complex load conditions to be simulated using, for example, an arbitrary waveform generator.

Alternatively, a logic signal can be used to switch between levels. When "external TTL" is selected, the level is switched between the two preset levels in response to an external logic signal.

The remote control inputs have a wide common mode range allowing the control voltage to be referenced independently of the load terminal voltages.

Current waveform monitor

It is often important to be able to observe the load current waveform on an oscilloscope. The LD300 provides a calibrated monitor output for this purpose as well as a sync output from the transient generator.

The monitor output has several volts of compliance with respect to the load input, thus allowing it to be connected to a grounded oscilloscope without current divertion.

Figure 9-15: LD300 DC electronic load features [60]

Technical Specifications

RATINGS

Voltage and Current:	80 volts maximum, 80 amps maximum.
Power Dissipation:	320 watts maximum continuous at 28°C. Derating to 300 watts continuous at 40°C.
Min. Operating Volts:	Increases with current, <0.5V at 10A, <1V at 40A, <2V at 80A.

OPERATING MODES

Constant Current Mode

Setting Range:	0 to 80A in 2 ranges, set by 10 turn control.
Meter Resolution:	1mA on 8A range, 10mA on 80A range.
Setting Accuracy:	± (0.2% + 20mA).
Regulation:	<30mA for a 20W to 280W power change.
Slew Rate Range:	<8mA/ms to >2500A/ms

Constant Resistance Mode

Setting Range:	0.04Ω to 100Ω in 2 ranges, set by 10 turn control.
Meter Resolution:	10mΩ on 10Ω range, 100mΩ on 400Ω range.
Setting Accuracy:	± (0.5% + 2 digits).
Regulation:	<2% for a 20W to 280W power change.
Slew Rate Range:	<3.3Ω/s to >4000Ω/ms

Constant Conductance Mode

Setting Range:	0.01A/V to 40A/V in 2 ranges, set by 10 turn control.
Meter Resolution:	0.001A/V or 0.01A/V depending on range.
Setting Accuracy:	± (0.5% + 2 digits).
Regulation:	<2% for a 20W to 280W power change.
Slew Rate Range:	<33mA/V/s to >400A/V/ms

Constant Voltage Mode

Setting Range:	Vmin to 80V in 2 ranges, set by 10 turn control. Vmin varies with current - see Ratings.
Meter Resolution:	1mV on 8V range, 10mV on 80V range.
Setting Accuracy:	± (0.2% + 2 digits).
Regulation:	<30mV for a 20W to 280W power change.
Slew Rate Range:	<2.5V/s to >800V/ms

Constant Power Mode

Setting Range:	0 to 320W, set by 10 turn control.
Meter Resolution:	1W.
Setting Accuracy:	± (0.5% + 2 W).
Regulation:	<2% for a 20W to 280W power change.
Slew Rate Range:	<0.1W/ms to >3,200W/ms

LEVEL CONTROL

Control Modes:
Level A, Level B, Transient Internal (switching between A and B using the built-in generator), Transient External (switching between A and B using an external switching signal), and Remote (level proportional to an external voltage).

Level A, Level B:
Each set by 10-turn potentiometer. Range, resolution and setting accuracy as shown above.

Slew Rate Control
All changes of level are subjected to slew rate control which is adjustable over a 30,000:1 range by a 3 position switch and vernier.

Input Enable
Latching switch which turns the load condition on.

Slow Start
Engages slew rate control to limit the speed of the ON transition when the input is enabled.

Dropout Voltage
Defines a minimum voltage below which the load current will reduce to zero (as may be required for testing batteries or power sources that can not be short circuited). Adjustable from 0V to 80V.

TRANSIENT GENERATOR

Pulse Repetition Rate:	0.1Hz to 10kHz in 3 overlapping ranges.
Setting Resolution:	0.1Hz, 1Hz, 10Hz depending on range.
Setting Accuracy:	± 2% of range.
Pulse Duty Cycle:	1% to 99% continuously variable.
Sync Output:	Pulse synchronous with transient level change.

DISPLAYS and METERING

Dual 4 digit LED displays showing a variety of settings or measurements as set by a five position switch.

Setting Displays:	Level A and Level B, Frequency and Duty Cycle, Slew Rate and Drop Out.
Measurements:	Amps and Volts, Watts and Ohms (calculated from V and I measurements).
Meter Accuracy:	Voltage ±(0.1% + 1 digit), Current ±(0.2% + 20mA).

REMOTE VOLTAGE SENSE

Remote or Local voltage sensing can be selected via a rear panel switch. Sense connections are on the rear panel terminal block.

Input Impedance:	680kΩ (each input) to load negative.
Max. Voltage Drop:	6 volts.

REMOTE CONTROL

Analogue - the level for any mode can be set by an external analogue voltage (4V full scale).

TTL - the change between the Level A and Level B settings for any mode can be done in response to an external logic signal.

The inputs for analogue or TTL have an impedance of 400kΩ to the power negative terminal and a common mode range of ±100V.

Remote Disable - when the front panel input enable switch is in the on position, this input can be used to turn the load on or off in response to an external logic signal. Fully opto isolated input.

CURRENT MONITOR

An analogue signal representing the current waveform is available for connection to an oscilloscope or external meter. Scaling is 50mV/Amp and compliance is ±3V with respect to the load negative terminal.

PROTECTION

The load incorporates both a power limiter circuit and a fault trip which responds to excess voltage, current, power or temperature. The trip puts the load into a high impedance state. Surge suppressors are incorporated to limit transient voltage spikes.

GENERAL

Rear Terminals:	Input via 6mm terminal/binding posts. Remote sense, current monitor, remote control via terminal block.
Front Terminals:	Input via 4mm terminal/binding posts (30A max.). Current monitor via 4mm sockets.
Power Requirement:	220V - 240V or 110V - 120V ±10%, 50/60Hz. Installation Category II. Consumption 30VA max.
Operating Range:	+5°C to +40°C, 20% to 80% RH.
Storage Range:	-40°C to +70°C.
Environmental:	Indoor use at altitudes up to 2000m. Pollution degree 2.
Safety and EMC:	Complies with EN61010-1 and EN61326.
Size:	130 x 212 x 435mm [HxWxD], (3U x half rack).
Weight:	6kg.
Option:	19-inch rack mount kit.

Accuracy specifications apply for 18°C to 28°C and 50W power.

Thurlby Thandar Instruments Ltd. operates a policy of continuous development and reserves the right to alter specifications without prior notice.

Designed and built in Europe by:

Thurlby Thandar Instruments Ltd.
Glebe Road, Huntingdon. Cambs. PE29 7DR United Kingdom (UK)
Tel: +44 (0)1480 412451 Fax: +44 (0)1480 450409
Email: sales@tti-test.com **Web: www.tti-test.com**

82100-0094

Figure 9-16: TTI DC electronic load technical specifications [60]